ERCOFTAC

Bulletin

December 2019

121

ERCOFTAC is a leading European association of research, education and industry groups in the technology of flow, turbulence and combustion. The main objectives of *ERCOFTAC* are: To promote joint efforts of European research institutes and industries with the aim of **exchanging technical and scientific information**; to promote **Pilot Centres** for collaboration, stimulation and application of research across Europe; to stimulate, through the creation of **Special Interest Groups**, wellcoordinated European-wide research efforts on specific topics; to stimulate the creation of advanced training activities; and to be influential on funding agencies, governments, the European Commission and the European Parliament.

www.ercoftac.org

Table Of Contents

Submissions

ERCOFTAC Bulletin
Institute of Thermal Machinery
Częstochowa University of Technology
Al. Armii Krajowej 21
42-201 Częstochowa
Poland
Tel: +48 343 250 507
Fax: +48 343 250 507
Email:ercoftac@imc.pcz.czest.pl

Hosted, Printed & Distributed By

Częstochowa University of Technology

ISSN: 2518-0991

Next *ERCOFTAC* Events

ERCOFTAC Spring Festival
16th of April, 2020
Cambridge, UK

ERCOFTAC Committee Meetings
17th of April, 2020
Cambridge, UK

The ERCOFTAC Best Practice Guidelines for Industrial Computational Fluid Dynamics

The Best Practice Guidelines (BPG) were commissioned by ERCOFTAC following an extensive consultation with European industry which revealed an urgent demand for such a document. The first edition was completed in January 2000 and constitutes generic advice on how to carry out quality CFD calculations. The BPG therefore address mesh design; construction of numerical boundary conditions where problem data is uncertain; mesh and model sensitivity checks; distinction between numerical and turbulence model inadequacy; preliminary information regarding the limitations of turbulence models etc. The aim is to encourage a common best practice by virtue of which separate analyses of the same problem, using the same model physics, should produce consistent results. Input and advice was sought from a wide cross-section of CFD specialists, eminent academics, end-users and, (particularly important) the leading commercial code vendors established in Europe. Thus, the final document can be considered to represent the consensus view of the European CFD community.

Inevitably, the Guidelines cannot cover every aspect of CFD in detail. They are intended to offer roughly those 20% of the most important general rules of advice that cover roughly 80% of the problems likely to be encountered. As such, they constitute essential information for the novice user and provide a basis for quality management and regulation of safety submissions which rely on CFD. Experience has also shown that they can often provide useful advice for the more experienced user. The technical content is limited to single-phase, compressible and incompressible, steady and unsteady, turbulent and laminar flow with and without heat transfer. Versions which are customised to other aspects of CFD (the remaining 20% of problems) are planned for the future.

The seven principle chapters of the document address numerical, convergence and round-off errors; turbulence modelling; application uncertainties; user errors; code errors; validation and sensitivity tests for CFD models and finally examples of the BPG applied in practice. In the first six of these, each of the different sources of error and uncertainty are examined and discussed, including references to important books, articles and reviews. Following the discussion sections, short simple bullet-point statements of advice are listed which provide clear guidance and are easily understandable without elaborate mathematics. As an illustrative example, an extract dealing with the use of turbulent wall functions is given below:

- Check that the correct form of the wall function is being used to take into account the wall roughness. An equivalent roughness height and a modified multiplier in the law of the wall must be used.
- Check the upper limit on $y+$. In the case of moderate Reynolds number, where the boundary layer only extends to $y+$ of 300 to 500, there is no chance of accurately resolving the boundary layer if the first integration point is placed at a location with the value of $y+$ of 100.
- Check the lower limit of $y+$. In the commonly used applications of wall functions, the meshing should be arranged so that the values of $y+$ at all the wall-adjacent integration points is only slightly above the recommended lower limit given by the code developers, typically between 20 and 30 (the form usually assumed for the wall functions is not valid much below these values). This procedure offers the best chances to resolve the turbulent portion of the boundary layer. It should be noted that this criterion is impossible to satisfy close to separation or reattachment zones unless $y+$ is based upon $y*$.
- Exercise care when calculating the flow using different schemes or different codes with wall functions on the same mesh. Cell centred schemes have their integration points at different locations in a mesh cell than cell vertex schemes. Thus the $y+$ value associated with a wall-adjacent cell differs according to which scheme is being used on the mesh.
- Check the resolution of the boundary layer. If boundary layer effects are important, it is recommended that the resolution of the boundary layer is checked after the computation. This can be achieved by a plot of the ratio between the turbulent to the molecular viscosity, which is high inside the boundary layer. Adequate boundary layer resolution requires at least 8-10 points in the layer.

All such statements of advice are gathered together at the end of the document to provide a 'Best Practice Checklist'. The examples chapter provides detailed expositions of eight test cases each one calculated by a code vendor (viz FLUENT, AEA Technology, Computational Dynamics, NUMECA) or code developer (viz Electricité de France, CEA, British Energy) and each of which highlights one or more specific points of advice arising in the BPG. These test cases range from natural convection in a cavity through to flow in a low speed centrifugal compressor and in an internal combustion engine valve.

Copies of the Best Practice Guidelines can be acquired from:

ERCOFTAC (CADO)
PO Box 1212
Bushey, WD23 9HT
United Kingdom
Tel: +44 208 117 6170
Email: admin@cado-ercoftac.org

The price per copy (not including postage) is:

ERCOFTAC members	
First copy	*Free*
Subsequent copies	75 Euros
Students	75 Euros
Non-ERCOFTAC academics	140 Euros
Non-ERCOFTAC industrial	230 Euros
EU/Non EU postage fee	10/17 Euros

BPG for CFD in Turbulent Combustion

ERCOFTAC
Best Practice Guidelines for CFD of Turbulent Combustion

Editors: Profs. Luc Vervisch, & Dirk Roekaerts
Foreword: Dr. Richard E. Seoud

The aim of this Best Practice Guide (BPG) is to provide guidelines to CFD users in a wide range of application areas where combustion is an essential process. Its overall structure is as follows:

Chapters 1-3 summarize the key issues in model formulation, Chapter 4 is addressing the validation of modeling using available experimental databases. Then, two application areas are elaborated in separate chapters: Chapter 5 on Internal Combustion Engines, and Chapter 6 on Gas Turbines. Best practice guidelines by the nature of technology development are always temporary. New insights and approaches will take over after some time. Therefore this BPG ends with a Chapter 7 on Emerging Methods, providing a preview of approaches so far only useful for simulating canonical configurations or requiring further developments.

A comprehensive CFD approach to turbulent combustion modeling relies on appropriate submodels for flow turbulence, chemistry and radiation, and their interactions. In the framework of this BPG, knowledge of turbulent flow modeling is a pre-requisite and only briefly explained. Instead the discussion on models is divided in three parts: turbulence-chemistry interaction (Chapter 1), chemistry (Chapter 2) and radiative heat transfer (Chapter 3). Many of the models introduced in the first three chapters will reappear in the discussion in Chapters 4 to 6 and comments on challenges, advantages and disadvantages are formulated in all chapters. Those looking for immediate advices to tackle a specific application may want to proceed immediately to the application chapters (IC engines in Chapter 5 and Gas Turbines in Chapter 6) and return to the basic chapters when necessary. But everyone not finding in these chapters an immediate answer to the basic question: What is the best model for my specific application? should certainly spend some time on Chapter 4, because it addresses the mandatory preliminary steps that have to be considered to validate a simulation involving any sort of turbulent flames.

We hope that many readers will find this BPG useful. Feedback on possible improvements is welcome. Instructions on how to provide such feedback is available on the ERCOFTAC webpages (www.ercoftac.org). When appropriate, the information received will be included in the courses promoting the use of this BPG and in future additions or updates.

Table of Content

To order please visit

`www.ercoftac.org/publications/ercoftac_best_practice_guidelines/`

Or from:
ERCOFTAC (CADO)
PO Box 1212
Bushey, WD23 9HT
United Kingdom
Tel: +44 208 117 6170

Email: `admin@cado-ercoftac.org`

The price per copy (not including postage) is:
ERCOFTAC members
First copy Free
Subsequent copies 75 Euros
Students 75 Euros
Non-ERCOFTAC academics, 140 Euros
Non-ERCOFTAC industrial, 230 Euros
EU / Non EU postage fee 10/ 17 Euros

Progress in RANS-based Scale-Resolving Flow Simulation Methods II

S. Jakirlić

Institute of Fluid Mechanics and Aerodynamics
Technische Universität Darmstadt, Alarich-Weiss-Straße. 10, 64287 Darmstadt, Germany

s.jakirlic@sla.tu-darmstadt.de

The procedure of hybridizing the RANS (Reynolds-Averaged Navier-Stokes) and LES (Large-Eddy Simulation) computational frameworks aimed at combining their advantages - with RANS exhibiting weaker sensitivity against grid non-uniformities being especially affordable in the attached near-wall regions and LES being capable of capturing the flows dominated by the organized large-scale coherent structures with a broader spectrum, as encountered for instance in the flows involving separation - has been experiencing intensified developments over the past two decades since the appearance of the DES (Detached-Eddy Simulation) methodology (Spalart et al., 1997, [1]) - finally numerous relevant sessions at major conferences, even the entire symposiums on Hybrid RANS-LES Methods (Hoarau et al., 2020, [2]) have been organized. Analogously to the role of the Smagorinsky-related subgrid-scale (SGS) models in LES, the dynamics of the residual turbulence in Hybrid LES/RANS computational schemes is described by an appropriately sensitized RANS-based model.

Contrary to the LES framework utilizing mostly the SGS models of the Smagorinsky type (0-equation models), where the grid spacing Δ represents the characteristic size of the largest unresolved scales (Sub-Grid-Scales), the representative length (and time) scales of the residual turbulence entering the relevant equations of motion in the hybrid LES/RANS methodologies are determined by solving respective equations describing the dynamics of corresponding turbulence quantities. In these introductory remarks just a few popular hybrid schemes will be briefly mentioned (the nominally grid-spacing-free SAS formulation, representing actually an eddy-resolving Unsteady RANS model, are purposefully introduced here within the same methodological concept): whereas the unresolved turbulence in the DES (Spalart et al., 1997, Spalart, 2009; Annu. Rev. Fluid Mech. 41: 181-202), PANS (Partially-Averaged Navier-Stokes; Girimaji, 2006; ASME J. Appl. Mech. 73: 413-421, Basara et al., 2011; AIAA J. 49(12): 2627-2636), PITM-$k-\epsilon$ (Partially Integrated Transport Model; Schiestel and Dejoan, 2005; Theoret. Comput. Fluid Dynamics 18: 443-468) and SAS-$k-\omega$ (Scale-Adaptive Simulations; Menter and Egorov, 2010; Flow Turbulence Combust. 85:113-138) methods is represented by an appropriately modelled turbulent viscosity, the PITM-$\overline{u_iu_j}-\epsilon$ (Chaouat and Schiestel, 2005; Phys. Fluids 17(065106): 1-19) and SAS-$\overline{u_iu_j}-\omega$ (Jakirlic and Maduta, 2015; Int. J. Heat Fluid Flow 51: 175-194) methods utilize the solutions of model equations governing the entire turbulent stress tensor. Accordingly, the RANS-based sub-scale models of different complexity have been employed. Correspondingly, the grid spacing incorporated into the hybrid LES/RANS models represents just one of several model parameters serving for the determination of the unresolved turbulent scales. The relevant model formulations point to complex relationships involving different turbulent quantities exhibiting high level of coherence. Consequently, unlike in the LES method, where the grid size Δ influences very directly the final outcome, the grid spacing Δ is a less influential factor in Hybrid LES/RANS models - such a model rationale has inherently much more physics, allowing the use of coarser spatial and temporal resolutions.

The present thematic issue of the ERCOFTAC Bulletin (with the first part published in the September 2019 Volume) attempts to give an overview of relevant activities in this very active field of research.

References

[1] Spalart, P.R., Jou, W.-H., Strelets, M., Allmaras, S. (1997): Comments on the feasibility of LES for wings and on a hybrid RANS/LES approach, 1st AFOSR Int. Conf. on DNS and LES. In: Liu, C., Liu, Z. (Eds.), Advances in DNS/LES. Columbus, OH, Greyden Press, pp. 137-147

[2] Hoarau, Y., Peng, S.-H., Schwamborn, D. and Revell, A. (Eds.) (2020): Progress in Hybrid RANS-LES Modelling 7. Notes on Numerical Fluid Mechanics and Multidisciplinary Design, Vol. 143, Springer Verlag (ISBN 978-3-030-27606-5), Contributions to the 7th Symposium on Hybrid RANS/LES Methods, Berlin, Germany, 2018; DOI: https://doi.org/10.1007/978-3-030-27607-2

RANS-based Sub-scale Modelling in Eddy-resolving Simulation Methods

S. Jakirlić, M. Bopp, C-Y. Chang, F. Köhler, B. Krumbein, L. Kutej, D. Kütemeier, I. Maden, R. Maduta, M. Ullrich, S. Wegt and C. Tropea

Institute of Fluid Mechanics and Aerodynamics, Technical University of Darmstadt
Alarich-Weiss-Straße 10, D-64287 Darmstadt, Germany

jakirlic@sla.tu-darmstadt.de

Abstract

The activities of the group for 'Modelling and Simulation of Turbulent Flows' at the Institute of Fluid Mechanics and Aerodynamics (Technical University of Darmstadt, Germany) in hybridizing the RANS (Reynolds-Averaged Navier-Stokes) and LES (Large-Eddy Simulation) computational methods for simulating complex turbulent flows are reviewed.

1 Introduction

All turbulent flows are inherently unsteady. Even if the mean flow can be regarded as steady (and e.g. two-dimensional) the turbulence is always unsteady (and three-dimensional). In some simple attached flows, the mean flow and corresponding turbulence structure can be correctly captured by using conventional models employed in (steady/unsteady) RANS (Reynolds-Averaged Navier Stokes) framework. However, in configurations featured e.g. by flow separated from curved continuous walls (characterized by intermittent separation region) the fluctuating turbulence associated with a highly unsteady separated shear layer has to be adequately (to an appropriate extent) resolved in order to capture even the mean flow properties correctly. Accordingly, the application of a suitable scale-resolving turbulence model is required. The flow complexity is especially enhanced when dealing with high Reynolds number flows. Extremely high demands on spatial and temporal resolutions prevent the application of highly feasible computational methods, such as Direct Numerical Simulation (DNS) and Large-Eddy Simulation (LES). Furthermore, a highly irregular anisotropic grid cells' arrangement, not only in the immediate wall vicinity, invalidates the Smagorinsky-related subgrid-scale models, keeping in mind an explicit dependence of the stresses residing in subgrid scales ($\tau_{ij} \propto \nu_{sgs} S_{ij}$) on the grid spacing, corresponding directly to the filter width. Especially suitable for handling such complex flows, also at higher Reynolds numbers, are the hybrid RANS/LES (Large-Eddy Simulation) methods. Their aim is to combine the advantages of both RANS and LES methods in order to provide a computational procedure that is capable to affordably capture the unsteadiness of the flow. Unlike in the LES framework utilizing mostly the SGS (SubGrid-Scale) models of the Smagorinsky type (0-equation models), where the grid spacing Δ represents the characteristic size of the largest unresolved scales (subgrid-scales), the representative length (and time) scales of the residual turbulence entering the relevant equations of motion in the hybrid LES/RANS methodologies are determined by solving respective equations describing the dynamics of corresponding turbulence quantities. Accordingly, the basic of any Hybrid RANS/LES method is a RANS-based model formulation describing the unresolved sub-scale fraction of turbulence. The RANS-based sub-scale models of different complexity are appropriately 'sensitized' to account for turbulence unsteadiness (fluctuating turbulence) by introducing either:

- a grid-spacing-dependent filter parameter: mostly in the length-scale determining equation - PANS (Partially-Averaged Navier-Stokes, proposed principally by Girimaji, 2006 and further developed by Basara et al., 2011, 2018) / PITM (Partially-Integrated Transport Model, developed principally by Chaouat and Schiestel, 2005) equation/expression - DES-related schemes (DES - Detached-Eddy Simulation, developed principally by Spalart et al., 1997; see also Spalart, 2009 for further upgrades) / VLES (Very LES; proposed principaly by Speziale, 1998;)
  or

- the von Karman length scale $L_{vK} = \kappa S/|\nabla^2 U|$ - nominally a grid-spacing-free model formulation; SAS - related models (Scale-Adaptive Simulation model developed principally by Menter and Egorov, 2010)

Accordingly, the model equations (formulated and validated within the Steady RANS framework, describing the fully-modeled turbulence) adapt automatically (by interplaying with the grid resolution) to the highly-unsteady (unresolved, residual) sub-scale turbulence. The grid spacing incorporated in the hybrid LES/RANS models, represents just one of several model parameters serving for the determination of the unresolved turbulent scales. The relevant model formulations point to complex relationships involving different turbulent quantities exhibiting high level of coherence. Consequently, unlike in the LES method, where the grid size Δ influences very directly the final outcome, the grid spacing Δ is obviously a less influential factor in Hybrid LES/RANS models - such a model rationale has inherently much more physics, allowing the use of coarser spatial and temporal resolutions.

2 Presently used eddy-resolving models

Following eddy-resolving computational models are presently in focus[1]:

- **VLES** (Very Large-Eddy Simulation) and **PANS** (Partially-Averaged Navier Stokes) - seamless, variable resolution hybrid LES/RANS models (Chang et al., 2014; Chang et al., 2015b; Jakirlic et al., 2014, 2016a, 2016b, 2017, 2018, Krumbein et al., 2017a, 2017b, 2018). In both methods a four-equation ERM-based model formulation (Elliptic-Relaxation Method), solving the equation describing the dynamics of the normal-to-wall turbulence intensity component in addition to equations governing the sub-scale kinetic energy of turbulence and its dissipation rate (Hanjalic et al., 2004), was employed to mimic the sub-scale model seamlessly in the entire flow domain. Whereas the destruction term in the equation governing the scale-supplying variable is appropriately modelled in the PANS framework, the VLES method is concerned with appropriate suppression of the turbulent viscosity in the equation of motion directly. Such actions cause turbulence level to be suppressed towards the 'subscale' ('sub-filter') level. Herewith, the development of the structural characteristics of the flow and associated turbulence is enabled.

- An **eddy-resolving Reynolds-stress model** (RSM) for unsteady flow computations: denoted as Instability-sensitive RSM - IS-RSM (Jakirlic and Maduta, 2015a, 2015b; Maden et al., 2015; Maduta et al., 2017; Kütemeier et al., 2019; Köhler et al., 2020; Bauer et al., 2020). The model scheme adopted, functioning as a 'sub-scale' model in the Unsteady RANS framework, represents a differential near-wall Reynolds stress model formulated in conjunction with the scale-supplying equation governing the homogeneous part of the inverse turbulent time scale. The model capability to account for the vortex length and time scales variability was enabled through a selective enhancement of the production of the dissipation rate in line with the SAS proposal (Menter and Egorov, 2010) pertinent particularly to the highly unsteady separated shear layer regions. Recently, the SAS-relevant methodological sensitivity towards adequate capturing of the turbulence instabilities is extended to an eddy-viscosity model Similar as in both PANS and VLES methods the Hanjalic et al. (2004) model formulation has been appropriately modified, Krumbein et al. (2020). The model proposed is denoted as **the eddy-resolving ERM-based eddy-viscosity model** (denoted by $ER-\zeta-f$). The initially proposed SAS-formulation involving the von Karman length scale ($L_{vK}=(\kappa S/|\nabla^2 U|)$), was reformulated here by expressing it as a function of the second derivative of the velocity field directly, as proposed originally by Rotta (1972). The latter modification, making the model even more sensitive against turbulence unsteadiness (a resolving mode can be enabled at even coarser grid resolutions), has been consequently used also in conjunction with the previously mentioned Reynolds-stress model, Kütemeier et al., 2019; Köhler et al., 2020; Bauer et al., 2020. Both URANS-based sub-scale model formulations are grid-spacing free unlike the majority of relevant hybrid RANS/LES models, representing certainly an advantage, especially if unstructured grids with arbitrary grid-cell topology are to be employed.

The predictive performances of the proposed models are intensively validated in numerous aerodynamic-type flows of different complexity featured by boundary layer separation, swirl and impinging, including also convective heat transfer cases. A selection of relevant results as well as the results obtained by the consequent models application to some configurations relevant to car aerodynamics and IC engines is illustrated in Section 3. All VLES and IS-RSM model equations are implemented into the OpenFOAM Code with which all respective computations have been performed, whereas the AVL-FIRE [1] code was applied for all PANS computations. In all cases second-order accurate spatial and temporal discretization schemes have been applied.

3 Computational illustrations

Selected results illustrating the predictive capabilities of the afore-introduced RANS-based eddy-resolving models are displayed in the following figures without going into specific details with respect to the flow configurations description, spatial (grid size and arrangement) and temporal resolutions, discretization methods, inflow and boundary conditions; for all these details interested readers are referred to respective publications.

3.1 PANS-related results

The predictive performance of the PANS methodology is preliminary investigated by computing a series of canonical, geometrically simpler configurations, but featured by complex flow straining and associated turbulent interactions including separation, swirling effects and mean compression in a square piston-duct assembly, Chang et al. (2015a, 2015b). The results shown presently are exclusively related to the external car aerodynamics (Jakirlic et al., 2016b, 2018). Figures 1-6 illustrate the feasibility of the PANS method in computing the flow past three 'DrivAer' car models (Heft et al., 2012; Heft 2014) characterized by differently designed rear end shapes: estate-back, fastback and notchback configurations. Fig. 1 depicts the vortex structure past the estate-back model visualized by using the Q-criterion.

The vortex structure refinement associated with an intensive unsteadiness in the wake behind the car can be observed. The near-wake region is populated with smaller vortices whereas the ligament-like vortices shedding from the car surface experience a certain disruption caused by a complex flow straining in the far wake region.

[1] A **zonal two-layer hybrid LES/RANS methodology** (it could also be considered as a **RANS-based wall-modelled LES**), with a differential near-wall eddy-viscosity model covering the wall layer and the conventional LES resolving the core flow, represents also a relevant research activity (Jakirlic et al., 2009, 2010 and 2011). Special attention was devoted to the coupling of both methods, the issue being closely connected to the treatment at the interface separating RANS and LES sub-regions. Hereby, great importance is attached to simplicity, efficiency and applicability to complex geometries. The exchange of the variables across the LES/RANS interface was adjusted by implicit imposition of the condition of equality of the modelled turbulent viscosities (by assuming the continuity of their resolved contributions across the interface), enabling a smooth transition from RANS layer to the LES sub-region. Next important issue is the utilization of a self-adjusting interface position in the course of the simulation. A control parameter representing the ratio of the modelled (SGS) to the total turbulent kinetic energy in the LES region, averaged over all grid cells at the interface on the LES side, is adopted in the present zonal modelling strategy.

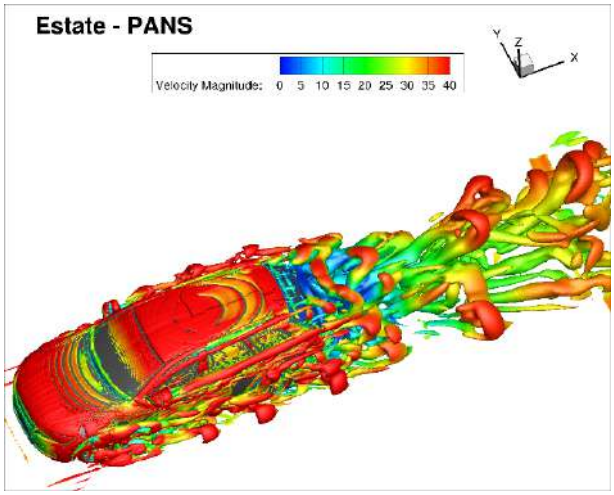

Figure 1: Q-criterion visualization of the vortex structure past the estate-back configuration predicted by PANS method ($Q = 6500s^{-2}$)

The appropriately high resolution of the structural characteristics of the wake region led to its intensive spreading pointing to an enhanced turbulence activity, complying with the PANS method's capability to capture fluctuating turbulence to a corresponding extent. Figures 2 show the PANS-related mean velocity field and associated streamlines illustrating the separation region behind the estate-back and fast back 'DrivAer' car models.

Whereas the fastback and notchback (not shown here) models are characterized by a very similar wake topology, the estate back configuration points to a much more complex vortex system. The correspondingly large flow reversal region occupying the entire box-type rear-end originates from the boundary layer separating in parallel (in the spatial sense) from the roof edge over its entire spanwise extent, sides and underbody. Accordingly, a complex vortical pattern is formed consisting of two pairs of counter-rotating vortices: the base vortices interacting with the ground (encountered also in both the notchback and fast-back configurations) and the so-called tip vortices. The surface pressure distribution (Fig. 3) at the car body is completely in accordance with the computed velocity field exhibiting total deceleration within the stagnation region occupying the front part (characterized by $Cp = 1$) followed by high acceleration at the strongly curved front car surface associated with a steep Cp decrease. After the pressure alternation from a characteristic rise at the engine cover surface and a further pressure drop reflecting the effects of the favourable pressure gradient due to a flow acceleration over the front window a certain plateau characterized by negative values pertinent to the roof surface is reached. Apart of the roof locality accommodating the wall-mounted sting (not accounted for in the computational study), the agreement with the experimental results is very good. The Cp-developments related to three investigated rear end designs start to differ from each other approximately at the middle of the roof. Whereas a negative pressure plateau characterizes the estate-back configuration preceding a sudden jump to an almost zero Cp-value related to a relatively steep transition from the roof to the rear-window, the pressure development at the notchback and fastback car models exhibits a much more complex trend. The relevant pressure progressions are qualitatively similar, but the distinct positive peak values are spatially

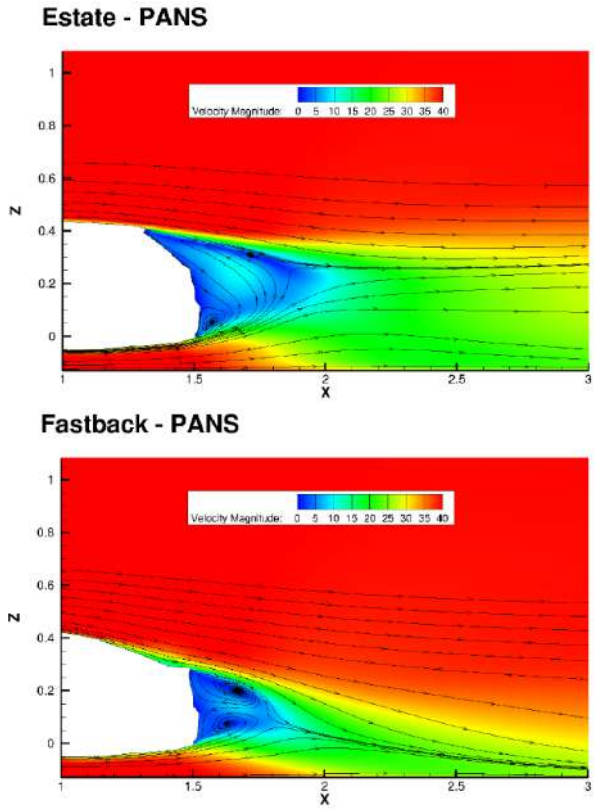

Figure 2: Estate-back and fastback 'DrivAer' car models: mean streamlines and iso-contours of the velocity field colored by its magnitude obtained by the PANS method

shifted, with that related to the fastback model occurring more downstream, following the turnover of the velocity field from accelerating to decelerating mode.

A qualitative impression about the flow past a BMW car model taking over a truck model is illustrated in Fig. 4. Both vehicles represent down-scaled (1:2.5), geometrically-similar models of realistic vehicle configurations for which on-road measurements have been performed by Schrefl (2008). Figures 5 display the Q-criterion visualization of the vortical flow structure corresponding to two car-truck relative positions $x/L = -0.80$ and $x/L = 0.39$, with the latter relating to the most critical car-truck constellation characterized by the largest drag coefficient. Between these positions a characteristic change of the drag coefficient from reduced to enlarged

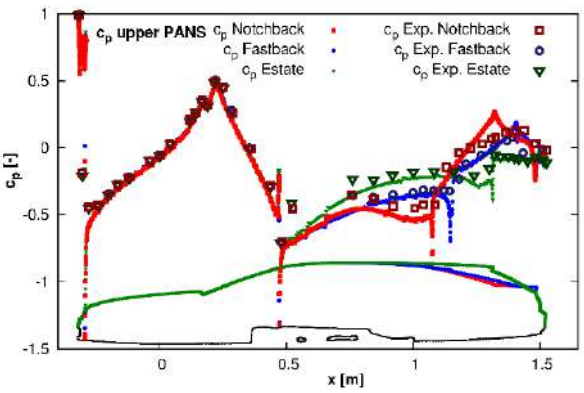

Figure 3: Development of the mean surface pressure coefficient over the upper surface of all three investigated configurations - notchback, fastback and estate-back

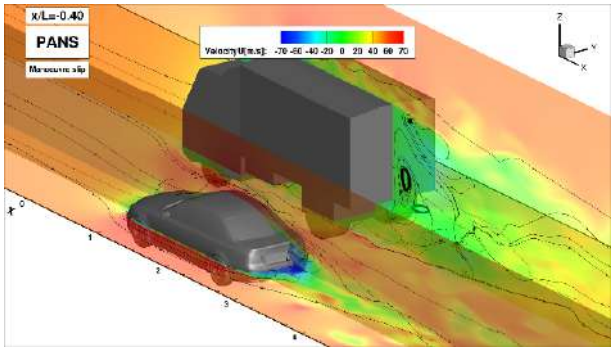

Figure 4: Computationally obtained instantaneous velocity field and corresponding streamlines related to the car-truck relative position $x/L = -0.40$

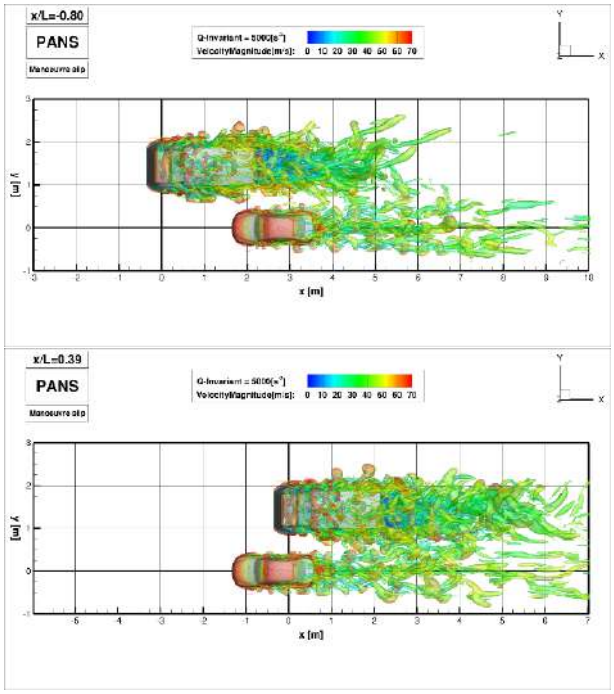

Figure 5: Computationally obtained vortex structures related to the car-truck relative positions $x/L = -0.80$ (upper) and 0.39 (lower) visualized by the Q-criterion

value relative to the isolated single car occurs (investigated by Jakirlic et al., 2014). The inherent flow unsteadiness originating from the multiple stagnation regions at the front end of both vehicles, front side of the wheels and mirrors remained preserved down to the far wake region. These pictures indicate also the spatial extent of the vortical structures in terms of their size and shape diversity, similar to those displayed in Fig. 1. The complex flow straining expressed through an intensified interaction between wall-bounded and subsequent multiple separated shear layers influences strongly the formation of the wake region. Similar as in the case of the 'DrivAer' model (Fig. 1) the adequate capturing of the intensified turbulence activity within the wake requires an appropriately high resolution of the related structural properties, representing the inherent feature of the PANS methodology. Figures 6 show the development of the aerodynamic coefficients associated with the side force (F_s), representing the spanwise (y) component of the force comprising contributions originating from both the pressure and friction forces, and the yawing moment (C_{Mz}). The PANS results are obtained

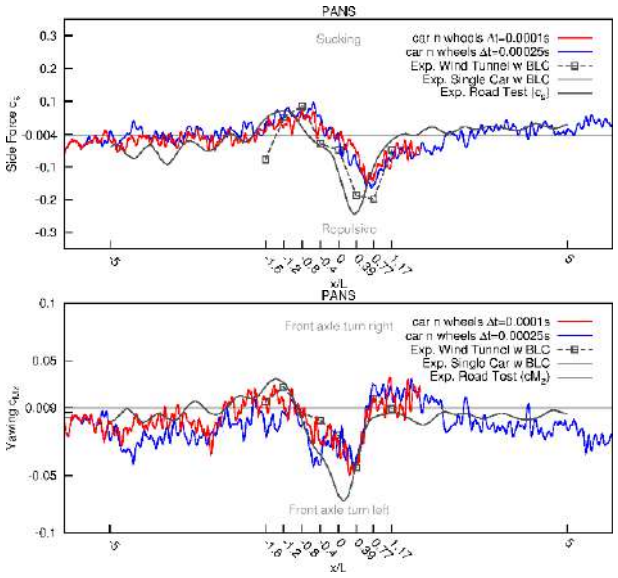

Figure 6: Variation of the car-related aerodynamic coefficients associated with the side force (C_s) and yawing moment (C_{Mz}) during the overtaking manoeuvre

by applying two temporal resolutions corresponding to time steps $\Delta t = 0.0001sec$ and $\Delta t = 0.00025sec$. The solid black lines displaying the development of both coefficients represent the experimental results determined during the 'on-road' overtaking process involving realistic vehicles. The prime focus of the experimental campaign was the investigation of the car stability during the 'on-road' overtaking manoeuvre, characterized by strong unsteadiness of the oncoming flow. Accordingly, only these two mostly relevant quantities have been measured. In addition, the quasi-steady wind-tunnel measurements, represented by the square symbols, are used here as a reference. Both coefficients follow closely the experimental reference. Outside of the 'overtaking region' (taking place between $x/L = -1.60$ and $x/L = 1.17$) both coefficients oscillate weakly about the value corresponding closely to that related to the isolated single car (marked by the horizontal line). The flow acceleration, and consequently the pressure reduction, within the gap between two vehicles is especially pronounced at the relative position $x/L = -0.80$ corresponding to the highest positive value of the side force directed towards the truck (Fig. 6-upper). This effect, representing an expected outcome complying with the car situated in the truck wake characterized by lower flow velocities, implies the truck exerting a suction effect on the car. Analysis of the yawing moment development (Fig. 6-lower), the maximum value of which is reached somewhat earlier compared to the side force, reveals a complementary reaction: the car's front axle is turned into right direction towards the truck. In the further course of the overtaking process a dramatic change of both coefficients, from positive to negative values, takes place. The side force coefficient experiences its lowest (negative) value at the relative position $x/L = 0.39$; the minimum negative value of the yawing moment is recorded earlier, at the position $x/L \approx 0.0$. The flow within the narrow gap is still accelerated, but there is a bow-wave effect originating from the truck acting repulsively on the car. This process is complemented by the front axle turning into left direction away from the truck, being in relation with the negative yawing moment.

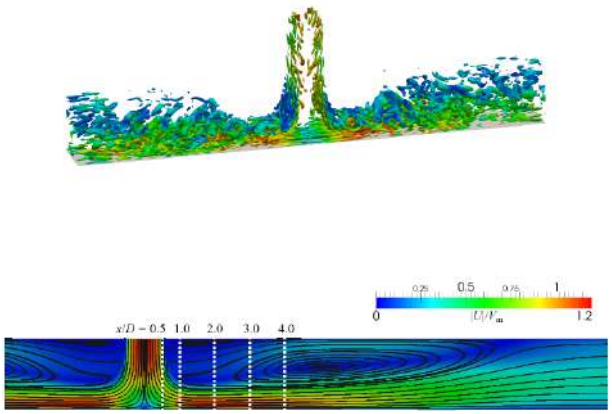

Figure 7: Q-criterion-visualization of the vortical structure in the impinging jet flow coloured by velocity magnitude (upper), mean velocity field and corresponding streamlines (lower)

3.2 VLES-related results

In the course of the VLES model development different canonical flows have been computed: natural decay of the homogenous isotropic turbulence, channel flow in a Reynolds number range (also over a rough surface, Krumbein et al., 2017a) and separated flow over a curved continuous surface, Chang et al. (2014). The method is consequently applied to a swirling flow in cooling hole of a turbine blade as well as to different vehicle aerodynamics cases, Jakirlic et al. (2016a, 2017). Here, some selected results related to a slot-jet impinging perpendicularly onto a heated wall and thermal mixing in a cross-stream type T-junction (Krumbein et al., 2017b, 2018) will be presented.

Fig. 7 shows the vortex structure of the plane jet at $Re_m = 9120$ impinging onto a heated wall visualized by Q-criterion and the resulting mean velocity field with corresponding streamlines. The strong deceleration of the jet by approaching the bottom plate related to the stagnation region and subsequent acceleration and wall-jet formation are clearly visible. A large recirculation zone with a very low back-flow intensity is created at the upper wall.

Figures 8 show the semi-log plots of the mean velocity and temperature profiles obtained by the VLES and RANS (employing the $\zeta - f$ model representing the RANS constituents of the VLES) methods along with the DNS results (Hattori and Nagano, 2004) at selected streamwise x/D-locations (marked by dashed lines in Fig. 7). Fig. 8-upper shows the velocity in the near-wall region normalized by the local wall friction velocity U_τ varying in streamwise direction. The displayed mean velocity profile development reveals very strong departure from the equilibrium conditions, underlying the logarithmic law. The high positive pressure gradient typical of the impingement region (streamwise position $X/D = 0.5$) causes large departure from the log-law in line with the strong jet deceleration when perpendicularly impinging the wall. The consequent flow relaxation in terms of the mean velocity intensification (flow acceleration) pertinent to the wall jet region is documented at the positions $x/D = 1 - 4$ in very good

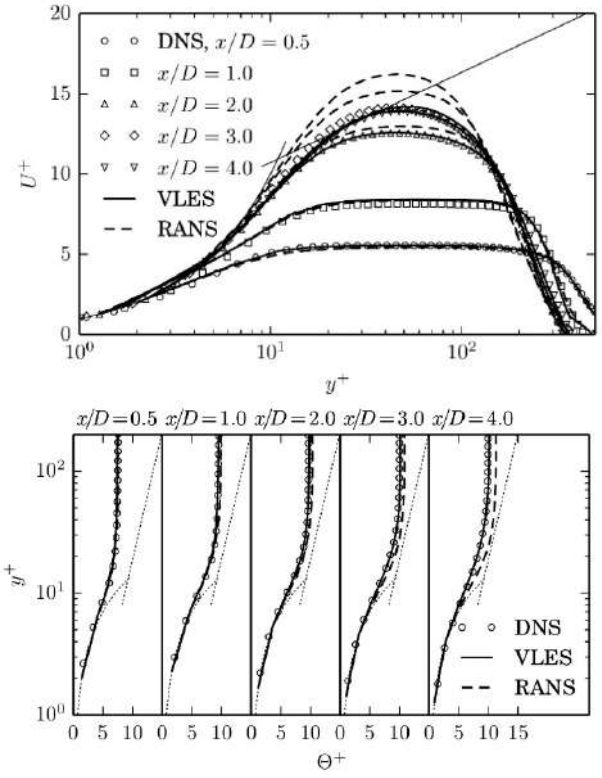

Figure 8: Velocity and temperature profiles in wall units at different locations x/D. For better visibility, only every third data point of the DNS data set is shown

agreement with the DNS database. With the RANS model a slight overprediction of the velocity at the more upstream positions is obtained. Regarding the thermal fields, mean temperature field is analysed. Fig. 8-lower shows temperature profiles in wall units at different positions along the impingement plate. The temperature is non-dimensionalized by normalizing the difference of the temperature and the local wall temperature $(T - T_w)$ with the friction temperature $\theta_\tau = q_w/(\rho C_p U_\tau)$. Again a highly non-equilibrium nature of the thermal field considered is clearly illustrated by a corresponding departure from the conditions associated with the logarithmic law. Very good agreement is obtained with the VLES model, while the RANS model overpredicts slightly the temperature away from the wall at further downstream positions.

Thermal mixing in two cross-stream T-junction configurations occurring under constant (DNS reference by Hattori et al., 2014) and variable (experimental reference by Hirota et al., 2010) fluid properties is presently considered. Here, as an illustration, only the results related to the former configuration will be shown, Figure 9-11 (for more details Krumbein et al. 2018 should be consulted). The flow field arising from the impingement of the two crossing streams is displayed in Fig. 9. The flow issuing from the vertical branch-channel detaches at its right upper edge denoted by position $x/H = 0.0$; subsequently, a flow reversal zone is developed at the lower main-channel-wall with associated flow acceleration in the upper part of the channel complying with the continuity condition. The separated shear layer aligned with the mean dividing streamline is primarily responsible for a strong turbulence production - the most intensive turbulence activity originates from the separation process (see Fig. 10). Further downstream at $x/H = 2$, the flow reattaches. The Q-criterion image ($Q = 10s^{-2}$) enables

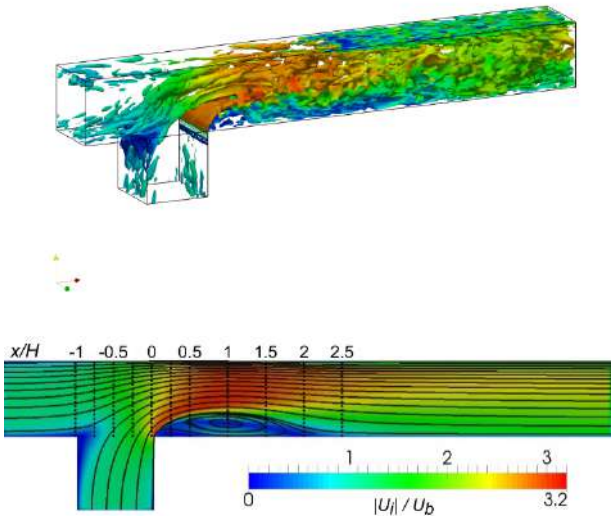

Figure 9: Q-criterion-visualization of the vortical structure in the T-junction configuration coloured by velocity magnitude (upper), mean velocity field and corresponding streamlines (lower)

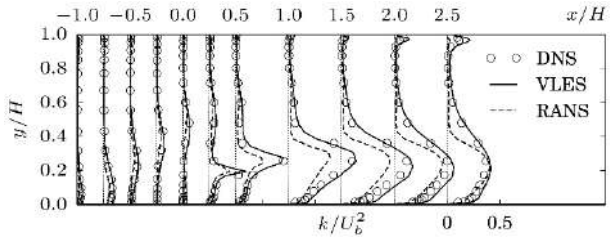

Figure 10: Turbulence kinetic energy profiles normalized by the bulk velocity at different streamwise positions

visualization of the mechanisms of the separated shear layer generation at the right edge of the vertical branch channel dominated by the spanwise vorticity, its rolling up and finally its shedding and disruption by a correspondingly complex straining within the main horizontal channel. The profiles of the kinetic energy of turbulence (Fig. 10) and appropriately normalized mean temperatures (Fig. 11) are evaluated at different streamwise positions x/H marked by the dotted lines in Fig. 9. The results interpretation covers all characteristic flow localities: crossing/merging zone of main and branch streams, recirculation zone including separation and reattachment points, as well as the post-reattachment region. Typical turbulent intensity field is obtained revealing the strong profiles' asymmetry with characteristic near-wall

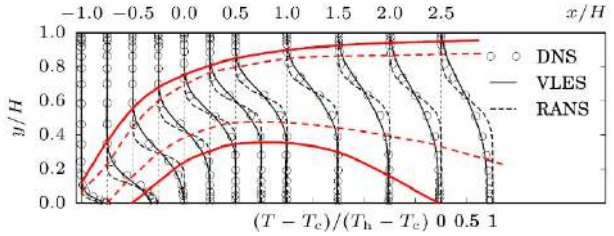

Figure 11: Temperature profiles normalized with hot and cold stream temperatures at different streamwise positions (red lines denote the thermal layer spreading)

peaks representing the consequence of enhanced turbulence production due to the strong velocity gradients at both bottom and upper walls, and the intensified turbulence activity at the wall distances coinciding with the separated shear layer region. Overall good agreement between the VLES and DNS data can be observed. The $\zeta - f$-RANS model underpredicts the turbulence level, especially in the separated shear layer region and the recirculation bubble. The underestimation of the turbulence kinetic energy in the separated shear layer is, as it is well-known, associated with a weaker momentum transfer into the recirculation zone representing the prime reason for the overestimation of the length of the recirculation bubble. The thermal layer area characterized by large temperature gradients (Fig. 11) progresses above the separated shear layer representing the region where the thermal streams originating from both inflow channels merge. Thermal mixing is captured accurately within the VLES framework. In the RANS simulation however, thermal mixing intensity is severely underpredicted resulting in a too narrow thermal mixing layer, characterized by a too steep temperature gradient with corresponding underestimation of temperature level in the upper and overestimation in the lower part of the main channel. This points to a weaker momentum exchange and consequently a lower spreading rate of the separated shear layer; the latter outcome is, as discussed earlier, directly correlated with the lower turbulence activity in this region.

3.3 IS-RSM-related results

Numerous canonical attached flows and flows separated from sharp-edged and curved walls have been computed in the course of interactive model development and validation, Jakirlic and Maduta (2015a, 2015b). Figures 12-23 offer a relevant overview illustrating the feasibility of the model in simulating flows of enhanced complexity subjected to different extra strain rates relevant e.g. to plasma-actuated flow control towards the pressure recovery enhancement in a 3D diffuser (Maden et al., 2015), flow and aeroacoustics past a tandem cylinder (Maduta et al., 2017; Köhler et al, 2020), dynamic stall effects at a plunging airfoil (Kütermeier et al., 2019) and pulsating flow in an aortic aneurysm (Bauer et al., 2020).

Flow in the 3D diffuser is extremely complex, Fig. 12. It is characterized by a 3D separation bubble starting in the corner built by two expanding walls (blue area). Initial growth of this corner bubble reveals its spreading rate along two sloped walls being approximately of the same intensity. As the adverse pressure gradient along the upper wall significantly outweighs the one along the side wall due to a substantially higher angle of expansion, 11.3° vs 2.56°, the separation zone spreads gradually over the entire top wall surface. The strong three-dimensional nature of the separation pattern is obvious.

The pulsed forcing imparted by the plasma actuator (PA; mounted on the upper wall of the inflow duct) to the fluid flow in the spanwise direction, generating a pair of the streamwise vortices, changes completely the natural sense of the rotational pattern of the secondary motion in inflow duct as well as its intensity, Fig. 13. The orientation of the PA-generated vortex in the upper duct corner opposes a fairly weak vortex in the lower duct corner, with the latter still resembling the orientation of the baseline secondary motion. The relevant peak transverse velocity magnitude is about ten times higher compared to the baseline configuration and about twenty times higher in the case of continuous ac-

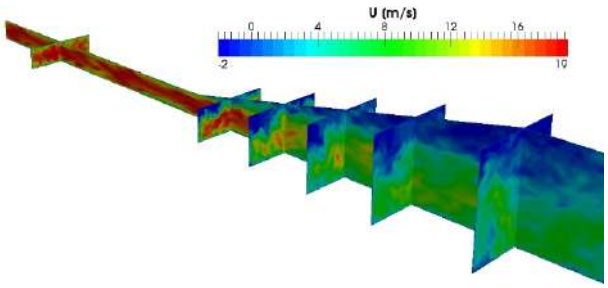

Figure 12: Flow in a 3D diffuser, baseline configuration - instantaneous velocity field

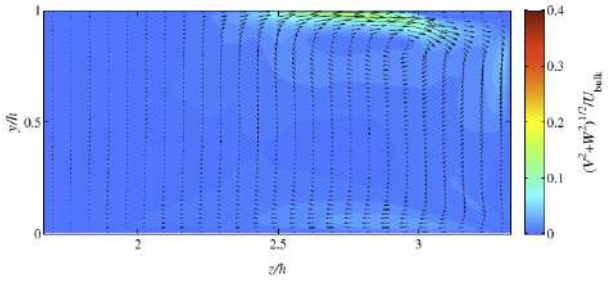

Figure 13: Flow in a 3D diffuser, plasma-actuated configuration (pulsed mode with 40% duty cycle) - time-averaged velocity field coloured by velocity magnitude and corresponding velocity vectors in the cross-section of the inflow duct (only one half is shown)

tuation (not shown here). Depending on the operating mode, the plasma-actuated manipulation of the inflow conditions modifies secondary flow structure selectively, either towards an increase of the turbulence intensity, as in the case of pulsed actuation, or towards its suppression, as it is characteristic for the continuous operation. The modification of the secondary motion through the plasma actuator reflects restructuring of the separated flow within the diffuser, see Fig. 14. The turbulence intensity in the duct wall boundary layer transforming into a separated shear layer is closely correlated with the size of the flow reversal zone: higher turbulence level implies a higher momentum transport across the separated shear layer and a consequent depletion of the recirculation bubble. Accordingly, whereas the recirculation zone occupies the entire upper wall in the diffuser section and consequently a part of the straight duct (Fig. 12) in the baseline flow, the flow reversal vanishes almost completely in the case of the actuator pulsed with 40 % duty cycle, Fig. 14-left. In the continuous actuation case, the lower turbulence intensity influenced by significant secondary flow acceleration in the region corresponding to the actuator location causes the flow to separate at the side diffuser wall (Fig. 14-right), unlike in the baseline case.

Fig. 15 illustrates the development of the pressure coefficient on the bottom wall of the 3D diffuser configuration representing the practically most important outcome of the actuation. In all three diffuser configurations the continuous pressure decrease in the inflow duct is followed by a steep increase after entering the diffuser section. The different pressure recovery levels depend strongly on the mode of the plasma-based actuation of the secondary vortices in the inflow duct. The pressure recovery enhancement for the pulsed configuration is obvious compared to the baseline case without flow control. Accordingly, it represents the most efficient actuation, contributing to a strong turbulence activity

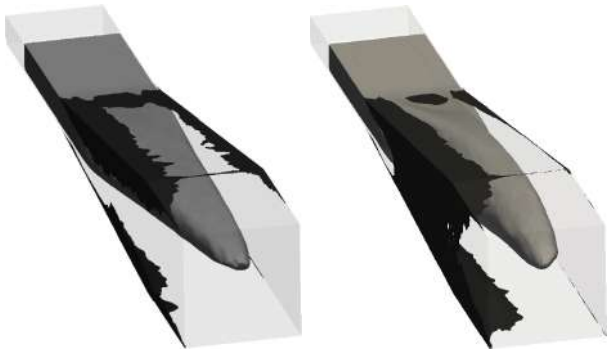

Figure 14: Iso-surfaces of axial velocity component $U/U_{bulk} = -0.01$ (black iso-surface) and 0.4 (gray isosurface) for two plasma-actuated diffuser cases with pulsed mode (left; 40% duty cycle) and continuous mode (right; 100% duty cycle)

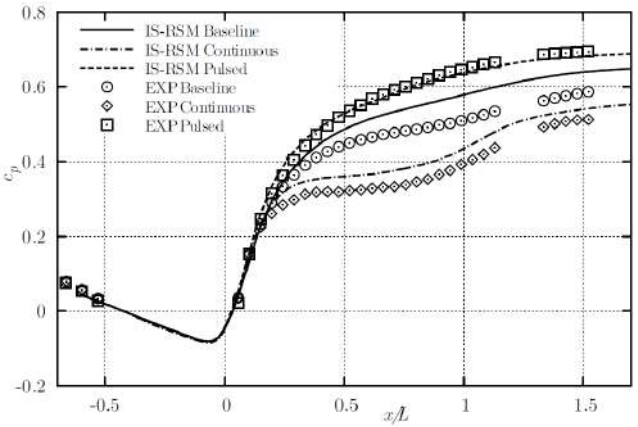

Figure 15: Flow in a 3D diffuser - Pressure coefficient distribution at the bottom diffuser wall for baseline and actuated cases (experiment by Grundmann et al., 2011)

intensification and causing significant reduction of the cross-sectional area occupied by the flow reversal.

Fig. 16 illustrates the instantaneous flow field past an in-line arrangement of a tandem cylinder visualized by the Q-criterion. The IS-RSM model's capability of resolving the turbulence unsteadiness enables development of turbulent structures in the gap and wake regions; the complex vortex shedding process and associated flow features are returned quantitatively accurate. The quantitative evidence of the results obtained by both conventional RSM and IS-RSM models is verified by contrasting their outcome along with the experimentally obtained results (Lockard et al., 2007; Neuhart et al., 2009), Figures 17-18. The tandem cylinder configuration can be regarded as a simplified version of a landing gear and can therefore serve as the first step in testing turbulence models for predicting the airframe noise. The unsteady pressure field is the most important flow variable acting as the noise-source representative. Conventional RANS models fail traditionally in predicting it because of their time-averaging rationale. Only unsteady interactions involving large scales can be reasonably captured. The unsteady feature of the pressure field is represented through the root-mean-square of the fluctuating pressure on downstream cylinder, Fig. 17. The model results are compared to those of the tripped experiments. It was experimentally found that the second cylinder is the main source of noise as the relevant $\overline{C'_{p'_{rsm}}}$ values are four to five times higher than those measured on the upstream

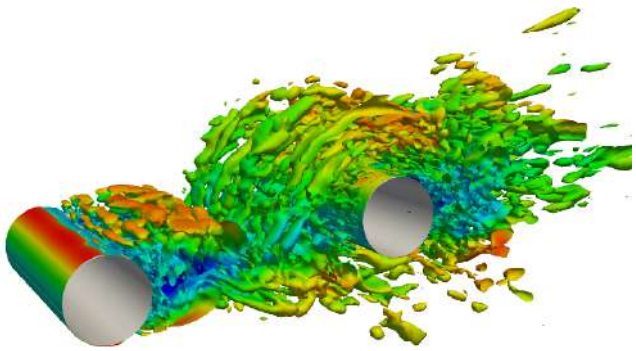

Figure 16: Instantaneous flow structure visualized by the Q-criterion (Q - iso-surfaces are coloured by the streamwise velocity magnitude) computed by the IS-RSM

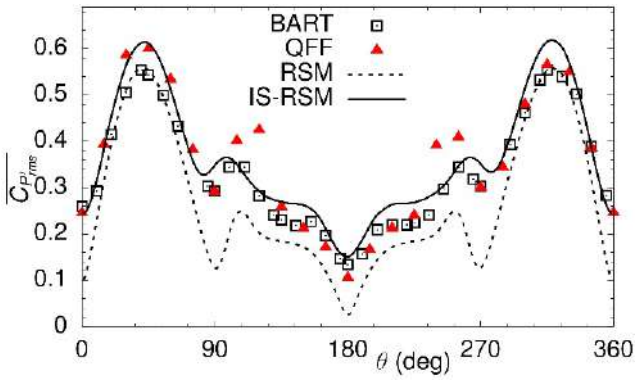

Figure 17: Root-mean-square (rms) of the fluctuating pressure at the downstream cylinder obtained by both conventional RSM and its instability-sensitive variant

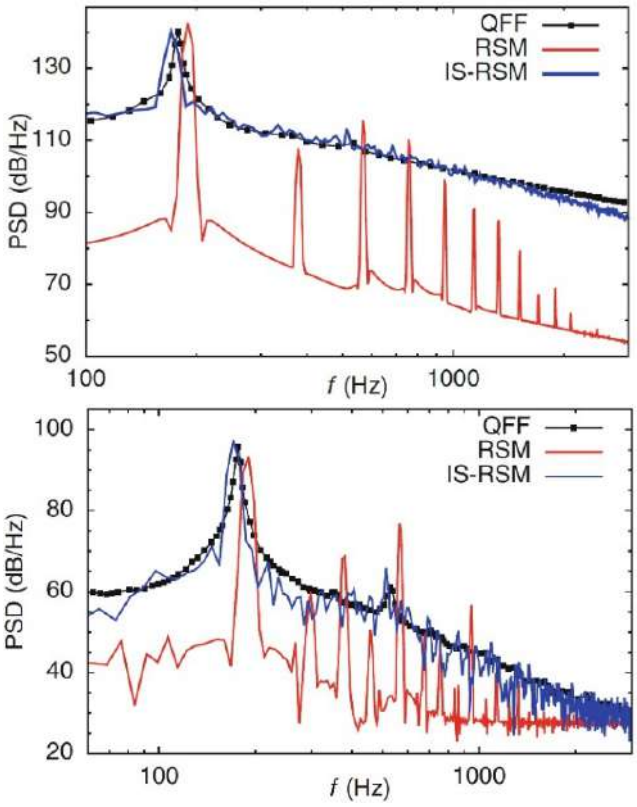

Figure 18: PSD of the surface pressure at $\theta = 45°$ on the downstream cylinder (upper) and far-field noise illustrated by the PSD of acoustic pressure at microphone position B (lower)

cylinder. The IS-RSM model results exhibit reasonable agreement in regard to both peak values and $\overline{C'_{p'_{rsm}}}$ distribution over the most of the cylinder surface, indicating the model's high potential for being used as a tool for the noise prediction. The RSM model results in a qualitatively correct shape of the $\overline{C'_{p'_{rsm}}}$ distribution but underestimates significantly its values at the entire cylinder surface Obviously that incapability of capturing the small-scale unsteadiness and their interaction with the large scales caused such a non-satisfactory outcome.

The time-dependent flow features are illustrated further in relation to the frequency spectrum of the surface pressure at $\theta = 45°$ at the downstream cylinder in Fig. 18-upper by the power spectral density (PSD). The IS-RSM results exhibit very good agreement with the QFF data while the RSM computations, due to the time-averaged rationale of the URANS approach, reproduce substantially lower PSD level with distinct discrete peaks, because only a weak unsteadiness of the large-scale motion could be resolved. Furthermore, the primary vortex shedding frequency corresponds to 190.3 Hz in relation to the RSM-related computation and 172.5 Hz to the IS-RSM-related one, with the latter comparing very well with the frequency of 178 Hz evaluated experimentally.

The power spectral density of the acoustic pressure following from the aeroacoustic computations based on the unsteady flow fields is presented for the far-field microphone position B in Fig. 18-lower (the results for microphones A and C are similar, but are not shown here for the sake of brevity). The PSD resulting from the IS-RSM computation is in very good agreement with the experimental data over the entire frequency range matching both the PSD peak value and the corresponding frequency quite well, unlike the RSM-related PSD result. The acoustic results, corresponding closely to the previously displayed PSD of the surface pressure, support the conclusion that the IS-RSM computations can generate appropriate acoustic sources in the flow field representing highly suitable background for reasonable determination and analysis of the far-field noise.

The next computational example deals with a plunging airfoil down-stroke-motion causing a vertical velocity component being imposed to the free stream velocity in an airfoil-fixed frame of reference, which implies a change of the effective angle of attack α_{eff}. When α_{eff} reaches a specific threshold, determined by the airfoil's leading edge curvature, the boundary layer rolls up and forms a leading-edge vortex (LEV) that accumulates negative vorticity (ω^-). The topology of the vortex growth and detachment phase can be described by a combination of half saddles, full saddles and nodes as identifiers as outlined by Rival et al. (2014), Fig. 19. Topologically, the LEV is bounded by two half saddles, one at the leading edge where the LEV is fed by the separated shear layer, and one at the rear reattachment point. While the LEV grows by accumulating mass, its reattachment point travels downstream until it reaches the trailing edge, Fig. 19a. In case of the presently considered boundary-layer eruption mechanism the LEV induces an adverse pressure gradient on the boundary layer that forms on the airfoil;s surface below the vortex towards the leading edge. When the velocity induced by the rotating LEV increases, the adverse pressure gradient reaches a critical value. Consequently, the boundary-layer beneath the vortex will separate and eject fluid of

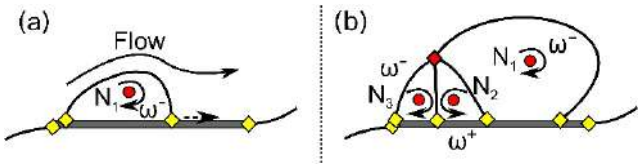

Figure 19: Boundary layer eruption mechanism: half saddle (yellow-coloured diamond), full saddle (red-coloured diamond) and node (N; red-coloured circle) - (a) growing LEV and (b) separation into primary (N1), secondary (N2) and tertiary (N3) vortex

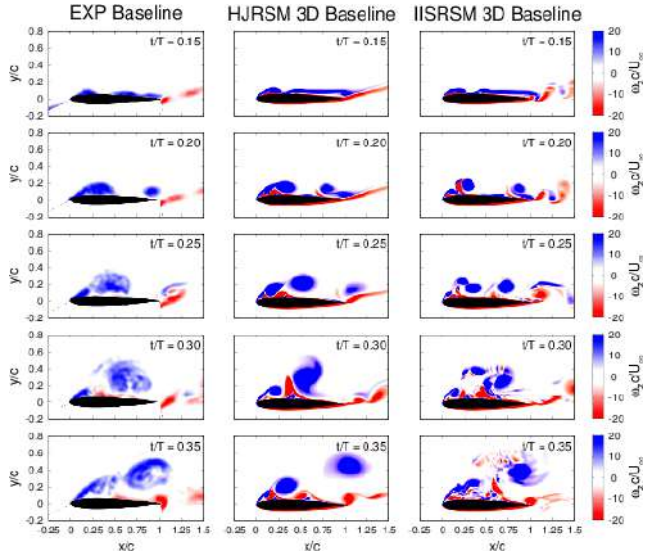

Figure 20: Temporal variation of the normalized spanwise vorticity of the LEV generated at a plunging airfoil

positive signed vorticity (ω^+) between vortex and leading edge. This upward ejection forms a secondary vortex termed N2 rotating opposite (ω^+) of the LEV (ω^-), Fig. 19b. To satisfy topological consistency, a tertiary vortex N3 (ω^-) arises ahead of the secondary vortex.

Figures 20 and 21, illustrating the temporal evolution of the spanwise vorticities and corresponding lift coefficient, compare directly the results obtained by three-dimensional computations employing both the baseline (HJ)RSM model and its eddy-resolving IIS-RSM counterpart with the experimental reference (Rival et al., 2014). The vorticity measurements represent the results of a 'single-shot' experiment (the computations are performed in the same way); the experimentally obtained C_L-coefficient represents an average over ten realisations.

The flow field obtained by the instability-sensitive IISRSM model has, unlike the flow field related to the HJRSM model employed within the conventional URANS procedure (featured by a very weak bulk flow unsteadiness in the spanwise direction), a true three-dimensional character, representing the outcome complying with the capability of the IISRSM model of capturing the turbulence fluctuations, also in the spanwise direction. The vorticity field (averaged over the spanwise direction; Fig. 20), depicted at the same time sequences as those obtained by the HJ-RSM model, show much finer structure. It is characterized by a somewhat longer sustainment of the shear layer feeding the Leading-Edge-Vortex, reflected also in a closer agreement of the lift coefficient with the experimental reference; this relates mostly to the decreasing part of the lift coefficient development, Fig. 21.

The final presently considered configuration focuses on

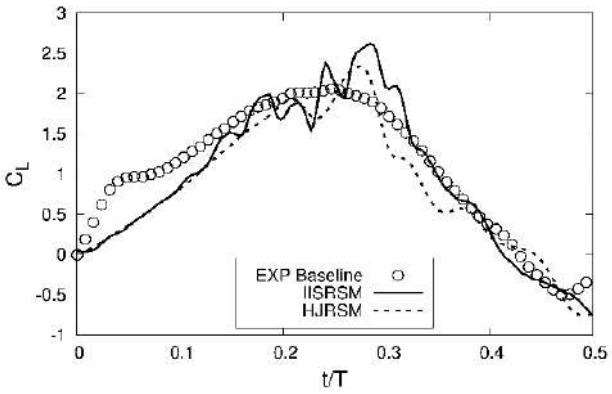

Figure 21: Temporal development of the lift coefficient

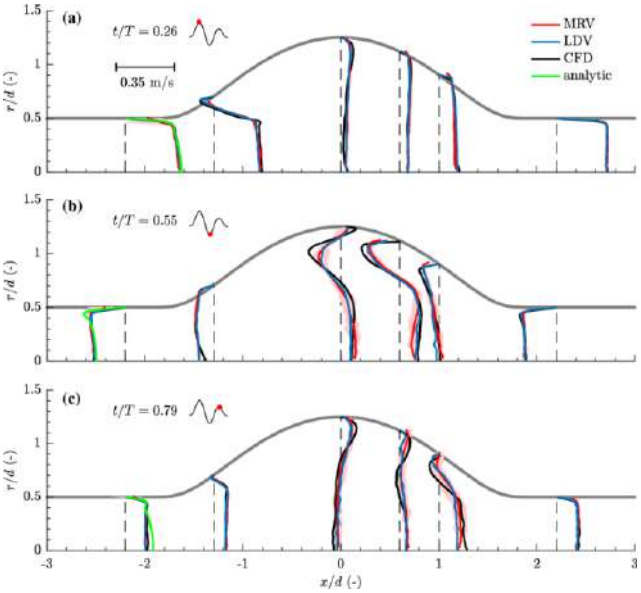

Figure 22: Spatial development of the mean axial velocity profile at the three time steps of peak volume flow rate

the physiologically pulsating flow in an aortic aneurysm for which the experimental reference has been provided (by employing the MRV and LDV measurement techniques) by Bauer et al. (2020), Figures 22-23.

Fig. 22 displays the mean axial velocity profile development within the aneurysm configuration at the three time steps corresponding to peak volume flow rates, acquired with MRV and LDV, compared to the CFD-ISRSM result and an analytic (laminar flow) solution. The temporal evolution of the flow resembling a physiological variation of the volume flow rate in the aorta, shown in small diagram in the upper left corner, relates to the so-called exercise conditions. The 'positive' peak flow Reynolds number (measured at the time instant $t/T = 0.26$) is 7649, whereas the one related to the 'negative' peak (at $t/T = 0.55$) corresponds approximately to 5550. The shaded red area indicates the variation of the MRV velocity profiles over the circumferential direction. The velocity field is typical of a pulsating flow with alternating reversal flow regions. Overal agreement between experimental and computational results is on a very high level. At the time instant $t/T = 0.26$ the flow detaches at the proximal neck due to the increasing flow rate forming a vortex ring which subsequently induces negative velocities at the wall, expands over the entire aneurysm cross-sectional area, travels downstream, weakens and finally

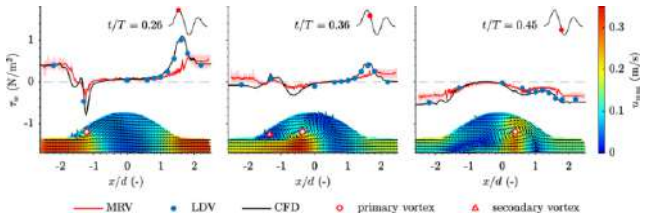

Figure 23: Spatial distribution of the WSS for different time steps during the cycle (with the corresponding values depicted on the left axis). The respective flow rate at each time step is denoted by red point in the upper right corners. The MRV-related circumferentially-averaged velocity field is given on the bottom (using the right colourbar and the lower axis)

dissipates. This vortex ring growth can be adequately followed in Fig. 23, highlighting also the generation and movement of both primary and secondary vortex cores in the flow field. In addition, the spatial distribution of the wall shear stress (WSS) at different time sequences within one physiological cycle is shown. Its alternating behaviour is closely correlated with the previously illustrated velocity field. The simulation results exhibit very good agreement with the LDV measurement, while the MRV results show some underestimations, especially in the regions and at the time steps where high WSS peaks are present.

4 Summary

An overview of the activities is presented related to development and application of differently-designed RANS-based eddy-resolving strategies for turbulent flow simulations, relying on both eddy-viscosity and Reynolds-stress modelling concepts. Numerous highly non-equilibrium flow configurations exhibiting different features is computationally studied and discussed along with reference experiments and other (LES/DNS) computational studies demonstrating the model feasibility and applicability in a broad range of complex, wall-bounded turbulent flows.

Acknowledgements

We acknowledge the financial support of the German Scientific Foundation (DFG-TRR150-B03; TR 194/56-1 and HE 1875/30-1), Federal Ministry for Economic Affairs and Energy (BMWi, GRS Project No. 1501417 and AiF-FVV IGF-Project No. 20224 N/2), EU Project ATAAC (with the grant number ACP8-GA-2009-233710) and the AVL List GmbH (Graz, Austria). Our special thanks go to Dr. Branislav Basara for an intensive cooperation in relation to the AVL-FIRE Code application and the PANS modelling strategy.

References

[1] AVL-FIRE Programme Manual, AVL List GmbH, Graz, Austria. CFD Solver Version 2017.1

[2] Basara, B., Krajnovic, S., Girimaji, S. and Pavlovic, Z. (2011): Near-Wall Formulation of the Partially Averaged Navier-Stokes Turbulence Model. AIAA Journal 49(12): 2627-2636

[3] Basara, B., Pavlovic, Z. and Girimaji, S. (2018): A new approach for the calculation of the cut-off resolution parameter in bridging methods for turbulent flow simulation. Int. J. Heat Fluid Flow 74: 76-88

[4] Bauer, A., Bopp, M. Jakirlić, S., Tropea, C., Shokina, N., Krafft, A. and Hennig, J. (2020): Analysis of the wall shear stress in a generic aneurysm under pulsating and transitional flow conditions. Experiments in Fluids 61(2):59, doi: 10.1007/s00348-020-2901-4

[5] Chang, C.-Y., Jakirlic, S., Dietrich, K., Basara, B. and Tropea, C. (2014): Swirling flow in a tube with variably-shaped outlet orifices: an LES and VLES study. Int. J. Heat and Fluid Flow 49:28-42, doi: 10.1016/j.ijheatfluidflow.2014.05.008

[6] Chang, C.-Y., Jakirlić, S., Basara, B. and Tropea, C. (2015a): Predictive capability assessment of the PANS- model of turbulence. Part I: physical rationale by reference to wall-bounded flows including separation. In "Advances in Hybrid RANS-LES Modelling 5". Notes on Numerical Fluid Mechanics and Multidisciplinary Design, Vol. 130, S. Girimaji et al. (Eds.), pp. 371-383, doi: 10.1007/978-3-319-15141-030

[7] Chang, C.-Y., Jakirlić, S., Basara, B. and Tropea, C. (2015b): Predictive capability assessment of the PANS- model of turbulence. Part II: application to swirling and tumble/mean-compression flows. In "Advances in Hybrid RANS-LES Modelling 5". Notes on Numerical Fluid Mechanics and Multidisciplinary Design, Vol. 130, S. Girimaji et al. (Eds.), pp. 385-398, doi: 10.1007/978-3-319-15141-031

[8] Chaouat, B. and Schiestel, R. (2005): A new partially integrated transport model for subgrid-scale stresses and dissipation rate for turbulent developing flows. Phys. Fluids 17 (065106): 1-19

[9] Girimaji, S.S. (2006): Partially-Averaged Navier-Stokes Model for Turbulence: A Reynolds-Averaged Navier-Stokes to Direct Numerical Simulation Bridging Method. J. Appl. Mech. 73: 413-421

[10] Grundmann, S., Sayles, E. Eaton, J.K. (2011): Sensitivity of an asymmetric 3D diffuser to plasma-actuator induced inlet condition perturbations. Experiments in Fluids 50(1): 217-231

[11] Hanjalić, K., Popovac, M. and Hadziabdić, M. (2004): A robust near-wall elliptic-relaxation eddy-viscosity turbulence model for CFD, Int. J. Heat and Fluid Flow 25: 1047-1051

[12] Hattori, H. and Nagano, Y. (2004): Direct numerical simulation of turbulent heat transfer in plane impinging jet. Int. J. Heat and Fluid Flow 25: 749-758

[13] Hattori, H., Iwase, M., Houra, T. and Tagawa, M. (2014): DNS and LES for turbulent heat transfer and mixing in T-junction channel flow. 10th Int. ERCOFTAC Symp. on Eng. Turbulence Modelling and Meas., Marbella, Spain.

[14] Heft, A., Indinger, T. and Adams, N. (2012): Introduction of a New Realistic Generic Car Model for Aerodynamic Investigations. SAE Technical Paper 2012-01-0168

[15] Heft, A. (2014): Aerodynamic Investigation of the Cooling Requirements of Electric Vehicles, PhD Thesis, Technical University Munich, Verlag Dr. Hut, ISBN 978-3-8439-1765-0

[16] Hirota, M., Mohri, E., Asano, H. and Goto, H. (2010): Experimental study on turbulent mixing process in cross-flow type T-junction. Int. J. Heat and Fluid Flow 31: 776-784

[17] Jakirlić, S., Kniesner, B., Kadavelil, G., Gnirß, M. and Tropea, C. (2009): Experimental and computational investigations of flow and mixing in a single-annular combustor configuration. Flow, Turbulence and Combustion 83(3):425-448, doi: 10.1007/s10494-009-9229-8

[18] Jakirlić, S., Kadavelil, G., Kornhaas, M., Schäfer, M., Sternel, D.C. and Tropea, C. (2010): Numerical and Physical Aspects in LES and Hybrid LES/RANS of Turbulent Flow Separation in a 3-D Diffuser. Int. J. Heat and Fluid Flow 31(5):820-832, doi: 10.1016/j.ijheatfluidflow.2010.05.004

[19] Jakirlić, S., Kniesner, B. and Kadavelil, G. (2011): On interface issues in LES/RANS coupling strategies: a method for turbulence forcing. JSME Journal of Fluid Science and Technology 6(1):56-72, doi: 10.1299/jfst.6.56

[20] Jakirlić, S., Kutej, L. Basara, B. and Tropea, C. (2014): Computational study of the aerodynamics of a realistic car model by means of RANS and hybrid RANS/LES approaches. SAE International Journal of Passenger Cars - Mechanical Systems 7(2):559-574, doi: 10.4271/2014-01-0594)

[21] Jakirlić, S. and Maduta, R. (2015a): Extending the bounds of "steady" RANS closures: towards an instability-sensitive Reynolds stress model. Int. J. Heat and Fluid Flow 51:175-194, doi: 10.1016/j.ijheatfluidflow.2014.09.003

[22] Jakirlić, S. and Maduta, R. (2015b): Sensitized RANS modelling of turbulence: resolving turbulence unsteadiness by a (near-wall) Reynolds stress model. Progress in Wall Turbulence 2: Understanding and Modeling. M. Stanislas, J. Jimenez and I. Marusic (Eds.), pp. 17-35, Springer Verlag, ERCOFTAC Series Vol. 23, doi: 10.1007/978-3-319-20388-1_2

[23] Jakirlić, S., Kutej, L., Hanssmann, D., Basara, B. and Tropea, C. (2016a): Eddy-resolving Simulations of the Notchback DrivAer Model: Influence of Underbody Geometry and Wheels Rotation on Aerodynamic Behaviour; SAE Technical Paper Series, Paper No. 2016-01-1062, doi: 10.4271/2016-01-1602

[24] Jakirlić, S., Kutej, L., Basara, B. and Tropea, C. (2016b): Numerische Fahrzeugaerodynamik am Beispiel von 'DrivAer' Modellkonfigurationen. Automobiltechnische Zeitschrift - ATZ, Band 118 (5/2016): 78-85, doi: 10.1007/s35148-016-0012-6 (also as Computational vehicle aerodynamics by reference to 'DrivAer' model configurations. ATZ Worldwide, Vol. 118 (5/2016): 76-83; doi: 10.1007/s38311-016-0008-6)

[25] Jakirlić, S., Kutej, L., Unterlechner, P. and Tropea, C. (2017): Critical assessment of some popular scale-resolving turbulence models for vehicle aerodynamics. SAE International Journal of Passenger Cars - Mechanical Systems V126-6EJ 10(1):235-250, doi: 10.4271/2017-01-1532

[26] Jakirlić, S., Kutej, L. Basara, B. and Tropea, C. (2018): Scale-resolving simulation of an 'on-road' overtaking maneuver involving model vehicles. SAE Technical Paper Series, Paper No. 2018-01-0706, doi: 10.4271/2018-01-0706

[27] Köhler, F., Maduta, R., Krumbein, B. and Jakirlić, S. (2020): Scrutinizing Conventional and Eddy-resolving Unsteady RANS Approaches in Computing the Flow and Aeroacoustics past a Tandem Cylinder. "New Results in Numerical and Experimental Fluid Mechanics XII", Notes on Numerical Fluid Mechanics and Multidisciplinary Design (NNFM), Vol. 142, Dillmann, A. et al. (Eds.), pp. 586-596, doi: 10.1007/978-3-030-25253-3_56

[28] Krumbein, B., Fooroghi, P., Jakirlić, S., Magagnato, F. and Frohnapfel, B. (2017a): VLES modeling of flow over walls with variably-shaped roughness by reference to complementary DNS. Flow, Turbulence and Combustion 99(3-4):685-703, doi: 10.1007/s10494-017-9867-1

[29] Krumbein, B., Jakirlić, S. and Tropea, C. (2017b): VLES study of a jet impinging onto a heated wall. Int. J. Heat and Fluid Flow 68:290-297, doi: 10.1016/j.ijheatfluidflow.2017.09.020)

[30] Krumbein, B., Termini, V., Jakirlić, S. and Tropea, C. (2018): Flow and heat transfer in cross-stream type T-junctions: A computational study. Int. J. Heat and Fluid Flow 71:179-188, doi: 10.1016/j.ijheatfluidflow.2018.03.013

[31] Krumbein, B., Maduta, R., Jakirlić, S. and Tropea, C. (2020): A scale-resolving elliptic-relaxation-based eddy-viscosity model: development and validation. "New Results in Numerical and Experimental Fluid Mechanics XII", Notes on Numerical Fluid Mechanics and Multidisciplinary Design (NNFM), Vol. 142, Dillmann, A. et al. (Eds.), pp. 90-100, doi: 10.1007/978-3-030-25253-3_9

[32] Kütemeier, D., Wegt, S., Maden, I., Kissing, J., Maduta, R., Kriegseis, J., Jakirlić, S and Tropea, C. (2019): Plasma-actuated Lift Enhancement of a Plunging Airfoil: A Computational Study. Paper No. AIAA-2019-0305, SciTech 2019, San Diego, CA, USA, January 7-11, doi: 10.2514/6.2019-0305

[33] Lockard, D.P., Khorrami, M.R., Choudhari, M.M., Hutcheson, F.V. and Brooks, T.F. (2007): Tandem cylinder noise predictions. AIAA Paper 2007-3450

[34] Maden, I., Maduta, R., Kriegseis, J., Jakirlić, S., Grundmann, S. and Tropea, C. (2015): Plasma-actuated manipulation of secondary flow towards pressure recovery enhancement in a 3D diffuser modelled by an eddy-resolving second-moment closure. Flow, Turbulence and Combustion 95(2-3):377-398 doi: 10.1007/s10494-015-9641-1

[35] Maduta, R., Ullrich, M., Jakirlić, S. (2017): Reynolds stress modelling of wake interference of two cylinders in tandem: conventional vs. eddy-resolving closure. Int. J. Heat and Fluid Flow 67B:139-148, doi: 10.1016/j.ijheatfluidflow.2017.07.012

[36] Menter, F. and Egorov, Y. (2010): The Scale-adaptive Simulation method for unsteady turbulent flow predictions. Part 1: theory and model description. Flow, Turbulence and Combustion 85: 113-138

[37] Neuhart, D.H., Jenkins, L.N., Choudhari, M.M. and Khorrami, M.R. (2009): Measurements of the flow field interaction between tandem cylinders. AIAA Paper 2009-3275

[38] Rival, D., Kriegseis, J., Schaub, P., Widmann, A., Tropea C. (2014): Characteristic length scales for vortex detachment on plunging profiles with varying leading-edge geometry. Exp. in Fluids 55:1-8

[39] Rotta, J. C., 1972. Turbulente Strömungen. Eine Einführung in die Theorie und ihre Anwendung. Teubner Verlag Stuttgart (ISBN-10: 3519023164; ISBN-13: 978-3519023166)

[40] Schreffl, N. (2008): Instationaere Aerodynamik von Kraftfahrzeugen - Aerodynamik bei Ueberholvorgang und boeigem Seitenwind. PhD Thesis, Technical University of Darmstadt, Germany, Shaker Verlag Aachen, ISBN 978-3-8322-7010-0

[41] Spalart, P.R., Jou, W.-H., Strelets, M., Allmaras, S. (1997): Comments on the feasibility of LES for wings and on a hybrid RANS/LES approach, 1st AFOSR Int. Conf. on DNS and LES. In: Liu, C., Liu, Z. (Eds.), Advances in DNS/LES. Columbus, OH, Greyden Press, pp. 137-147

[42] Spalart, P.R. (2009): Detached-Eddy Simulation. Annu. Rev. Fluid Mech. 41: 181-202

[43] Speziale, C.G. (1998): Turbulence modeling for time-dependent RANS and VLES: A review. AIAA Journal 36(2):173-184

Elliptic-Relaxation Hybrid RANS-LES (ER-HRL) for Complex Wall-Bounded Fluid and Heat Flows

M. Hadžiabdić[1] and K. Hanjalić[2,3]

[1] *International University of Sarajevo, Hrasnička cesta 15, 71210 Ilidža, Sarajevo, Bosnia and Herzegovina*
[2] *Delft University of Technology, Bld. 58, Van der Maasweg 9, 2629 HZ Delft, The Netherlands*
[3] *University of Sarajevo, Vilsonovo šetalište 8, Sarajevo 71000, Bosnia and Herzegovina*

Abstract

The paper summarizes the salient features and some recent extensions and scrutiny of the Elliptic-Relaxation Hybrid RANS-LES (ER-HRL) scale-resolving method [1, 2]. The physically transparent model with minimal empirical contents employs the elliptic- relaxation wall-integration (WIN) eddy-viscosity $\zeta - f$ RANS model [3] for the wall-adjacent regions and the dynamic Smagorinsky LES for the outer flow, blended by a simple grid-detecting function. The elliptic-relaxation, accounting for inviscid wall-blocking effects, makes the model particularly suited for predictions of flow, heat and mass transfer in passages bounded by multiple and irregular walls. The solution of the transport equation for a scalar surrogate of the wall-normal stress accounts for the near-wall stress anisotropy which enhances sensitivity of the RANS model to outer LES perturbations. The adopted blending function, together with the back-scatter from the dynamic LES and the enhanced receptivity of the RANS ensure a fast transition between the two regions and returns predictions with practically no "gray area" around the RANS-LES interface without any artificial remedy. A new feature of the method is the option for automatic blending of the RANS model with or switching to the Simplified Analytical Wall Functions (SAWF) [4] when the wall-nearest grid point happens to be outside the viscous sublayer, suited especially for coarse, automatically generated computational grids. The paper outlines the modelling rational and its effect on the the grey-zone, and provides some illustration from a palette of flows and heat transfer in complex turbomachinery passages.

1 The modelling rationale

Since the appearance of Detached-Eddy Simulations (DES), [5], the hybrid LES-RANS methods have been gaining in popularity, emerging as the most viable option for CFD of real-scale complex applications, especially for external flows. Entrusting the LES to resolve the important turbulence scales in the flow bulk, the modelling empiricism is confined to a relatively small wall-adjacent RANS region, arguably justifying the use of a simple one- or two-equations eddy-viscosity model. However, in internal flows with bounding walls of complex topology such as encountered in heat exchanges (finned, ribbed, dimpled and other surface textures), turbomachinery (internal and external blade cooling, tip leakage, labyrinth seas), IC engines (valves, cooling jackets), electronics cooling and others, and especially when heat and mass transfer are in focus, the choice of the near-wall RANS can be essential for accurate predictions of friction, heat and mass transfer and other wall phenomena, e.g, condensation, evaporation, cavitation, particle deposition, erosion, combustion, chemical reactions [6].

The ER-HRL, summarised in the Appendix, employs in the RANS region the three-equation eddy viscosity model based on the conventional $k-\varepsilon$ concept, enriched by the transport equation for $\zeta = v^2/k$, where v^2 is the Durbin's scalar surrogate for the wall-normal turbulent stress components. The equation set is complemented by a simple, elliptic equation for the relaxation function f [7] with the original time- and length-scale realisability limiters, hence labelled as the $k-\varepsilon-\zeta-f$, (or simply the $\zeta - f$) model. Compared with the parent $v^2 - f$ model of Durbin, the $\zeta - f$ requires less stiff wall boundary conditions and proved generally to be more robust and faster converging.

The rationale behind the ER-HRL model ([1], [2], [8]) is to intervene in the sink term of the k-equation with a grid detecting parameter α (hence sometimes also labelled as α-HRL) by which the RANS eddy viscosity is suppressed to the subgrid-scale value of LES at the matching interface. The full set of equations is provided in Appendix 1; here we list only the k-equation and the two limiters that control the switching from one to another model:

$$\frac{Dk}{Dt} = D_k + P_k - \alpha\varepsilon,$$
$$\alpha = max(1, \frac{L_{RANS}}{\Delta}),\ \nu_t = max\left(\nu_t^{RANS}, \nu_t^{LES}\right)$$

where k is the (RANS) modelled turbulent kinetic energy, ε its dissipation rate, $L_{RANS} = k^{1.5}/\varepsilon$ and $L_{LES} = \Delta = C_\Delta\ (\Delta V)^{1/3}$.

To function in a hybrid mode with LES in the outer flow region, the k-equation contains a blending function associated with the energy dissipation rate ε, which, in the spirit of DES practice, switches the implicit characteristic turbulence length scale from the RANS energy containing scale L_{RANS} to the characteristic LES subgrid-scale when it becomes smaller than L_{RANS}. The model contains one more switching criterion which chooses the larger eddy viscosity among ν_t^{RANS} and ν_t^{LES}. Close to a wall $\alpha = 1$ and the model acts as in the URANS mode. Away from walls, where $L_{RANS} > \Delta$, $\alpha > 1$, k is damped, thus diminishing ν_t^{RANS}. Eventually, when $\nu_t^{RANS} < \nu_t^{LES}$, the second constraint is activated and the conventional LES is resumed.

Depending on the active $\nu_t = max\left(\nu_t^{RANS}, \nu_t^{LES}\right)$, the model provides the RANS or the subgrid-scale LES stress in the corresponding averaged or filtered momentum equations.

$$\tau_{ij}^t - \frac{1}{3}\tau_{kk}^t \delta_{ij} = -2\nu_t \overline{S_{ij}}$$

where S_{ij} denotest the RANS or filtered rate of strain tensor.

Once α becomes greater than 1, the RANS modelled eddy viscosity starts to decrease towards the LES sgs value, while the resolved energy increases. Thus, for $\alpha > 1$, the turbulence properties obtained from the $\zeta - f$ model do not represent any longer the characteristic large-eddy structures so that the length scale L_{RANS} should be defined in terms of the total turbulent kinetic energy, $k_{tot} = k_{res} + k_{mod}$. In general, k_{tot} is not known in advance, and the simulations can be started by using the mixing length $L_{RANS} = \kappa y$ until the flow structures are reasonably established, and then replaced by $L_{RANS} = k_{tot}^{1.5}/\varepsilon$.

Using the standard L_{RANS} throughout the model may sometimes pose some numerical instabilities in complex flow configurations (as shown below) which can also be easily remedied by switching to $L_{RANS} = \kappa x_n$, where x_n is the local distance from the nearest wall. It is noted, however, that, unlike in DES and similar schemes, here L_{RANS} serves only to define the blending-control parameter α, thus entering the turbulence model only in a narrow buffer region where $\alpha > 1$, which is usually only few grid nodes between the true URANS ($\alpha = 1$) and the full LES ($\nu_t = \nu_t^{LES}$).

For flows at very high Re numbers and especially when intentionally or in the course of automatic mesh generation the wall-nearest grid point lies in the buffer or in the fully turbulent wall region, the model activates respectively either a blending of the full wall-integration (WIN) model with the Simplified-Analytical Wall Functions (SAWF), or a full switching to the SAWF to provide the wall boundary conditions [4]. The SAWF and their blending with wall-integration (WIN) are summarized in Appendix 2.

2 Grey area and model scrutiny in a plane channel flow

The RANS-LES interface mismatch known as the "grey area" in hybrid LES-RANS strategy for computation of wall-bounded turbulent flows has been a concern in just about all popular hybrid approaches irrespective of the modelling rationale. The anomaly, notably revealed by an excessive slope (a kink) of the logarithmic velocity profile in equilibrium wall flows ("log layer mismatch" [9]), has been attributed to the excessive RANS eddy viscosity pervading too far into the LES zone, thus suppressing instabilities, stochastic fluctuations and, more importantly, weakening the LES resolution of the large-scale stress-bearing eddies. The total (modelled plus resolved) shear stress appears too low, generating too high velocity gradient to match the momentum balance for the imposed pressure gradient or mass flow rate.

Some years back, we noticed that our ER-HRL model shows no significant grey area anomaly without introducing any specific remedy. Based on that experience and other testing we argue that the cause of the anomaly can be rooted primarily in the way the RANS and LES solutions are blended, but also in the insufficient sensitivity and receptivity of the particular wall RANS model to external (LES) perturbations.

Various remedies have been proposed to alleviate the grey area, some focusing on the modifications of the subgrid scale either by adding artificial forcing in form of synthetic turbulence or an uncorrelated stochastic function [10]. Another method proposed recently [11], introduces the commutation terms at the RANS-LES interfaces in the mean momentum and the $k - \omega$ turbulence transport equations, claimed to rapidly reduce the turbulent viscosity across the RANS-to-LES interface thus enhancing the resolved turbulent fluctuations and a rapid establishment of the proper LES.

In our earlier studies,[12, 13], one-equation ($k - l$) and two-equations ($k - \varepsilon$) RANS models and the dynamic Smagorinsky or one-equation subgrid-scale models were matched by the compatibility conditions for velocity and turbulent viscosity imposed across the interface by way of the RANS eddy-viscosity coefficient C_μ. These conditions, tested in a channel flow, are extracted dynamically as the simulation progresses. One of the interesting findings was that using the averaged C_μ , which to a large degree filters out the transmission of LES fluctuations to the RANS, resulted in a pronounced kink in the logarithmic velocity profile. However, the anomalous kink almost disappeared when applying the highly fluctuating instantaneous C_μ values, supporting the argument that a lack of stochastic fluctuations in the interface region is one of the roots of the grey area anomaly.

The RANS sensitivity to LES perturbation across the interface were examined in [10-12] by analysing the response of one- and two-equation ($k - l$, $k - \varepsilon$) RANS models to the true instantaneous LES velocity and pressure fields generated by a priori fine-resolved LES for the complete channel and imposed as dynamic boundary condition at the RANS outer edge - mimicking the interface in hybrid approaches. The results showed a striking qualitative similarity of the RANS and LES results for instantaneous velocity profiles as well as histograms of streamiwise velocity at various distances from the wall. This also applies to the response of the wall friction velocity, as well as for the correlation between the instantaneous wall-friction and fluid velocity and their angles in the wall-parallels planes with respect to the streamwise direction. Those findings, at the time very encouraging, proved over the time to be insufficient for ruling out the RANS sensitivity and receptivity as issue in hybrid RANS/LES strategies presumably because the test reported in [2, 12, 14] involved only one-way (LES to RANS) feeding of information. In hybrid schemes, the RANS and LES interact and feedback to each other, most probably diminishing the capacity of RANS to sustain the true physical LES fluctuations, feedback and modify the neighbouring LES in and around the interface. Arguably, such effects and interactions should depend in the natural sensitivity and receptivity of a RANS model depending on its physical foundation and capability to account for local turbulence anisotropy, elliptic wall blocking and other model features.

We show some results of ER-HRL computations, starting with a fully developed plane channel flow at $Re_\tau = 2000$ and 20000 and discuss in parallel the model features that add to a self-mitigation of the grey area. Figure (1) shows the logarithmic plot of the mean velocity with indicated locations of the activation of the RANS-LES blending function $\alpha = 1$, and the switching from the RANS to LES eddy viscosity. It is noted that all results are shown for the relatively coarse computational grids of $N_x \times N_y \times N_z = 64 \times 64 \times 32$ (total ≈ 130000 cells) for $Re_\tau = 2000$ and $N_x \times N_y \times N_z = 64 \times 90 \times 32$ (total ≈ 180000 cells) for $Re_\tau = 20000$, on a domain of $2\pi h \times 2h \times \pi$.

As shown in Figure (1) (and in more details also in [6]), the model switching locations ($\alpha > 1$ and $\nu_t^{RANS} =$

ν_t^{LES}) show that a relatively large portion of the flow is handled by the URANS, whereas the transition zone between the two limiters varies depending on the grid clustering, but without noticeable effect on the mean velocity distribution.

The log layer mismatch is illustrated by the standard DES97 velocity profile in Figure (1)(a), but notably absent in the ER-HRL plot for both Re numbers considered, as seen also in Figure (1)(b). The performance of the ER-HRL model on the same grid but with a very different distribution of wall normal grid cells (Δy) is illustrated for $Re_\tau = 20000$ in Figure (1)(b) for the wall nearest grid points at $y^+ = 0.5$, 15 and 310. While in the first case the ER-HRL is solved up to the wall (WIN mode), in the third case the wall boundary conditions are provided fully by SA Wall Functions, activated automatically. In the second case for $y^+ = 15$, a blending of the WIN solution with SAWF is applied (Appendix 2).

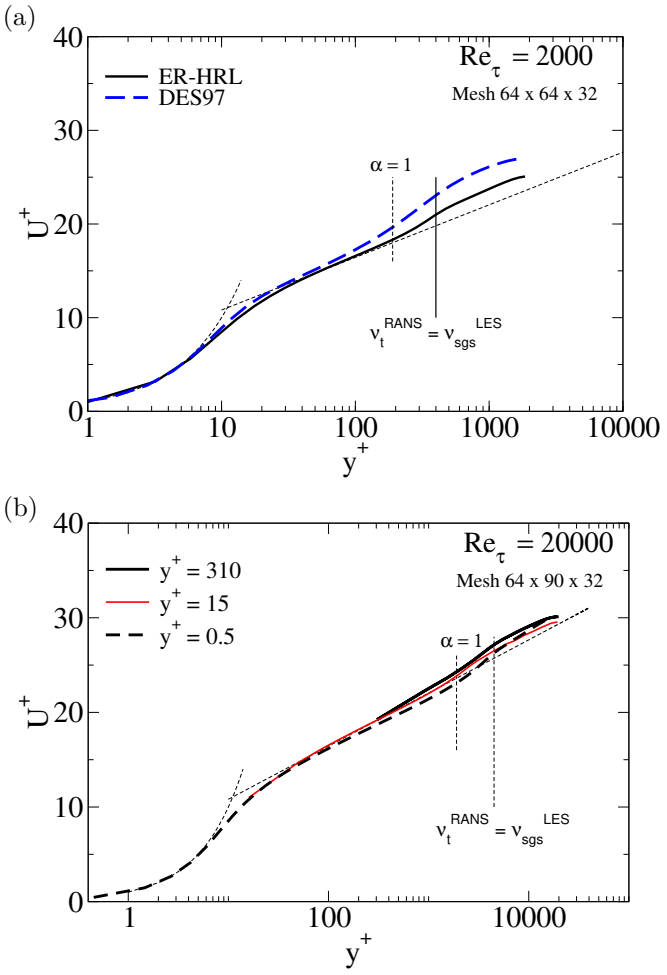

Figure 1: Velocity profiles for a moderate grid for $Re_\tau = 2000$ and 20000, with locations of blending fucntion activation ($\alpha = 1$), and the RANS-LES switching

A plot of the resolved and modelled turbulent shear stress, normalised with the corresponding (different) wall shear stress in Figure (2) provides some indication of the origin of log-law anomaly displayed in Figure (1)(a). As seen, DES97 generates a substantially larger modelled stress which permeates much further into the LES area suppressing resolution of energy-containing and stress bearing eddies. The latter effect seems stronger so that the resolved DES activity in the overlapping area is insufficient to make it up to the proper total shear stress required to match the imposed pressure gradient or mass flow rate.

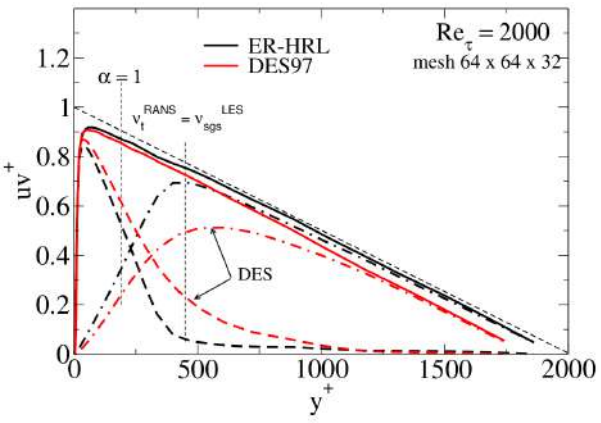

Figure 2: Shear stress across the half-channel showing the modelled, resolved and total values for EF-HRL and standard DES97

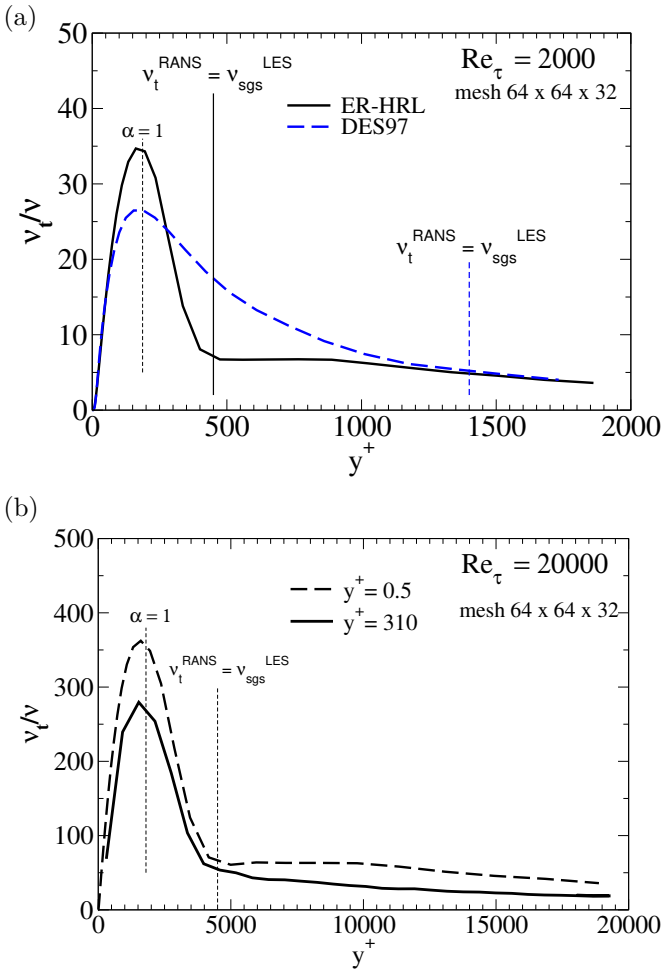

Figure 3: RANS-LES blending function. (a) DES97 and ER-HRL for the same Re and grid; (b) ER-HRL for $Re_\tau = 20000$ for different near-wall gird distributions

A further insight into the matter can be gained from a scrutiny of the RANS-LES effective eddy viscosity. Figure (3)(a) compares the acting eddy-viscosities in the ER-HRL and DES97 models for the same grid and Re number. Whereas in both cases the near-wall plots are almost indistinguishable up to $y^+ = 100$, further away from the wall the distributions are very different. Apart from different peak values located in the present case

for both models at almost the same wall distance of $y^+ = 200$, which, incidentally, do not seem to be particularly influential, the major difference appears in the transition area around the RANS-LES interface. A striking feature of the ER-HRL eddy viscosity is its fast drop to the sgs value, here at $y^+ = 450$ when the full LES is activated. In contrast, the DES eddy viscosity diminishes gradually and reaches the sgs value much further away, at $y^+ = 1400$. This is also reflected in the modelled stress distribution in Figure (2). The too high modelled stress and the consequent low resolved stress in a relatively large transition region for $100 < y^+ < 1400$ coincides with the log-law mismatch shown in Figure (1)(a). Thus, as stated above, the shape of the blending function determining the modification of the eddy-viscosity in the area around the RANS-LES interface, and the sensitised receptivity of the ER RANS model to LES unsteadiness seem the major agencies in self-mitigating the grey-area. Some benefits in the resolution sensitivity can also be attributed to the inherent backscatter from the dynamic LES sgs as identified in the full wall-resolved LES.

Some more insight into the quality of predictions and grey-area issue can be gained by comparing power spectra from ER-HRL and DES-like[1] solutions plotted at different wall distances, as shown in Figure (4) for $Re_\tau = 2000$. First we note that both approaches return relatively smooth spectra typical of channel flows at all locations considered including those deeply within the RANS layer. Very close to the wall, at $y^+ = 10$, where both RANS models (the $\zeta - f$ in ER-HRL and Spalart-Allmaras (S-A) in DES) the two spectra are close to each other at very low wave numbers, but differ notably for higher frequencies despite practically identical eddy viscosity (Figure (3)a). The ER-HRL resolves turbulence fluctuations better than DES presumably because of its better sensitivity to outer perturbations generated by LES. The difference in spectra increases with the wave number indicating also that ER-HRL resolves better the small sales, as shown in Figure (4)a by a sharper spectrum drop in DES. Further away at $y^+ = 100$, roughly where the two eddy viscosities begin to part (Figure (4)b), and at $y^+ = 260$ corresponding to the locations of peak eddy viscosity in both models (Figure (4)c), the spectra show similar features and differences, being slightly closer to each other in the highest wave-number range, especially at the latter location. Of a particular interest are the spectra in the interface zone shown in Figure (4)d for $y^+ = 600$, where ER-HRL has already switched to the true LES, whereas in DES it is still in the blending zone with a significant RANS eddy viscosity. Here the spectra are closer to each other, but the ER-HRL shows more energy over the whole wave-number range, the difference appearing in particular at the end with dissipation tails characteristic for insufficiently resolved LES on coarser grids. We believe that a better spectral resolution and higher energy contents in ER-HRL model compared to DES over the whole spectral range for all locations considered explain, at least in part, the practical absence of the grey-area anomaly making redundant any artificial forcing in the RANS-LES interface area.

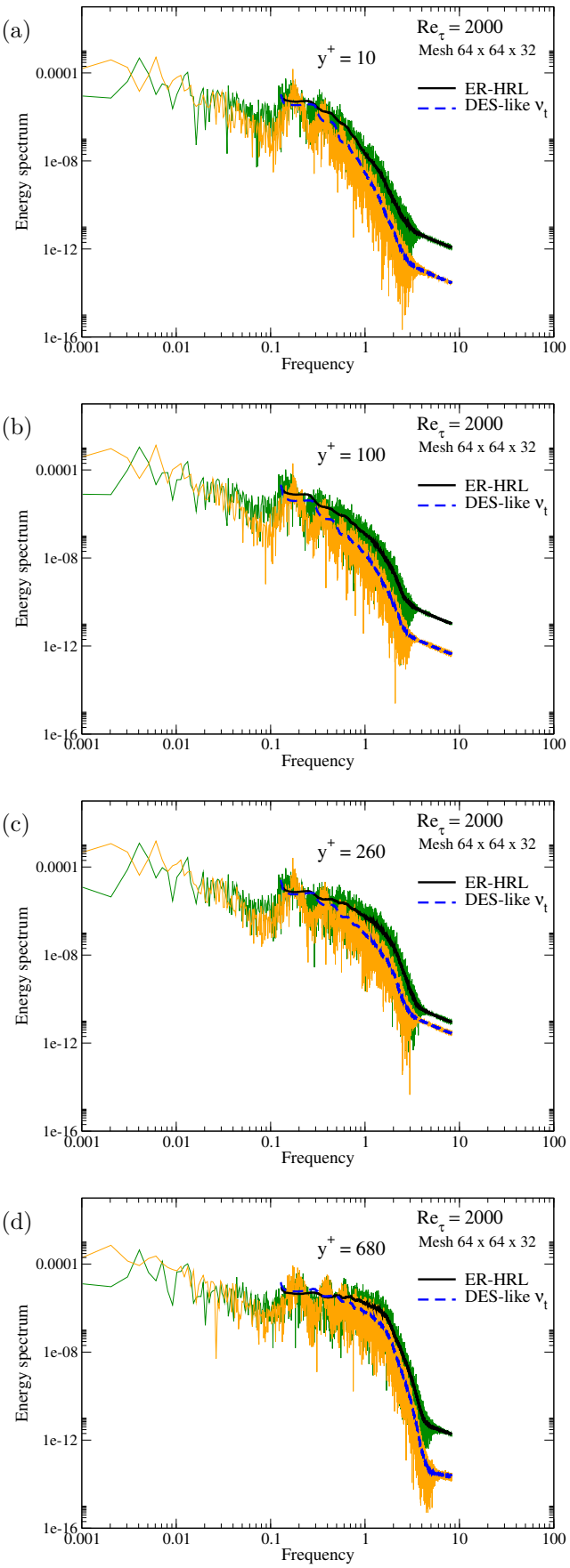

Figure 4: Energy spectra for DES and ER-HRL (a) Buffer region, (b) and (c) interface zone, (d) LES region

[1]The DES97 results shown here were performed some time ago [1] but without collecting spectral data. To generate spectra for the present comparison, we performed hybrid simulations by mimicking the S-A and DES blended eddy viscosity, hence the label "DES-like".

3 The ER-HRL in complex flows

3.1 Internal cooling of G-T blades

Without going much into details, we present a small selection of illustrations of the ER-HRL performance in two flows with complex wall-bounded configurations encountered in turbomachinery, from earlier publications co-authored by our colleagues D. Borello, G. Delibra and F. Rispoli [6, 15, 16, 17, 18, 19, 8].

Figure (6)(a) shows a sketch of the typical gas-turbine blade cooling system that includes impingement, effusion and enhanced interior convection. Here the attention is focused on the latter method in which the blade interior of the trailing part is fitted by a matrix of staggered cylindrical pins. The pins act primarily as promoters of vortex shedding and turbulence to enhance blade cooling by interior cold air flow. A simplified setup with parallel, differentially heated walls mimicking the experiment of [20] for two Re numbers (10^4 and $3 \cdot 10^4$) was simulated by URANS, LES and ER-HRL aimed at testing the optimum computational strategy. Details have been described in [2, 15, 18, 19, 8]. The complexity of the vortical and plume structures that govern heat transfer and its enhancement is illustrated by wall-resolved LES (available only for $Re = 10^4$) in Figure (6)(b),(c). We discuss briefly some results obtained by ER-HRL with moderate grids: $1.3 \cdot 10^6$ and $4.4 \cdot 10^6$ respectively for $Re = 10^4$ and $3 \cdot 10^4$, compared with $5 \cdot 10^6$ and $15 \cdot 10^6$ for LES (the latter grid proving insufficient). Regardless of the models applied, a much coarser grid used in the ER-HRL cannot reproduce the wide spectrum of scales shown in Figure (6)b, especially if URANS covers substantial portion of the flow, as illustrated in Figure (7). But, as shown in Figure (8) and Figure (9) the lack of small-scale resolution in the near-wall area has been well compensated by the applied $\zeta - f$ RANS model in predicting the wall heat transfer.

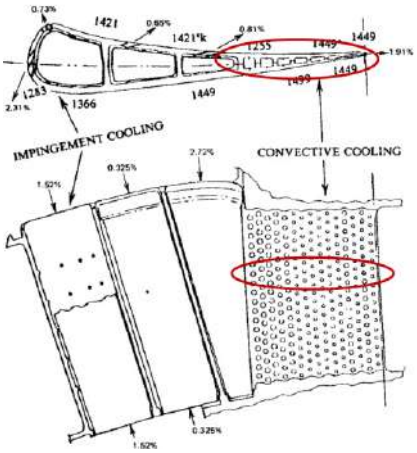

Figure 5: A sketch of gas-turbine blade cooling

Figure (8) and Figure (9) show the time averaged distribution of the Nusselt number on the heated wall, compared with the experiments (Figure (8)) and also with URANS using the same $\zeta - f$ model in the whole domain (Figure (9)). The ER-HRL showed superior results, and for $Re = 10^4$, also in close agreement with the LES [15, 8]. Although in both the HRL and URANS the same ($\zeta - f$ RANS) model is responsible for the wall heat transfer, the key difference is in the intensity of the outer forcing from LES that influences the separation dynamics of vortex shedding especially behind the first pin row.

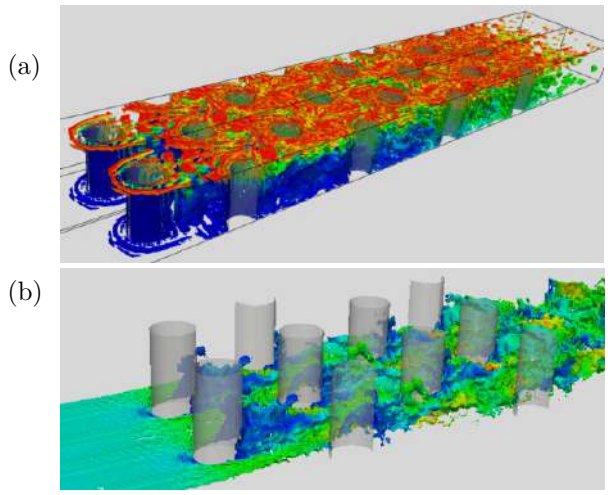

Figure 6: LES of flow in internal pinned passage ($Re = 10,000$). (a)-vortical structures coloured by temperature (top waall heated); (b)- thermal plumes (T=294K) coloured by velocity magnitude (bottom wall heated) [18]

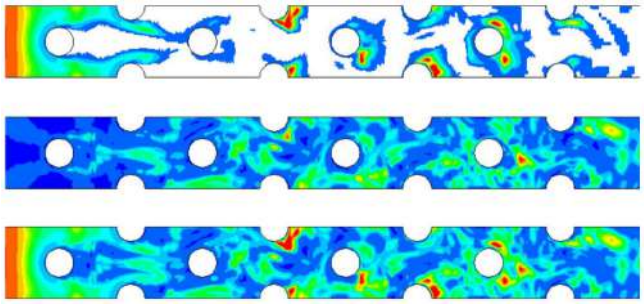

Figure 7: Viscosity contours in the midplane ($z = 1.0$. Pins 2, 4, 6 and 8 (laterally staggered) are also shown (shaded). Top rows: ν_t^{RANS}; center: ν_t^{LES}; bottom: effective viscosity [8]

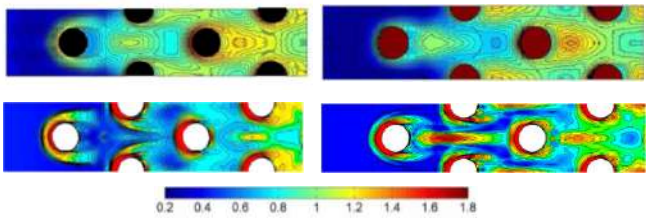

Figure 8: Time averaged Nu number on the heated wall (normalised with the area-averaged Nu_{av}). Left: $Re = 10.000$, Right: $Re = 30000$. Top: Exp. [20], Bottom; ER-HRL [8]

3.2 Blade-tip leakage and trailing vortices in compressor cascades

The unproductive but unavoidable blade-tip leakage, secondary flows in blade passage and trailing vortices in the cascade wake are the other serious causes of energy loss, especially in turbo-compressors. Here CFD can bring much enlightenment and help in the design optimisation. A sketch of a simplified low-speed compressor cascade with a casing, Figure (10), illustrates the critical phenomena that pose challenge to modelling [21]. We discuss briefly some salient flow features and challenges for CFD and show some results for stagnant and moving casing using the ER-HRL and URANS. More details can be found in [17, 16].

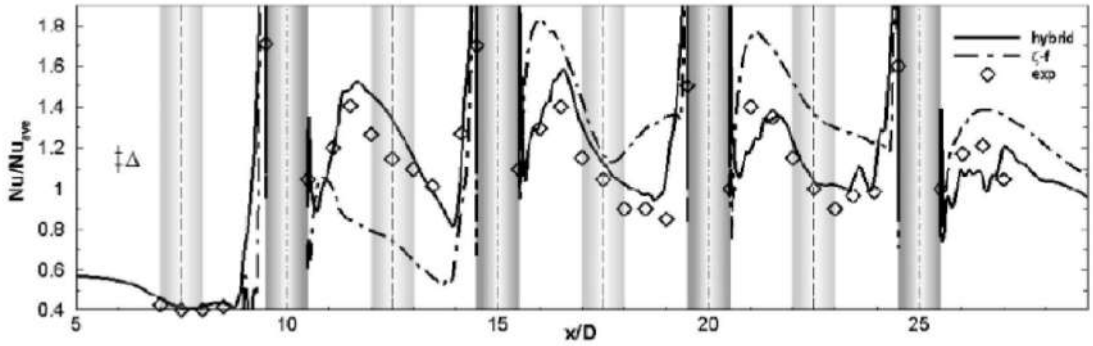

Figure 9: Nusselt number Nu/Nu_{av} on the heated endwall along the line cutting pins 2, 4, 6 and 8 for $Re = 10^4$. From [8]. Symbols: experiments [20]

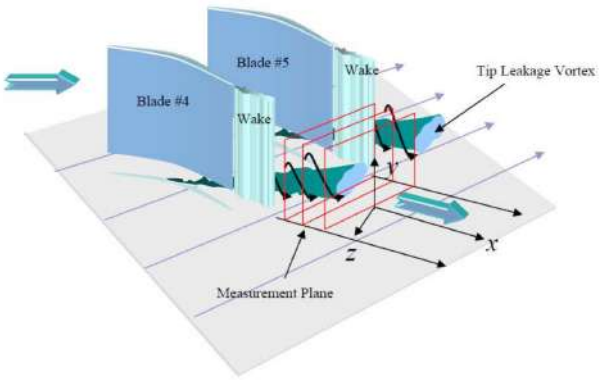

Figure 10: A sketch of the cascade and tip leakage vortices; measuring planes indicated by red quadrangles behind the cascade [21]

Fast distortion dominated by pressure and inviscid effects in the tip clearance makes the results relatively insensitive to turbulence modelling (Figure (11)), though the model plays a role in capturing the boundary layer properties on the moving casing. However, the formation and development of the tip vortex and its interaction with the blade wake (Figure (12)) puts a high demand on the model. Indeed, the results for the wake showed to be more model-sensitive as illustrated in Figure (13). The experimental data available in the planes indicated by red-quadrangles in Fig. 10, make it also possible to provide some quantitative test of the performances of the models considered. Figure (13), depicting the wall-normal velocity field in the cross-plane at the first measuring plane ($x/ca = 1.37$), shows that only the ER-HRL captures properly the locations as well as the velocity intensity in the two counter-rotating tip-leakage vortices. The linear and non-linear $\zeta - f$ RANS models, when applied in the whole domain (URANS computations), show very similar patterns in between, as well as the vortices strengths and their distance as in the experiment, but shifted laterally towards the suction side, indicating at a significant deflection of the wake and trailing vortices.

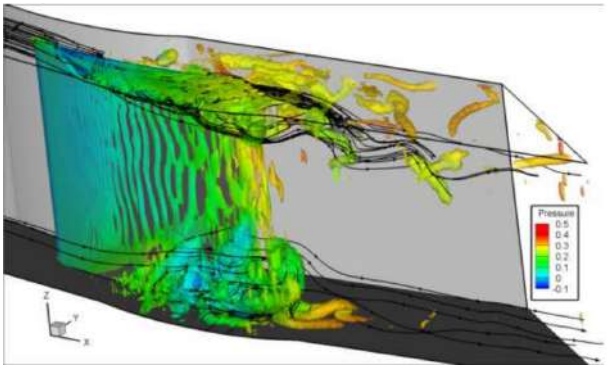

Figure 11: Instantaneous ER-HRL streamilnes over the blade tip and vortical structures on the blade, over the tip and the hub identified by pressure-coloured isosurfaces of $\Delta^2 p = 60$ in a linear compressor cascade with moving casing [16]

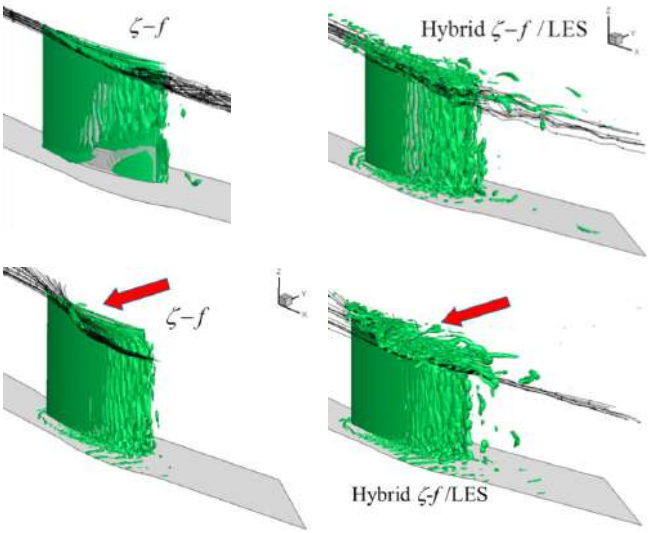

Figure 12: Vortical structures in and behind the tip leakage, identified by $Q = 35$ isosurfaces for $\zeta - f$ URANS and ER-HRL. Top: stationary casing; bottom: moving casing [16]

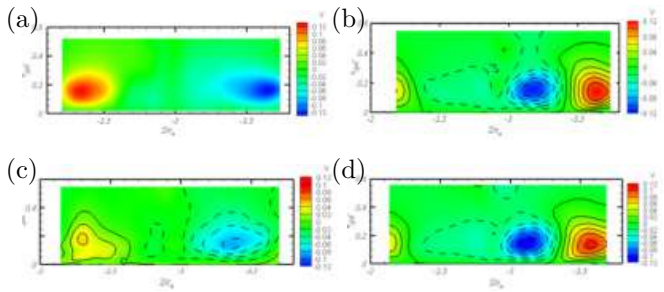

Figure 13: Wall-normal velocity in the tip-vortex wake at $x/ca = 1.37$. (a): Experiments from [22]; (b): $\zeta - f$ RANS; (c): Linear ER-HRL; (d): Nonlinear ER-HRL [16]

4 Comments and Conclusions

Predicting turbulent flows, heat and mass transfer and other surface phenomena in passages of industrial relevance pose specific challenges to scale-resolving CFD simulations. Multiple bounding walls of complex geometry exert strong inviscid (blocking) effects that may permeate over large flow regions. In hybrid RANS-LES approaches a substantial flow portion is entrusted to RANS, intentionally (for the sake of economy) or unintentionally (automatic gridding, difficulties in controlling the grid), so that the URANS region may encompass local separation, multiple vortex interactions, secondary flows, strong anisotropy, local transition, laminarization and others. All these and other phenomena require a RANS model free from topological parameters and yet be capable of capturing the basic physics of usually fully three-dimensional and intrinsically unsteady wall-adjacent flows, and ensuring sufficient receptivity to the LES forcing at its interface with RANS.

A RANS-LES method based on the elliptic-relaxation RANS wall-integration (WIN) eddy-viscosity $\zeta - f$ model blended with dynamic Smagorinsky LES (hence labelled ER-HRL) proved in a number of examples to capture most features listed above and capable of predicting such flows and phenomena in realistic industrial configurations. The enhanced sensitivity of the RANS model to LES perturbations and a specific way of RANS-LES blending (assisted also by backscatter of the dynamic LES sgs) ensure fast transitions across the RANS-LES interface without a notable log-layer mismatch ("grey area") anomaly.

As argued in [6], reduced empirical contents and better physical transparency are the desirable model prerequisites, at least when treating internal flows of complex topology. Robustness and economy matter, but should not be decisive since, for credible prediction of unknown situations, physics matters more. Advanced and physically sounder models are inevitably numerically more challenging, require more computational time and effort, but often only by a margin. As noted by [23], "The more capable the RANS component is, the lower costs of the hybrid computations will be. Therefore, the switch to LES in some regions does not remove the incentive to further the RANS technology".

Appendix 1: The ER-HRL model

$$\frac{Dk}{Dt} = D_k + P_k - \alpha\varepsilon, \;\; \frac{D\varepsilon}{Dt} = D_\varepsilon + \frac{C_{\varepsilon 1}P_k - C_{\varepsilon 2}\varepsilon}{\tau},$$

$$\frac{D\zeta}{Dt} = D_\zeta + f - \frac{\zeta}{k}P_k, \;\; D_\phi = \frac{\partial}{\partial x_j}\left[(\nu + \frac{\nu_t}{\sigma_\phi})\,\frac{\partial \phi}{\partial x_j}\right],$$

$$Ł^2\nabla^2 f - f = \frac{1}{\tau}\left(c_1 + C_2'\frac{P_k}{\varepsilon}\right)\left(\zeta - \frac{2}{3}\right),$$

$$\alpha = max(1, \frac{L_{RANS}}{\Delta}), \quad \Delta = C_\Delta(\Delta V)^{1/3},$$

$$L_{RANS} = \frac{k^{1.5}}{\varepsilon},$$

$$\nu_t^{RANS} = C_\mu^v\,\zeta\,k\,\tau, \quad \nu_t^{LES} = (C_s\Delta)^2\,|\overline{S}|,$$

$$\nu_t = max\left(\nu_t^{RANS}, \nu_t^{LES}\right),$$

$$\tau = max\left[min\left(\frac{k}{\varepsilon}, \frac{0.6}{\sqrt{6}C_\mu^v|S|\zeta}\right), C_T\left(\frac{\nu}{\varepsilon}\right)^{1/2}\right],$$

$$L = C_L\,max\left[min\left(\frac{k^{3/2}}{\varepsilon}, \frac{k^{1/2}}{\sqrt{6}C_\mu^v|S|\zeta}\right), C_\eta\left(\frac{\nu^3}{\varepsilon}\right)^{1/4}\right]$$

The table below summarises the empirical coefficients, most originating from the standard $k-\varepsilon$ and Durbin [6] $v^2 - f$ model:

C_μ^v	$C_{\varepsilon 2}$	C_1	C_2	σ_k	σ_ε	σ_ζ	C_T	C_L
0.22	1.9	0.4	0.65	1	1.3	1.2	6	0.36

$C_{\varepsilon 1}'$	C_η
$1.4(1 + 0.012/\zeta$	85

Appendix 2: Wall functions (SAWF) and their blending with Wall Integration (WIN) [4]

The below outlined Simplified Analytical Wall Function (SAWF) for velocity and temperature, as well as their blending with the wall-integration (WIN) $\zeta - f$ model in the hybrid RANS-LES strategy, makes it possible to use the ER-HRL irrespective of the location of the wall-nearest grid point P [4].

$$U^+ = \frac{1}{\kappa\psi}ln(Ey^+), \;\; \psi = 1 - \frac{C_U^+ y^+}{U^+\kappa},$$

$$C_U^+ = \frac{\nu}{\rho u_\tau^3}\left[\rho\frac{\partial U}{\partial t} + \rho U\frac{\partial U}{\partial x} + \rho V\frac{\partial U}{\partial y} + \frac{\partial P}{\partial x}\right],$$

$$\theta^+ = \frac{1}{\kappa_\theta\psi_\theta}ln(E_\theta y^+), \;\; \psi_\theta = 1 - \frac{\sigma_\theta C_\theta^+ y^+}{\theta^+\kappa_\theta},$$

$$C_\theta^+ = \frac{\mu}{\rho u_\tau q_w}\left[\rho\frac{\partial \theta}{\partial t} + \rho U\frac{\partial \theta}{\partial x} + \rho V\frac{\partial \theta}{\partial y} + S_\theta\right],$$

$$\phi_P = \phi_\nu e^{-\Gamma} + \phi_t e^{-1/\Gamma}, \;\; \Gamma = \frac{0.01y^{+4}}{1 + 5y^+}$$

where subscripts ν and t denote respectively the viscous (wall-limiting) and fully turbulent value of the variable $\phi(U, T)$.

Acknowledgement

The authors acknowledge the interaction with and earlier contribution to the development and testing of the EF-HRL approach by our colleagues Domenico Borello, Giovanni Delibra and Franco Rispoli at Sapienza University of Rome, Italy.

References

[1] M. Hadžiabdić, *LES, RANS and Combined Simulation of Impinging Flows and Heat Transfer*. PhD thesis, Delft University of Technology, Delft, The Netherlands, 2006.

[2] K. Hanjalić, "Will RANS survive LES: a view of perspectives," *ASME J. Fluids Engineering*, vol. 127, pp. 831–839, 2005.

[3] K. Hanjalić, M. Popovac, and M. Hadžiabdić, "A robust near-wall elliptic relaxation eddy-viscosity turbulence model for CFD," *International Journal of Heat and Fluid Flow*, vol. 25, pp. 1047–1051, 2004.

[4] M. Popovac and K. Hanjalić, "Compound wall treatment for rans computation of complex turbulent flows and heat transfer," *Flow Turbulence Combustion*, vol. 78, pp. 177–202, 2007.

[5] P. R. Spalart, W. H. Jou, M. Strelets, and S. R. Allmaras, "Comments on the feasibility of LES for wings, and on a hybrid RANS/LES approach," in *Advances in LES/DNS, Proc. of the first AFOSR int. conf. on DNS/LES* (C. Liu and Z. Liu, eds.), (Rouston Lousiana, U.S.A.), Greyden Press, Columbus, 1997.

[6] K. Hanjalić, D. Borello, G. Delibra, and F. Rispoli, "Hybrid LES/RANS of internal flows:a case for more advanced rans," in *Progress in Hybrid RANS-LES Modelling, Notes on Numerical Fluid Mechanics and Multidisciplinary Design* (S. G. et al., ed.), pp. 130:19–35, Springer Int. Publ. Switzerland, 2015.

[7] P. Durbin, "Near-wall turbulence closure modelling without 'damping functions'," *Theoret. Comput. Fluid Dynamics*, vol. 3, pp. 1–13, 1991.

[8] G. Delibra, K.Hanjalić, D. Borello, and F. Rispoli, "Vortex structures and heat transfer in a wall-bounded pin matrix: LES with a RANS wall treatment," *Int. J. Heat Fluid Flow*, vol. 31(5), pp. 740–753, 2010.

[9] P. R. Spalart, "Detached-eddy simulation," *Annu. Rev. Fluid Mech.*, vol. 41, p. 181-202, 2009.

[10] U. Piomelli, E. Balaras, H. Pasinato, K. Squires, and P. Spalart, "The inner-outer layer interface in large-eddy simulations with wall-layer models," *Int. J. Heat and Fluid Flow*, vol. 24, pp. 538–550, 2003.

[11] S. Arvidson, L. Davidson, and P. S.-H., "Interface methods for grey-area mitigation in turbulence-resolving hybrid RANS-LES," *Int. Journal of Heat and Fluid Flow*, vol. 73, p. 236-257, 2018.

[12] L. Temmerman, M. Hadžiabdić, M. Leschziner, and K. Hanjalić, "A hybrid two-layer URANS-LES approach for Large Eddy Simulation at high Reynolds numbers," *International Journal of Heat and Fluid Flow*, vol. 26, pp. 173–190, 2005.

[13] K. Hanjalić, M. Hadžiabdić, L. Temmerman, and M. Leschziner, "Merging LES and RANS strategies: Zonal or Seamless coupling?," in *Direct and Large-Eddy Simulations V* (R. Friedrich, B. Geurts, and O. Métais, eds.), pp. 451–464, Kluwer, 2004.

[14] L. Temmerman, M. Leschziner, and K. Hanjalić, "A-priori studies of a near-wall RANS model within a hybrid LES/RANS scheme," pp. 317–326, 5^{th} Int. Conf. on Engineering Turbulence Modelling and Experiments, Mallorca, Spain, 2002.

[15] G. Delibra, URANS, LES and Hybrid RANS/LES of flow and heat transfer in configurations relavant to thermal turbomachinery. PhD thesis, Sapienza University of Rome, Italy, 2011.

[16] B. Domenico, G. Delibra, K. Hanjalić, and F. Rispoli, "Hybrid LES/RANS study of turbulent flow in a linear compressor cascade with moving casing," vol. 7 of *Turbo Expo: Power for Land, Sea, and Air*, pp. 2735–2744, 2010.

[17] D. Borello, G. Delibra, K. Hanjalić, and F. Rispoli, "LES and hybrid LES/RANS study of flow and heat transfer around a wall-bounded short cylinder," in *Progress in Turbulence III* (J. Peinke, M. Oberlack, and A. Talamelli, eds.), (Berlin, Heidelberg), pp. 147–150, Springer Berlin Heidelberg, 2010.

[18] G. Delibra, D. Borello, K. Hanjalic, and F. Rispoli, "An LES Insight Into Convective Mechanism of Heat Transfer in a Wall-Bounded Pin Matrix," vol. 2010 14th International Heat Transfer Conference, Volume 2 of *International Heat Transfer Conference*, pp. 807–815, 2010.

[19] G. Delibra, D. Borello, K. Hanjalic, and F. Rispoli, "URANS of flow and endwall heat transfer in a pinned passage relevant to gas-turbine blade cooling," *International Journal of Heat and Fluid Flow*, vol. 30, no. 3, pp. 549 – 560, 2009.

[20] F. E. Ames, C. A. Nordquist, and L. A. Klennert, "Endwall Heat Transfer Measurements in a Staggered Pin Fin Array With an Adiabatic Pin," vol. Volume 4: Turbo Expo 2007, Parts A and B of *Turbo Expo: Power for Land, Sea, and Air*, pp. 423–432, 2007.

[21] Y. Wang and W. J. Devenport, "Wake of a compressor cascade with tip gap, part 2: Effects of endwall motion," *AIAA Journal*, vol. 42, no. 11, pp. 2332–2340, 2004.

[22] C. Muthanna and W. J. Devenport, "Wake of a compressor cascade with tip gap, part 1: Mean flow and turbulence structure," *AIAA Journal*, vol. 42, no. 11, pp. 2320–2331, 2004.

[23] P. R. Spalart, "Strategies for turbulence modelling and simulations," *International Journal of Heat and Fluid Flow*, vol. 21, no. 3, pp. 252 – 263, 2000.

Partially Averaged Navier-Stokes (PANS) Scale Resolving Simulations: From Fundamentals to Engineering Applications

B. Basara[1] and S. S. Girimaji[2]

[1] *AVL List GmbH, Advanced Simulation Technologies, Graz, Austria*
[2] *Ocean and Aerospace Engineering Departments Texas A&M University, College Station, Texas 77843, USA*

Abstract

The objective of this article is to briefly review the progress in Partially Averaged Navier-Stokes (PANS) method over the last fifteen years. We first present the foundational concepts of the PANS approach and proceed to exhibit some of the key simulation results in important engineering flows. PANS provides a mathematical framework and the physical principles for transferring the closure modelling knowledge from any Reynolds-Averaged Navier-Stokes (RANS) turbulence model to scale-resolving subgrid closure. The degree of implicit filtering is imposed by means of physical resolution control parameters, which in turn determine the closure coefficients. Theoretically sound and computationally robust method for computing the resolution control parameter is presented. The importance of near-wall models is also discussed, and possible avenues for future improvements are proposed. Finally, some key practical PANS simulations are highlighted.

1 Introduction

Scale resolving simulation (SRS) are envisioned for providing an optimal balance between accuracy and computational costs. Such methods are very attractive for industrial applications, especially for complex flow geometries wherein Large Eddy Simulations (LES) are prohibitively expensive and Reynolds-Averaged Navier-Stokes (RANS) approaches lack the fidelity to capture the underlying flow physics. The scale-resolving simulations can be broadly classified as zonal and bridging approaches. Zonal methods divide the computational domain into two distinct regions. Typically, a RANS turbulence model is employed in the near-wall region and LES in used in the remainder of the flow domain. On the other hand, bridging models employ the same closure model form in the entire domain, but the closure coefficients are functions of implicit filterwidth. Each approach has important challenges that must be addressed. In the zonal methods, the interface between RANS and LES must be handled in a manner that preserves important flow physics. In the bridging methods, the closure model must be suitably sensitive to the flow physics as a function of the implied filter width. A number of different simulation strategies are currently available under each SRS approach. For industrial applications, it is important to assess the suitability of SRS methods on the basis of: (1) physical foundation and the generality of the closure modelling approach; (2) specification of resolution control parameter for optimal use of the grid; (3) numerical characteristics and computational robustness including - convergence properties, error estimation etc. The purpose of this review is to address the above features in the context of the Partially-Averaged Navier-Stokes (PANS) method.

The PANS approach (Girimaji et al. 2003; Girimaji, 2006) seeks to convey the physical insight and closure physics from RANS models to SRS closures. Using fixed point analysis, the SRS closures are derived from parent RANS models using the averaging-invariance principle (Germano, 1992). In the resulting SRS model equations, the closure coefficients are rendered functions of grid resolution parameters in a manner dictated by turbulence flow physics. At one limit of resolution, the PANS calculation approaches DNS (direct numerical simulation). At the other limit, the PANS model reverts to the RANS model. In the original works, the RANS $k-\epsilon$ model served as the parent model. The corresponding resolution parameters are the unresolved-to-total ratio of turbulent kinetic energy f_k and unresolved-to-total ratio of dissipation f_ϵ. These parameters enter the model equations via a sink term in dissipation rate equation - in destruction of dissipation. In addition, the diffusion term in the turbulent kinetic energy and dissipation equation are also functions of the resolution parameters (Tazraei and Girimaji, 2019). Lakshmipathy and Girimaji (2006) derived the PANS $k-\omega$ variant. They also demonstrated that, as in RANS, $k-\epsilon$ and $k-\omega$ models exhibited advantages in different types of flows. While PANS was shown to be successful in free-shear flows and simple wall-bounded flows, further improvement was needed for smooth-surface separation. To address this need, Basara et al. (2011) derived the four-equation $k-\epsilon-\zeta-f$ PANS model. This model was implemented in conjunction with a hybrid wall treatment to incorporate the low Reynolds number effects. Other developments to address low-Reynolds number effects include the work of Ma et al. (2011) who proposed integration of modelled equations all the way down to the wall. More recently, Kamble et al. (2019) proposed a two-layer PANS model where the PANS $k-\epsilon$ model is used in the outer layer and only the unresolved kinetic energy is solved in the inner layer. In the inner layer, the eddy viscosity and dissipation are determined based on known scaling relationships.

It must be noted that the scale-dependent destruction closure model of PANS is very similar to that of PITM (Partially-Integrated Turbulence Transport Model) of Chaouat and Schiestel, (2005). Chaouat (2017) presents a comprehensive discussion of the various variants of PITM. One significant difference between PITM and PANS lies in the modelling of the turbulent transport terms of unresolved turbulent kinetic energy and dissipation (Tazraei and Girimaji, 2019).

Much of the PANS proof-of-concept studies employed spatially uniform resolution control parameters. This permits the validation of the modelling approach using

the paradigm that SRS is the DNS of a variable viscosity non-Newtonian turbulence field (Reyes et al. 2014). For industrial applications, accuracy of the PANS simulation and efficient use of the numerical grid depend upon the appropriate specification of the resolution control parameters - f_k and f_ϵ for the PANS $k-\epsilon$ model or f_k and f_ω for the PANS $k-\omega$ model. For such industrial applications, Girimaji and Abdol-Hamid (2005) formulated an expression for the smallest resolution achieved for a given grid, which is implemented by Basara et al. (2008) in a dynamic procedure where f_k is calculated at every calculation cell and for every time step. In that context, due attention should be given to a commutation error as suggested by Girimaji and Wallin (2013). In recent times, other methods for determining the optimal f_k for a given flow on a specific grid have also been proposed. In the following sections some of these methods are discussed in detail.

2 Mathematical model

Consider the decomposition of a turbulent velocity Ui into two components, the partially filtered component and the sub-filter component as

$$V_i = U_i + u_i \tag{1}$$
$$p = P + p'$$

If the filter commutes with spatio-temporal differential operator, then the Partially-Averaged Navier-Stokes equations can be written as

$$\frac{\partial U_i}{\partial t} + U_j \frac{\partial U_i}{\partial x_j} + \frac{\partial \tau(V_i,V_j)}{\partial x_i} = -\frac{1}{\rho}\frac{\partial P}{\partial x_i} + \nu \frac{\partial^2 U_i}{\partial x_j \partial x_j} \tag{2}$$

where $\tau(V_i,V_j)$ is the generalized second moment which represents the effect of the unresolved motion on the resolved field (Germano, 1992). The closure for this subfilter stress can be obtained by using Boussinesq approximation as proposed by Girimaji (2006):

$$\tau(V_i,V_j) = -\nu_u \left(\frac{\partial U_i}{\partial x_j} + \frac{\partial U_j}{\partial x_i} \right) + \frac{2}{3} k_u \delta_{ij} \tag{3}$$

where the eddy viscosity of the unresolved scales is given as

$$\nu_u = c_\mu \frac{k_u^2}{\epsilon_u} \tag{4}$$

The original approach of (Girimaji et al., 2003), Girimaji, 2006) was based on the $k-\epsilon$ RANS model. Two equations, namely the unresolved kinetic energy and the unresolved dissipation equations are solved to obtain the velocity and length scales of the unresolved flow field:

$$\frac{Dk_u}{Dt} = P_u - \epsilon_u + \frac{\partial}{\partial x_j}\left[\left(\nu + \frac{\nu_u}{\sigma_{ku}} \right) \frac{\partial k_u}{\partial x_j} \right] \tag{5}$$

$$\frac{D\epsilon_u}{Dt} = C_{\epsilon 1} P_u \frac{\epsilon_u}{k_u} - C^\star_{\epsilon 2} \frac{\epsilon_u^2}{k_u} + \frac{\partial}{\partial x_j}\left[\left(\nu + \frac{\nu_u}{\sigma_{\epsilon u}} \right) \frac{\partial \epsilon_u}{\partial x_j} \right] \tag{6}$$

with the closure constants

$$C^\star_{\epsilon 2} = C_{\epsilon 1} + \frac{f_k}{f_\epsilon}(C_{\epsilon 2} - C_{\epsilon 1}); \quad \sigma_{ku,\epsilon u} = \sigma_{k,\epsilon} \frac{f_k^2}{f_\epsilon} \tag{7}$$

Lakshmipathy and Girimaji (2006) derived the PANS $k-\omega$ variant in which the unresolved turbulence frequency equation is given by

$$\frac{D\omega_u}{Dt} = \alpha P_u \frac{\omega_u}{k_u} - \beta' \omega_u^2 + \frac{\partial}{\partial x_j}\left[\left(\nu + \frac{\nu_u}{\sigma_{\omega u}} \right) \frac{\partial \omega_u}{\partial x_j} \right] \tag{8}$$

where

$$\beta' = \alpha\beta^\star - \frac{\alpha\beta^\star}{f_\omega} + \frac{\beta}{f_\omega} \tag{9}$$

The closure coefficients are given as

$$\beta^\star = 0.09; \alpha = 5/9; \beta = 0.075; \sigma_k = \sigma_\omega = 2 \tag{10}$$

High-fidelity near-wall modelling is important for many industrial applications, so Basara et al. (2011) derived the near wall $k-\epsilon-\zeta-f$ PANS variant, which not only solves equations for k_u and ϵ_u but also an extra equation for the un resolved velocity scale ratio given as

$$\frac{D\zeta_u}{Dt} = f_u - \frac{\zeta_u}{k_u} P_u + \frac{\zeta_u}{k_u}\epsilon_u(1-f_k) + \frac{\partial}{\partial x_j}\left[\left(\nu + \frac{\nu_u}{\sigma_{\zeta u}} \right) \frac{\partial \zeta_u}{\partial x_j} \right] \tag{11}$$

where the elliptic function f_u is given as

$$L_u^2 \nabla^2 f_u - f_u = \frac{1}{T_u}\left(c_i + C_2' \frac{P}{\epsilon} \right)\left(\zeta_u - \frac{2}{3} \right) \tag{12}$$

Note that $f_\zeta = f_v^2/f_k$ is not used in the formulation. Instead, the information is contained in the elliptic function f_u as shown in the original reference [6].

Currently, the most popular manner of determining the unresolved-to-total kinetic energy ratio f_k as a function of grid spacing is to use the relation (Girimaji and Hamid 2005; Basara et al. 2008):

$$f_k = \frac{1}{\sqrt{c_\mu}}\left(\frac{\Delta}{\Lambda} \right)^{2/3} \tag{13}$$

where Δ is the grid cells dimension ($\Delta = V^{1/3}$ where V is the cell volume) and Λ is the integral scale of turbulence $\Lambda = k^{3/2}/\epsilon$). In high Reynolds number flows, $f\epsilon$ is taken to be equal one, which means $\epsilon_u = \epsilon$. A dynamic parameter f_k changes at each point at the end of every time step, and then it is used as a fixed value at the same location during the next time step. This modelling approach is further enhanced by including the hybrid wall treatment. This entails combining integration up to the wall with wall functions, as shown in Popovac & Hanjalic (2005), Basara (2006)

Another option was recently proposed by Kamble et al. (2019) who solved the standard PANS $k-\epsilon$ model given by Eqs. (5) and (6) in the outer wall layer and in the inner layer, the unresolved dissipation ϵ_u is calculated explicitly as

$$\epsilon_u = \frac{k_u^{3/2}}{l_{\epsilon u}}; \quad \nu_u = C_{\mu u}\sqrt{k_u} l_{\mu u} \tag{14}$$

where $C_{\mu_u} = C_\mu$, see Girimji et al. (2006), and following Kamble et al. (2019), the unresolved length scales of dissipation and eddy viscosity can be specified as:

$$l_{\epsilon u} = f_k^{3/2} C_l y[1 - e^{-R_{yu}/A_\epsilon}] \tag{15}$$

$$l_{\mu u} = f_k^{3/2} C_l y[1 - e^{-R_{yu}/A_\mu}]; R_{\mu u} = \frac{\sqrt{k_u} y}{\sqrt{f_k}\nu}$$

An advantage of the PANS method is that any RANS model can be adapted for the scale-resolving simulations as shown above. It must be kept in mind that the coarse

mesh and corresponding resolution-control parameters will lead to the RANS solution.

For computing industrial flows, SRS methods aim to obtain appreciably improved results over RANS method for a computational cost that is significantly lower that that of LES calculations. This involves choosing $f_k = k_u/k$ that is optimal for the flow phyiscs and grid size. However, f_k given by Eq. (13) must not be smaller than (and not as) $f_k = k_u/k$ which would mean that the mesh doesn't support chosen cut-off parameter. There are other formulations of f_k other than Eq. (12), e.g. Foroutan and Yavazkurt (2014) etc. Nearly all of the proposals in literature use the integral length scale $\Lambda = k^{3/2}/\epsilon$. Therefore, it is necessary to calculate a total turbulent kinetic energy k. The current procedure computes the total kinetic energy from the equation

$$k = k_r + k_u \tag{16}$$

where the resolved energy k_r is given by

$$k_r = \frac{1}{2}(U_i - \overline{U_i})^2 \tag{17}$$

The computation of the resolved kinetic energy can involve expensive averaging process. Further, periodic variations in the flow field could significantly contribute to the local value of k_r in certain cases and cause too low f_k.

An alternate approach would solve a model transport equa- tion for the resolved kinetic energy along with the other PANS equations as proposed by Basara, Pavlovic and Girimaji (2018):

$$k = k_{ssv} + k_u \tag{18}$$

Here, the resolved kinetic energy, k_{ssv}, is called the scale supplying variable. Thus, computing the resolved kinetic energy leads to computation of the total kinetic energy, see Eq. (18), which is then used to compute the resolution parameter f_k with Eq. (13). This PANS-SSV variant is based on the PANS $k-\epsilon-\zeta-f$ model and includes one additional equation:

$$\frac{\partial k_{ssv}}{\partial t} + U_j \frac{\partial k_{ssv}}{\partial x_j} = (1-f_k)(P-\epsilon) \tag{19}$$

$$+\frac{\partial}{\partial x_j}\left[\left(\nu + \frac{\nu_u}{\sigma_{ku}}\right)\frac{\partial k_{ssv}}{\partial x_j}\right]$$

Note that the resolution parameter f_k calculated by Eq. (13) is used in Eq. (19). The derivation of this equation is based on the same principals as the development of the unresolved kinetic energy Eq. (5) (for full derivations see Basara et al. 2018). This means that both, unresolved and resolved kinetic energy components are continuously calcu lated which enables in-situ update of the resolution parameter f_k. Thus, f_k is dynamically specified in time and space depending on the flow and computational meshes. This new variant enables efficient PANS computations of applications with moving geometries, transient boundaries and inherent unsteadiness e.g., periodic fuel injection. The proposed approach could also be applied for other bridging SRS methods.

3 Results and discussion

The performance of PANS has been well exhibited in a variety of idealized and canonical flows. Using isotropic turbulence data at different degrees of resolution, Reyes et al. (2014) clearly exhibit that the PANS fluctuating fields scale according to Kolmogorov hypotheses. Tazraei and Girimaji (2019) demonstrate that the PANS fluctuating field captures the hairpin vortices and ejection/sweep mechanisms quite precisely in channel flows. PANS has also been shown to perform well in a variety of wake flows including flows past circular cylinder, square cylinder and backward-facing step. We now exhibit the performance of PANS in a variety of real-life industrial application. Tested industrial cases include aerodynamics car models (Jakirlic et al. 2014), examples of active flow control (Han et al. 2013, Minelli et al. 2017), landing gears (Krajnovic et al. 2012), overtaking car maneuver (Jakirlic et al. 2018) etc. In all these studies, it was shown that the PANS simulations provide results that are more accurate than those of RANS and comparable to that of LES on much coarser meshes. We present a few selected cases here to provide a quick demonstration of the capabilities of PANS (all calculations presented in the subsections below have been performed using the commercial software AVL FIRE^{TM}).

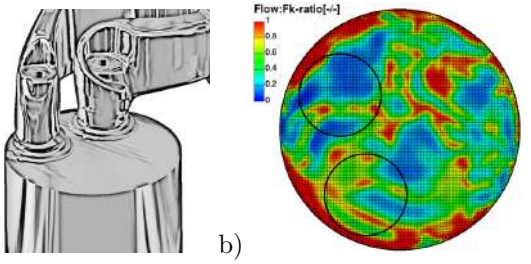

a) b)

Figure 1: (a) Model geometry of the helical-tangential intake port and (b) predicted resolution parameter f_k at the cross section 30 mm below the firedeck (Basara, Poredos and Gorensek, 2016)

3.1 Intake ports of IC engines

A computational study of the flow in intake port geometries was shown by Basara et al. (2016) in all detail. Three different intake port geometries, namely two combined tangential and helical ports and one quiescent port were analysed. Each of these cases was calculated for different valve lifts and the results were compared with available measurements. A typical combined helical-tangential intake port configuration is shown in Figure 1a. In the reported study, different computational meshes with maximum cells about 5 million were used. Due attention was given to the wall mesh layers to deliver the best input for the near wall model, which is in this case, the $k-\zeta-f$ with the hybrid wall treatment. Authors reported that the non-dimensional wall distance y^+ for these calculations varied between 2 and 16. As usually for such real-life cases, one could expect that the resolution parameter f_k is equal or close to unity near the wall, which means that the full RANS $k-\zeta-f$ model is used there. Predicted distribution of f_k is shown at measured cross section of the intake port in Figure 1b. Note that f_k in this case was calculated by using Eqs. (13) and (16-17).

The following integral parameters were compared: (a) a discharge coefficient and (b) a swirl coefficient. A discharge coefficient is usually easier to predict accurately than the swirl coefficient. Even there, visible improvements for the higher valve lifts with the PANS $k-\zeta-f$ was obtained, see Figure 2. The RANS $k-\zeta-f$ model is an isotropic eddy viscosity model and therefore not suitable for calculating swirling flows and if the mesh

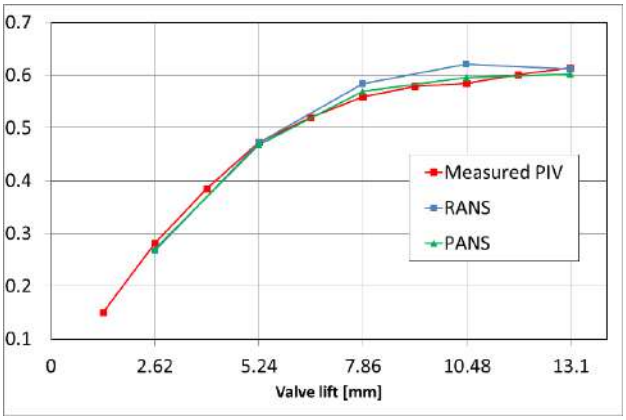

Figure 2: Discharge coefficients as predicted by the RANS and PANS $k-\zeta-f$ on the hexahedral mesh and compared with PIV measurements (Basara et al. 2016)

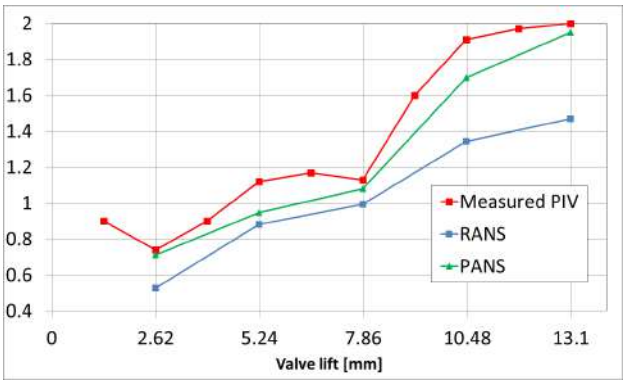

Figure 3: Swirl coefficients as predicted by the RANS and PANS $k-\zeta-f$ on the hybrid mesh and compared with PIV measurements (Basara, Poredos and Gorensek, 2016)

is coarse in the cylinder, a solution will go in direction of RANS results and one could expect difficulties in performing accurate simulations. However, having even relatively fine meshes which support mesh independent RANS results, would resolve a part of turbulent kinetic energy in PANS calculations and consequently, results will be improved. The lower resolution parameter f_k than unity means that an isotropic modelling is done only for the unresolved part of turbulence and therefore, the modelling error affects less the overall solution.

Figure 3 shows swirl coefficients for different valve lifts as predicted by the RANS and PANS $k-\zeta-f$ models and compared with PIV measurements. A trend of the swirl coefficient and absolute values are much better predicted with the PANS model. Very good agreements are also present in predicted velocity fields, see Figure 4. This was achieved on all cases presented by Basara et al. (2016). It was clearly shown that with the help of the computational mesh and the resolution parameters incorporated in the $k-\zeta-f$ model, the results are significantly improved.

3.2 External Car Aerodynamics

The most of PANS calculations, reported up to now, have been performed in the field of aerodynamics. Usually results obtained by the PANS models have been compared with the RANS models or in some cases with the LES to investigate if the PANS could provide the optimum fidelity on the given computational mesh. Some of typ-

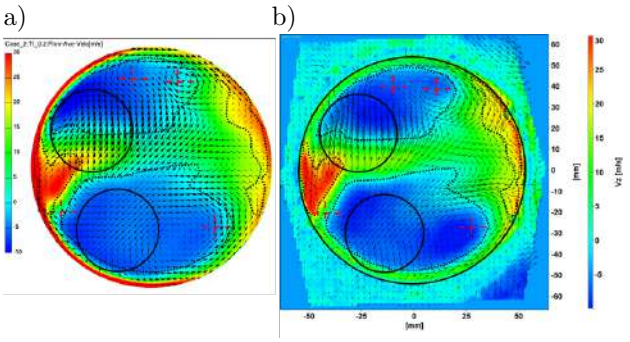

Figure 4: Predicted velocity magnitude at the cross section 30 mm below the firedeck and for the valve lift of 5.23 mm: (a) PANS $k-\zeta-f$; and (b) PIV measurements (Basara, Poredos and Gorensek, 2016)

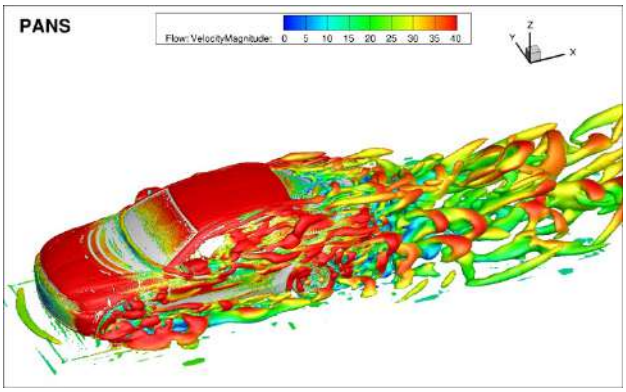

Figure 5: Flow field predicted by PANS model visualized by Q-criterion (Jakirlic, Kutej, Basara and Tropea, 2014)

ical PANS results are presented for a BMW car model by Jakirlic et al. (2014). Calculations were performed by using RANS, URANS and PANS $k-\zeta-f$ models. Predicted flow field by the PANS model is shown in Figure 5. The pressure coefficient at different surfaces of a car model as obtained by the PANS model is shown in Figures 6-7. A very good agreement with the measurements was achieved though only 28 million cells mesh was used.

Jakirlic et al. (2014) showed an important difference between results obtained by different modelling approaches on the same mesh.

The PANS method also predicted drag and lift coefficients close to the measured values, see original reference [20]. It is important to note that calculations with the PANS models are very stable even with a dynamic calculation procedure for the resolution parameter f_k . Viher et al. (2018) and Viher (2019) predicted the real Volvo SUV with the complete underhood, see Figure 8a-b. Viher et al. (2018) made calculations on meshes containing 130 mil. cells with 4 wall cell layers achieving approximatively y^+ around 15. Lift predictions were much improved with the PANS model, namely 0.052, compared to the RANS predictions of 0.003 and measured value of 0.085. If the surface of the car is accurate and no approximations are made, then further mesh refinements would lead to further result improvements. Computational meshes could be refined by using an adaptive refinement procedure as well. The next case, namely Volfo VRAK car model, is done by defining the box in which refinements is performed following the chosen f_k criterion. In this case, we used $f_k > 0.5$ to refine the mesh, see Figures 9-10. A drag coefficient on the basic mesh was 0.306

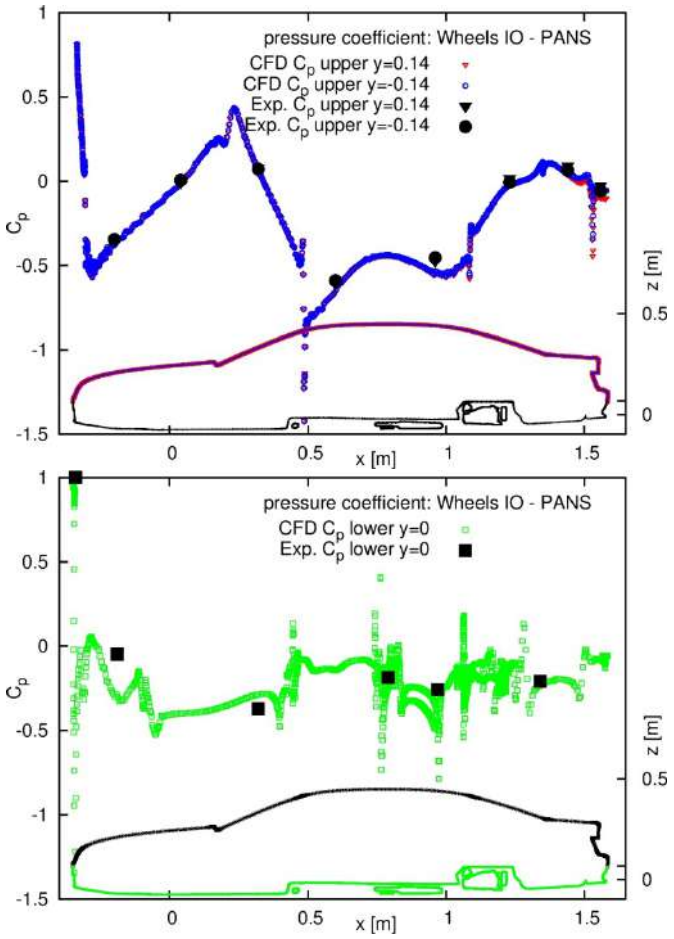

Figure 6: Predicted mean pressure coefficient over the upper surface (upper) and lower surface of a car model (lower) by the PANS model (Jakirlic, Kutej, Basara and Tropea, 2014)

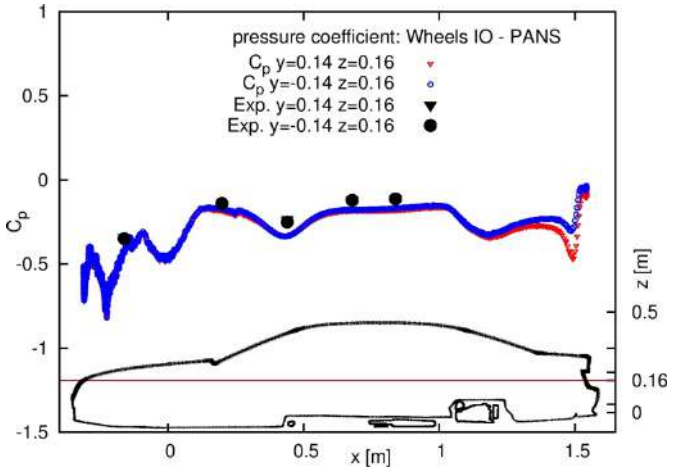

Figure 7: Predicted mean pressure coefficient at the side surface of a car model by the PANS model (Jakirlic, Kutej, Basara and Tropea, 2014)

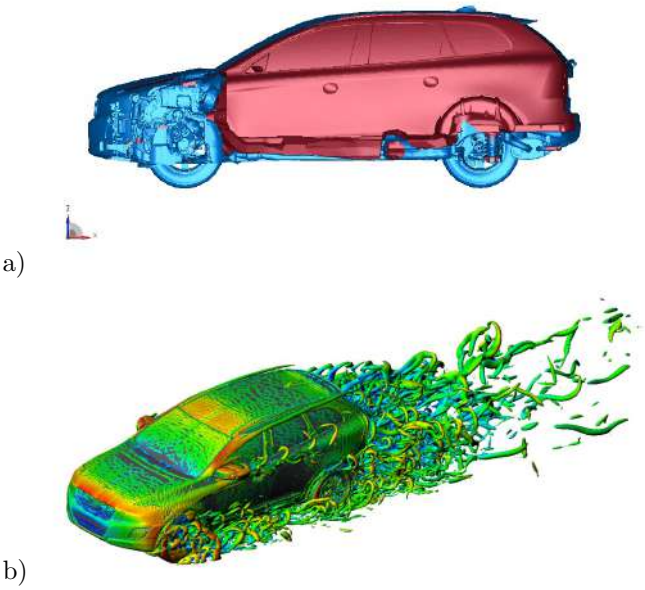

Figure 8: Volvo SUV: calculated geometry (a) and an instantaneous isosurface of the second invariant of the velocity gradient (b) (Viher, Tibaut, Basara and Krajnovic 2018; Viher, 2019)

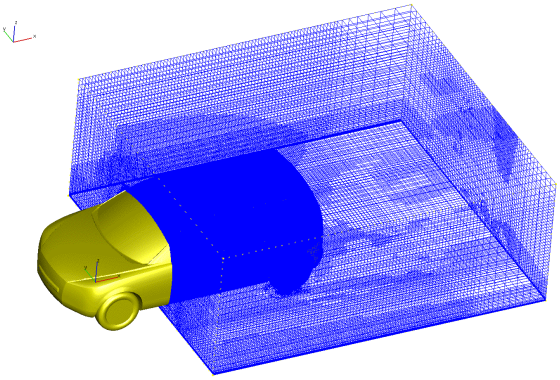

Figure 9: The box around the car model where the mesh refinement is applied and refined cells for the finest mesh containing 13.5 million cells (Basara, Krajnovic and Pavlovic, 2014)

and on the refined mesh 0.322 which is much closer to the measured value of 0.335. The predicted lift coefficent was 0.022 which is very close to the measured value of 0.026 (Basara et al. 2014). Due to the mesh refinement and abrupt changes in f_k, it is recommended to include a commutation error correction as suggested by Girimaji and Wallin (2013). Following their approach, the eddy viscosity should be corrected to consider a rapid change of f_k in time and space, see original reference [14].

3.3 Square cylinder

The vortex shedding around a square cylinder at $Re = 21400$ (ERCOFTAC classic database, Case C.43) is the case very often used to present a performance of various RANS turbulence models. There are different measurements of the same case as well as LES and hybrid RANS/LES calculations. Recently, Trias et al. (2015) published DNS results which provided additional insight in this flow. Even the first PANS publication, Girimaji

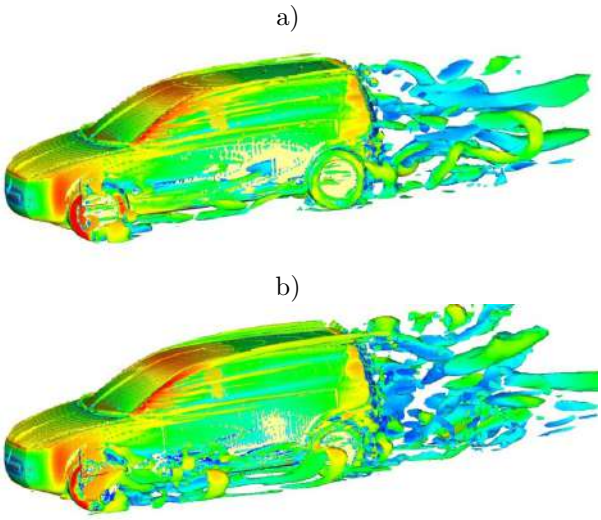

Figure 10: An instantaneous iso-surface of the second invariant of the velocity gradient colored by the resolution parameter f_k as predicted by PANS: a) coarse mesh (4.5 million), b) fine mesh (13.5 million) (Basara, Krajnovic and Pavlovic, 2014)

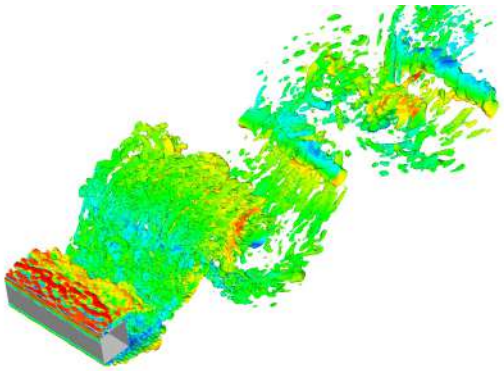

Figure 11: An instantaneous iso-surface of the second invariant of the velocity gradient as predicted by PANS (Basara, Pavlovic and Girimaji, 2018)

et al. (2003), was using this case to explain fundaments of the PANS approach (using constant f_k for clarity). Basara et al. (2018) computed again this case, see Figure 11, to show how periodic flows could influence dynamic calculations of f_k with Eqs. (13; 16-17) and provide wrong values of total k and consequently wrong f_k.

To solve this problem, Basara et al. (2018) introduced the scale supplying variable equation, Eq. (19), so total k could be obtained by using Eq. (18). The resolution parameter f_k as predicted by the PANS-SSV on one of meshes is shown in Figure 12a. All results for the square cylinder were improved, see original reference [19]. Figure 12b shows PANS predicted average flow streamlines describing the flow very close to DNS of Trias et al. (2015) (note that 5 mil. cells were used for PANS and 322 mil. cells for DNS).

With the new PANS-SSV variant, the Strouhal number was improved from 0.136 (PANS with Eqs.12; 16-17) to 0.13. Also, a drag coefficient was improved from 2.33 to 2.24 while the value of 2.1 was obtained by measurements. Present results confirm that the PANS-SSV could be a workable solution for the cases with moving geometries.

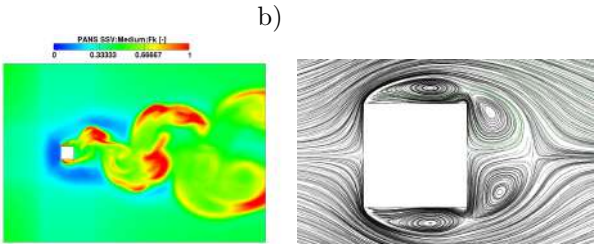

Figure 12: Predicted f_k by the PANS-SSV and using Eq. (18) (a) and streamlines of the averaged flow as predicted by the PANS model (b) (Basara, Pavlovic and Girimaji, 2018)

	PANS	PANS-SSV	DNS	Data
St	0.136	0.130	0.132	0.130-0.133

Table 1: Predicted and measured Strouhal number

3.4 Moving geometry - engine

Indeed, the PANS-SSV variant opens a prospect of more cost-effective engine calculations due to avoiding a cycle-to-cycle averaging of the resolved field to obtain total k needed for Eq. (13). Continuous calculations of both, un-resolved and resolved turbulent kinetic energy, enables in-situ update of the resolution parameter f_k. Basara et al. (2020) calculated AVL single cylinder research engine by using typical RANS meshes which vary between 1.4-4.5 mil. cells depending on the mesh position. Predicted vortex structure at certain angle is shown in Figure 13a and a cycle-to-cycle predicted pressure peak in Figure 13b.

Calculations were performed with the spray and combustion modules. Predicted temperature fields during the combustion phase by the RANS and the PANS $k-\zeta-f$ models are shown in Figures 14a-b for the chosen angle. The flame front predicted by the RANS is very smooth while PANS results show much more wrinkles due to capturing flow fluctuations. Emission calculations were also very different in cycles providing a completely different output of CFD calculations, see original reference [31]. Present results show that the PANS-SSV can be simple applied on the moving geometries.

4 Conclusions

This paper presents a brief review of the PANS method of scale resolving simulations of turbulence. It is exhibited that PANS is based on strong fundamental physical

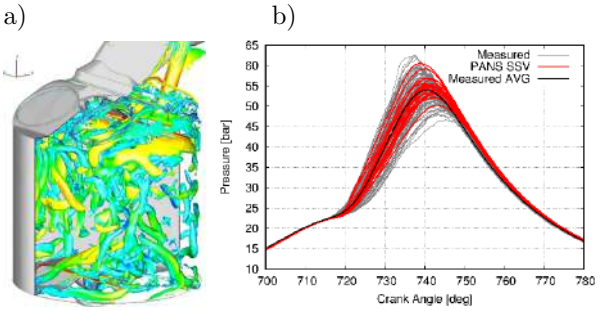

Figure 13: Computationally obtained vortex structures visualized by the Q-criterion (a) and predicted pressure peak values: cycle-to-cycle variations as predicted by the PANS model (b) (Basara, Pavlovic and Girimaji, 2020)

a) b)

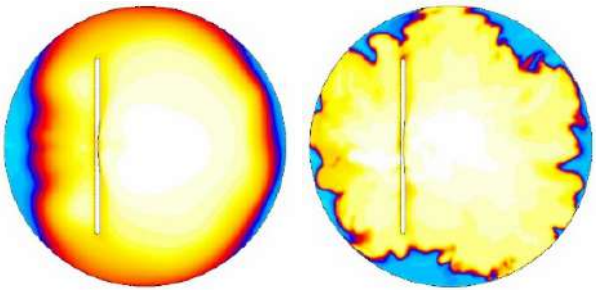

Figure 14: Predicted temperature by the RANS and PANS $k-\zeta-f$ model at 740 CA ((Basara, Pavlovic and Girimaji, 2020)

foundations and yet possess the robustness to simulate industrial flows accurately at reasonable computational cost. The PANS computations presented here are based on Boussinessq constitutive closure with two transport equations for unresolved kinetic energy and dissipation (or specific dissipation). PANS can also be used in conjunction with non-linear eddy viscosity models (Saroha et. al, 2019) and even extended to full stress transport equations. PANS concept has also been adapted for heat transfer computations (Basara 2014, Chakraborty et al. 2019). Most recently, machine-learning techniques have been used to provide accurate scale-dependent constitutive equations for PANS computations (Lav et al. 2019). Judicious use of scale resolution along with machine learning techniques for determining the scale-dependent constitutive equation will be an excellent direction for the future of PANS.

References

[1] Girimaji, S.S., Srinivasan, R. and Jeong, E. (2003). PANS turbulence model for seamless transition between RANS and LES: fixed-point analysis and preliminary results. In ASME/JSME 2003 4th Joint Fluids Summer Engineering Conference (pp. 1901-1909). American Society of Mechanical Engineers Digital Collection.

[2] Girimaji, S.S. (2006): Partially-averaged Navier-Stokes model for turbulence: A Reynolds-averaged Navier-Stokes to direct numerical simulation bridging method. Journal of Applied Mechanics, Vol. 73(3), pp. 413-421

[3] Germano, M. (1992): Turbulence: the filtering approach. Journal of Fluid Mechanics, Vol. 238, pp. 325-336

[4] Tazraei, P. and Girimaji, S.S. (2019): Scale-resolving simulations of turbulence: Equilibrium boundary layer analysis leading to near-wall closure modeling. Physical Review Fluids, Vol. 4(10), p.104607

[5] Lakshmipathy, S. and Girimaji, S. (2006): Partially-averaged Navier-Stokes method for turbulent flows: $k-\omega$ model implementation. In 44th AIAA aerospace sciences meeting and exhibit (p. 119)

[6] Basara, B., Krajnovic, S., Girimaji, S., and Pavlovic, Z. (2011): Near-wall formulation of the Partially Averaged Navier-Stokes turbulence model. AIAA journal, Vol. 49(12), pp. 2627-2636

[7] Ma, J.M., Peng, S.H., Davidson, L. and Wang, F.J. (2011): A low Reynolds number variant of partially-averaged Navier-Stokes model for turbulence. Int. J. Heat and Fluid Flow, Vol. 32(3), pp. 652-669

[8] Kamble, C., Girimaji, S.S., and Chen, H.C. (2019): Partially Averaged Navier-Stokes Formulation of a Two-Layer Turbulence Model. AIAA Journal, pp. 1-10

[9] Chaouat, B. and Schiestel, R. (2005): A new partially integrated transport model for subgrid-scale stresses and dissipation rate for turbulent developing flows. Physics of Fluids, Vol. 17(6), p.065106

[10] Chaouat, B. (2017): The state of the art of hybrid RANS/LES modeling for the simulation of turbulent flows. Flow, Turbulence and Combustion, Vol. 99(2), pp. 279-327

[11] Reyes, D.A., Cooper, J.M. and Girimaji, S.S. (2014): Characterizing velocity fluctuations in partially resolved turbulence simulations. Physics of Fluids, Vol. 26(8), p.085106

[12] Girimaji, S. and Abdol-Hamid, K. (2005): Partially-averaged Navier Stokes model for turbulence: Implementation and validation. In 43rd AIAA Aerospace Sciences Meeting and Exhibit (p. 502)

[13] Basara, B., Krajnovic, S. and Girimaji, S. (2008): PANS vs. LES for computations of the flow around a 3D bluff body. In Proc. of ERCOFTAC 7th Int. Symp.-ETMM7, Lymassol, Cyprus

[14] Girimaji, S.S. and Wallin, S. (2013): Closure modeling in bridging regions of variable-resolution (VR) turbulence computations. Journal of Turbulence, Vol. 14(1), pp. 72-98

[15] Popovac, M. and Hanjalic, K. (2007): Compound wall treatment for RANS computation of complex turbulent flows and heat transfer. Flow, turbulence and combustion, Vol. 78(2), p.177

[16] Basara, B. (2006): Eddy viscosity transport model based on elliptic relaxation approach. AIAA journal, Vol. 44(7), pp. 1686-1690

[17] Girimaji, S.S., Jeong, E. and Srinivasan, R. (2006): Partially averaged Navier-Stokes method for turbulence: Fixed point analysis and comparison with unsteady partially averaged Navier-Stokes. Journal of Applied Mechanics, Vol. 73(3), pp. 422-429

[18] Foroutan, H. and Yavuzkurt, S. (2014): A partially-averaged Navier-Stokes model for the simulation of turbulent swirling flow with vortex breakdown. Int. J. Heat and Fluid Flow, Vol. 50, pp. 402-416

[19] Basara, B., Pavlovic, Z. and Girimaji, S. (2018): A new approach for the calculation of the cut-off resolution parameter in bridging methods for turbulent flow simulation. Int. J. Heat and Fluid Flow, Vol. 74, pp. 76-88.

[20] Jakirlic, S., Kutej, L., Basara, B., and Tropea., C. (2014): Computational Study of the Aerodynamics of a Realistic Car Model by Means of RANS and Hybrid RANS/LES Approaches. SAE Int. J. Passeng. Cars - Mech. Syst. / Vol. 7(2).

[21] Han, X., Krajnovic, S., and Basara, B. (2013): Study of active flow control for a simplified vehicle model using the PANS method. Int. J. of Heat and Fluid Flow. Vol. 42., pp. 1341-1360.

[22] Minelli, G., Hartono, A., Chernoray, V., Hjelm, L., Basara, B., and Krajnovic, S. (2017): Validation of PANS and active flow control for a generic truck cabin. J. of Wind Engineering & Industrial Aerodynamics, Vol. (171), pp.148-160.

[23] Krajnovic, S., Larusson, R., and Basara, B. (2012): Superiority of PANS compared to LES in predicting a rudimentary landing gear flow with affordable meshes. Int. J. of Heat and Fluid Flow. Vol. 37., pp. 109-122.

[24] Jakirlic, S., Kutej, L., Basara, B., and Tropea, C. (2018): "Scale-Resolving Simulation of an 'On-Road' Overtaking Maneuver Involving Model Vehicles," SAE Technical Paper 2018-01-0706, doi:10.4271/2018-01-0706.

[25] AVL FIRE Manual, AVL List GmbH, Graz, Austria. CFD Solver Version, 2010-2019.

[26] Basara, B., Poredos, A., and Gorensek, P. (2016): "Scale-Resolving Simulations of the Flow in Intake Port Geometries," SAE Technical Paper 2016-01-0589, doi:10.4271/2016-01-0589.

[27] Viher, J., Tibaut, P., Basara, B., and Krajnovic, S. (2018): Computational study of a car aerodynamics using the partially-averaged Navier-Stokes approach. Proceedings of AEROVEHICLES 3 - Third International Conference in Numerical and Experimental Aerodynamics of Road Vehicles and Trains, Politecnico di Milano, Italy.

[28] Viher, J. (2019): Numerical simulations of full-scale vehicles using PANS turbulence model. MSc Thesis, University of Maribor, Slovenia.

[29] Basara, B., Krajnovic, S., and Pavlovic, Z. (2014): Computations of unsteady flow around a car model using the Partial-Averaged Navier-Stokes method. Proceedings of AEROVEHICLES 1 - First International Conference in Numerical and Experimental Aerodynamics of Road Vehicles and Trains, Bordeaux, France, June 23-25, 2014.

[30] Trias, F.X., Gorobets, A., and Oliva, A. (2015): Turbulent flow around a square cylinder at Reynolds number 22,000: A DNS study. Comput. Fluids. Vol. 123. pp. 87-98.

[31] Basara, B., Pavlovic, Z., and Girimaji, S. (2020): The prospect and benefits of using the Partial-Averaged Navier-Stokes method for engine flows. SAE Technical Paper SAE Technical paper 2020-01-1107.

[32] Saroha, S., Sinha, S., and Lakshmipathy S. (2019): Evaluation of PANS method in conjunction with nonlinear eddy viscosity closure using OpenFOAM. Int. J. Heat and Fluid Flow Vol. 29 (3), pp. 949-980.

[33] Basara, B. (2014): Fluid flow and conjugate heat transfer in a matrix of surface-mounted cubes: A PANS study. Int. J. Heat and Fluid Flow, Vol. 51, pp. 166-174.

[34] Chakraborty, K., Saroha, S., and Sinha, S. (2019): An Openfoam-based Extension of Low-re K-epsilon Model to the Partially-averaged Navier-stokes (PANS) Methodology for Simulating Separated Flows with Heat Transfer. Journal of Fluids Engineering, Paper number: FE-19-1391, doi:10.1115/1.4045209.

[35] Lav, C., Richard D. Sandberg, and Jimmy Philip (2019): A framework to develop data-driven turbulence models for flows with organised unsteadiness. Journal of Computational Physics, Vol. 383, pages 148-165.

Applications of an Embedded Seamless Hybrid RANS/LES Approach for Turbulent Dispersion over Complex Urban Areas

S. Kenjereš[1]

[1] *Faculty of Applied Sciences, Delft University of Technology, Van der Maasweg 9, 2629 HZ Delft, The Netherlands*

Abstract

This work presents an application of a RANS/LES hybrid approach in simulating flows and turbulent dispersion in complex urban areas. It is demonstrated that the hybrid approach correctly captures the time-dependent behavior of the wake regions behind buildings, resulting in improvements of the total turbulent kinetic energy and, consequently, the turbulent dispersion of pollutants. The seamless variant of the hybrid RANS/LES approach proposed here, based on a dynamic evolution of the local interface zone, in combination with a generic-reaction set atmospheric chemistry model, proved to be numerically efficient and robust, and is recommended for future investigations of turbulent dispersion in real-scale city domains.

1 Introduction

Urban pollution remains one of the key problems in the development of rapidly growing cities around the world. Local city pollution is often triggered by a sudden change of the local meteorological conditions coupled with an increase in industrial and/or traffic emissions. This example illustrates the importance of having a predictive tool based on a solid physics foundation able to provide local wind flow intensity and concentrations of reactive scalars that pose a threat for human health. In the present contribution, we provide evidence that an integrated computational fluid dynamics and computational atmospheric chemistry model can serve as a basis for such a predictive tool. The essential ingredient of such an integrated model is its ability to deal with localized predictions of the wind flow and turbulence, which intensity determines the dispersion of reactive pollutants in urban areas. The eddy-viscosity based approach in modeling of environmental turbulence, due to its simplicity (requires solving two additional transport equations, of the turbulent kinetic energy and its dissipation rate), is still very popular for predicting airflow and dispersion in and above complex urban areas. In the present work, we attempt to improve some of the current limitations of the simple two-equation eddy-viscosity model by incrising sensitivity to local flow instabilities through hybrid RANS/LES approach. This is done through a redefinition of the turbulence model coefficient dependency on the turbulent length-scale ratio obtained from RANS and characteristic mesh size. Note that this approach does not require any a priori definition of RANS and LES zones, i.e., the RANS/LES interface is temporarily and spatially self-adjusting. We hypothesize that a better prediction of turbulence in the wake of buildings will lead to improved predictions of the pollutant distributions. The turbulent dispersion of pollutants is modeled through an additional transport equation of concentration (passive scalar) or is coupled with an atmospheric chemistry model (reactive scalars).

2 Governing equations

The phenomena of the turbulent dispersion of a pollutant over a complex urban areas can be described by the following set of governing equations:

$$\frac{\partial U_i}{\partial t} + U_j \frac{\partial U_i}{\partial x_j} = \frac{\partial}{\partial x_j}\left[\nu\left(\frac{\partial U_i}{\partial x_j} + \frac{\partial U_j}{\partial x_i}\right) - p\delta_{ij} - \overline{u_i u_j}\right] \quad (1)$$

$$\frac{\partial C^{(k)}}{\partial t} + U_j \frac{\partial C^{(k)}}{\partial x_j} = \frac{\partial}{\partial x_j}\left[\mathcal{D}_c \frac{\partial C^{(k)}}{\partial x_j} - \overline{c^{(k)} u_j}\right] \pm R_c^{(k)} \quad (2)$$

where U_i is the velocity, p is the pressure, $\overline{u_i u_j}$ is the turbulent stress tensor, $C^{(k)}$ is the concentration of the species (k), $\overline{c^{(k)} u_j}$ is the turbulent concentration flux, $R_c^{(k)}$ is the reaction rate. The latter is zero for the dispersion of a passive (non-reactive) scalar. The turbulent stress tensor $(\overline{u_i u_j})$ and turbulent mass flux of species $(\overline{c^{(k)} u_i})$ are obtained by applying the eddy-viscosity and generalized gradient diffusion hypothesis approaches, respectively, which can be written as:

$$\overline{u_i u_j} = \frac{2}{3} k \delta_{ij} - \nu_t \left(\frac{\partial U_i}{\partial x_j} + \frac{\partial U_j}{\partial x_i}\right) \quad (3)$$

$$\overline{c^{(k)} u_i} = -C_\phi \overline{u_i u_j} \frac{\partial C^{(k)}}{\partial x_j} \quad (4)$$

To have a fully closed system of governing equations, additional transport equations of the turbulent kinetic energy and its dissipation rate are introduced:

$$\frac{\partial k}{\partial t} + U_j \frac{\partial k}{\partial x_j} = \frac{\partial}{\partial x_j}\left[\left(\nu + \frac{\nu_t}{\sigma_k}\right)\frac{\partial k}{\partial x_j}\right] + P_k - \varepsilon \quad (5)$$

$$\frac{\partial \varepsilon}{\partial t} + U_j \frac{\partial \varepsilon}{\partial x_j} = \frac{\partial}{\partial x_j}\left[\left(\nu + \frac{\nu_t}{\sigma_\varepsilon}\right)\frac{\partial \varepsilon}{\partial x_j}\right] + \frac{1}{T}\left(C_{\varepsilon 1} P_k - C_{\varepsilon 2}\varepsilon\right) \quad (6)$$

with

$$\nu_t = C_\mu \; k \; T, \quad T = \min\left(\frac{k}{\varepsilon}, \frac{0.6}{\sqrt{6} C_\mu |S|}\right) \quad (7)$$

where the characteristic time-scale (T) is defined in accordance with [1],[2].

3 Merging RANS with LES

We employ three different merging strategies between the RANS and LES approach. The first approach is to activate the time-dependent terms of the governing RANS equations, where all turbulence model coefficients are identical to their standard RANS values, [3, 4]. This method proved to be suitable for flows where a strong natural forcing due to external body forces is present. Some examples include the turbulent Rayleigh-Bénard convection, where due to presence of thermal buoyancy, highly unstable flow and heat transfer are generated, and where the application of (T)RANS provided accurate predictions of heat transfer over a range of Rayleigh numbers, which is not accessible to other eddy-resolving techniques (such as DNS or wall-resolving LES), [3, 4, 5]. The identical approach was also successfully applied in capturing time-dependent eddy-structure in flows characterized by the combined effects of thermal buoyancy and the Lorentz force, [6]. In this approach, with further refinement of the numerical mesh, the eddy structures captured are similar in size as for the coarser mesh, i.e., we do not have asymptotic behavior towards the DNS.

The asymptotic behavior towards the DNS with mesh refinement is achieved in the second approach, where we redefine the model coefficient in the dissipation rate of the turbulent kinetic energy equation, $C_{\varepsilon 2}$ such, that it becomes a function of the characteristic ratio between modeled and resolved length scales (i.e. similarly to the PITM approach of [7],[8]) as ([4]):

$$C_{\varepsilon 2} = C_{\varepsilon 1} + \frac{1}{\alpha}\left(C_{\varepsilon 2} - C_{\varepsilon 1}\right), \qquad \alpha = max\left(1, \frac{L^{RANS}}{L^{LES}}\right),$$
$$L^{RANS} = \frac{k^{3/2}}{\varepsilon}, \quad L^{LES} = \left(\Delta_x \Delta_y \Delta_z\right)^{1/3} \tag{8}$$

where $\Delta_{x,y,z}$ are orthogonal projections of the control volume surfaces. The seamless parameter α, equal to one, corresponds to the original (T)RANS approach. For the $\alpha >> 1$, the values of the $C_{\varepsilon 2}$ are asymptotically reaching $C_{\varepsilon 1}$, generating an extensive level of the dissipation rate, which makes negligible the modeled contribution of the turbulent kinetic energy, i.e. a zero-turbulent viscosity limit is reached, and we practically have a quasi DNS approach. This approach satisfies both asymptotic behaviors of the integrated model: (T)RANS for a coarse mesh and DNS for a fully resolving numerical mesh.

To obtain a better control over the intermediate mesh resolutions, we apply the following merging strategy with LES instead of DNS, as ([9]):

$$\nu_t^{LES} = \left(C_s \Delta\right)^2 |S|, \quad |S| = \left(2 S_{ij} S_{ij}\right)^{1/2},$$
$$\nu_t = \nu_t^{RANS} \cdot min\left(\frac{\nu_t^{LES}}{\nu_t^{RANS}}, 1\right) \tag{9}$$

with Smagorinsky coefficient C_s=0.1, characteristic filter Δ=L^{LES} and ν_t^{RANS} is the turbulent viscosity calculated from the (T)RANS model. The final long-term time-averaged second-order moments are calculated as a sum of the modeled and resolved contributions. For the turbulent kinetic energy, we can write $k_{tot} = k_{res} + k_{mod}$, where the modeled part is evaluated as $k_{mod} = \frac{1}{N}\sum_{n=1}^{N} k^{(n)}$, where $k^{(n)}$ is obtained from its own transport equation for a particular time step (n). The resolved part of the TKE is calculated as $k_{res} = \frac{1}{2N}\sum_{n=1}^{N}\left(U_i^{(n)} - \overline{U_i}\right)^2$. Similarly, the total turbulent mass flux is calculated as a sum of the modeled and resolved contributions: $(\tau_{ci})_{tot} \equiv (\overline{cu_i})_{tot} = (\overline{cu_i})_{mod} + (\overline{cu_i})_{res}$, with $(\overline{cu_i})_{mod} = \frac{1}{N}\sum_{n=1}^{N}\overline{cu_i}^{(n)}$ and $(\overline{cu_i})_{res} = \frac{1}{N}\sum_{n=1}^{N}\left(C^{(n)} - \overline{C}\right)\left(U_i^{(n)} - \overline{U_i}\right)$. For both - modeled and resolved contributions - data are collected during the time-dependent simulations (collecting on a run).

4 Numerical method

The complete set of discretised governing equations (Eqs.(1)-(9)), together with the corresponding atmospheric chemistry model for reactive species, is solved numerically using an in-house finite-volume based Navier-Stokes computational code design for general structured non-orthogonal geometries, [3, 4, 5, 9, 10]. Here we will provide a short overview of the most essential numerical details. The collocated arrangement is used for all transport variables. The Rhie-Chow interpolation is used to prevent decoupling between velocity and pressure. The standard SIMPLE algorithm is used to couple the momentum and continuity equations (the corrector-predictor iterative procedure). The second-order central differencing scheme is used for diffusive terms of governing equations, while the second-order quadratic- or linear-upwinding scheme is used for the convective terms of the momentum and turbulence parameters equations, respectively. The time-dependent terms are discretised by a fully implicit second-order three consecutive time-steps scheme.

5 Results and discussion

5.1 Dispersion of the passive scalar at the laboratory scale

For the validation of the numerical approach presented, we select experimental studies of [11] performed in a large water channel (with a length of 10 m, a width of 1.5 m, and a depth of 1.0 m, respectively). The measurements were performed by the combined Laser Doppler Velocimetry (LDV) (for velocity field) and Laser-Induced Fluorescence (LIF) (for concentration field). Various heterogeneous structures were generated at the bottom wall, mimicking buildings within complex urban areas. For results presented here, we have selected a configuration containing 17×16 cubes (with a height 'h' in the streamwise and spanwise directions, respectively, with a central 'tower-like' object with a characteristic height of '3h' (shown in red), Figure (1). The cube height is h=31.75 mm. Just behind this 'tower-like' structure, an opening at the bottom wall is introduced through which a color dye is injected, mimicking a passive pollutant release. The specific mass flow rate of 12 ml/min is imposed for the dye tracer through this opening, with a characteristic Schmidt number of Sc=1920. The primary inlet conditions are specified to correspond to the measured profiles of the streamwise velocity and turbulent kinetic energy in the empty channel (no obstacles).

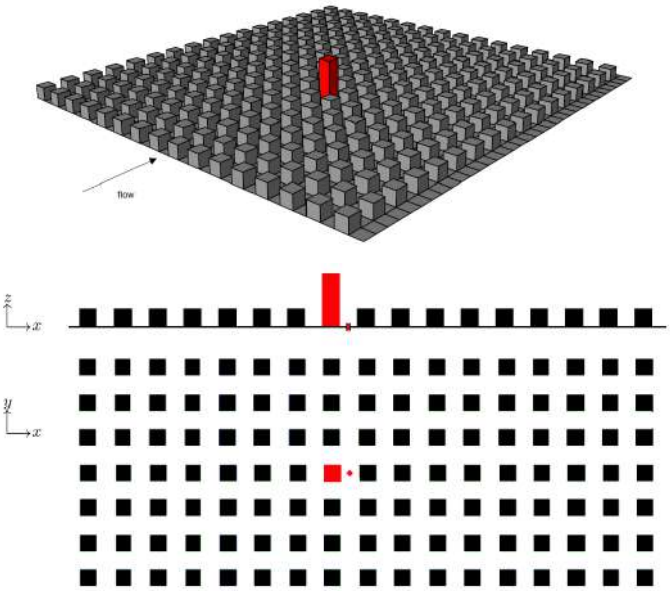

Figure 1: The geometry of the experimental setup of [11] for flow over an array of cubical obstacles (of height 'h') with a central tower (of height '3h'). The flow is from left to right. The pollutant source is located behind the tower at ground level in the middle of the street canyon, as indicated with the red circle

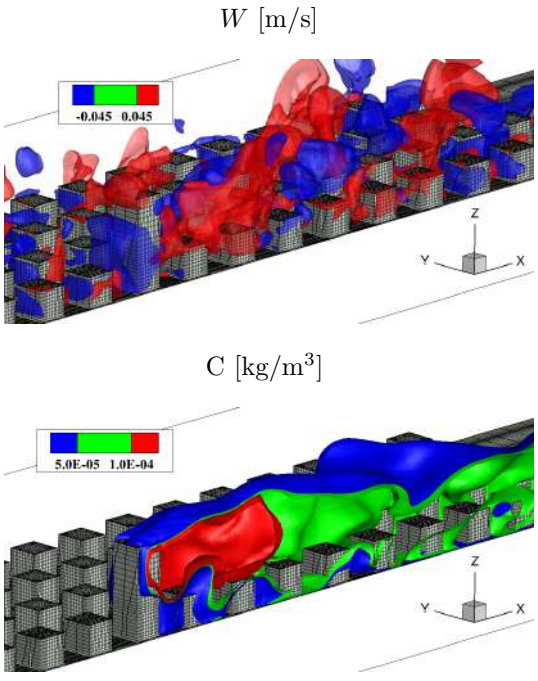

Figure 2: Top- isosurfaces of the vertical velocity W = 0.05 m/s (red) and -0.05 m/s (blue); Bottom- isosurfaces of the passive pollutant; All plots are done for an arbitrary instantaneous snapshot of a hybrid (T)RANS/(V)LES method of [9] for the configuration shown in Figure (1) (for clarity, only one-half of the simulated domain in the spanwise direction is shown), [9]

The characteristic Reynolds number based on the free-stream velocity (U_0 = 0.38 m/s) and height of tower-structure is Re= 3.6×10^4. The simulation domain includes the inlet-patch (with a distance of 6h between the inlet and the first row of obstacles), the outlet-patch (with a characteristic distance of 90h between the last row of obstacles and outlet), the spanwise-patches (with

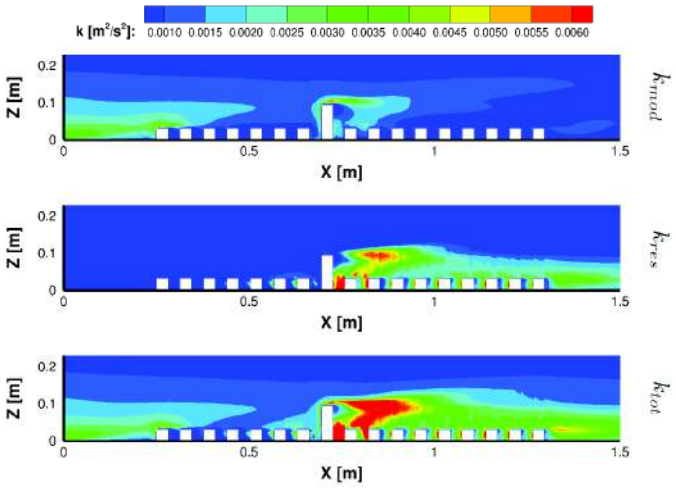

Figure 3: Contours of the modeled (k_{mod})-top, resolved (k_{res})-middle and total (k_{tot})-bottom turbulent kinetic energy in the central vertical plane. Results of the long-term time-averaged hybrid (T)RANS/(V)LES method, [9]

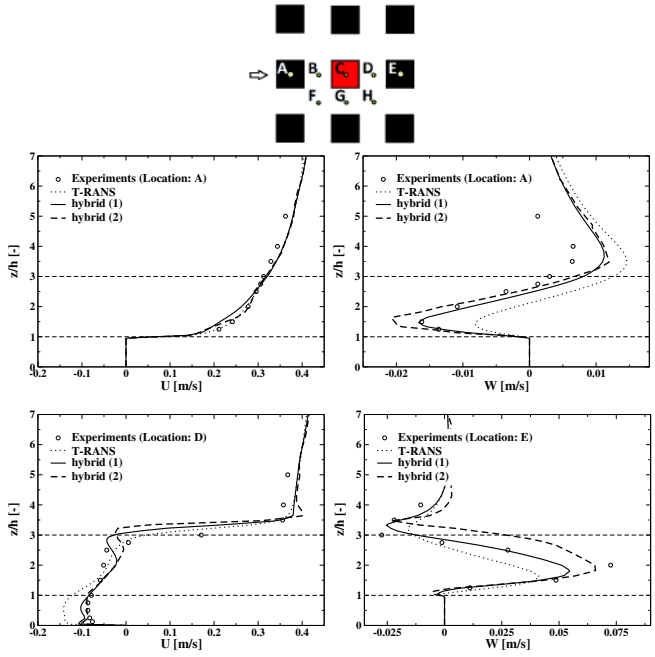

Figure 4: The vertical profiles of the long-term time-averaged streamwise ($\overline{U}$-left) and vertical velocity component ($\overline{W}$-right) at characteristic locations (A-D-E) in the proximity of the tower (red block) (locations are indicated in the top figure), [9]

5h distances between the obstacles and boundaries of the domain), and finally, the vertical patch (with a distance of 10h between the highest obstacle and the top of the domain). The symmetry boundary conditions are applied for the domain boundaries along the spanwise direction and at the top boundary. The computational mesh used is generated, such that it is refined in the proximity of buildings and the bottom wall. About 20 control volumes are used to represent the cubes, whereas about 30 control volumes are employed in the space between (street canyons). The non-dimensional wall-distance was kept to be $20 < y_n^+ < 50$ within the street-canyons. The entire simulation domain is represented by $584 \times 226 \times 50 \approx 6.6$M CVs. The mesh used pro-

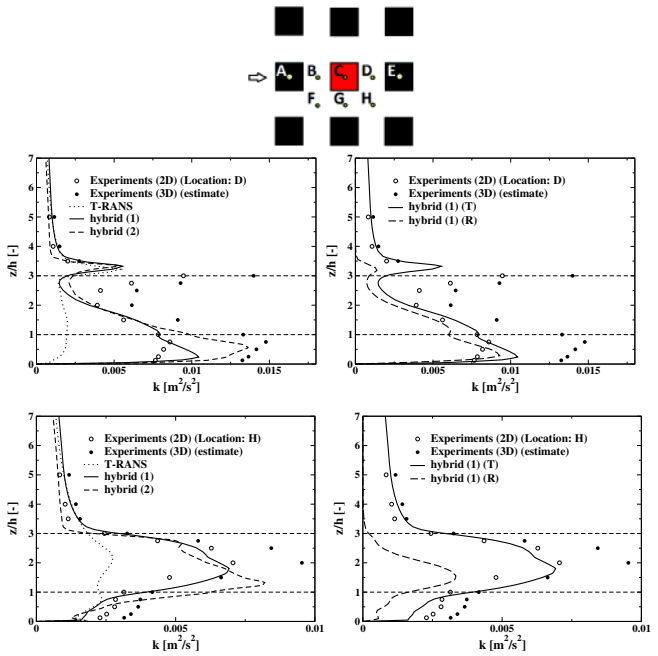

Figure 5: Vertical profiles of the turbulent kinetic energy at characteristic locations (D-H): the total contributions (k_{tot}) from experiments, (T)RANS, hybrid (1) and (2) methods (-left); the total (k_{tot}) and resolved (k_{res}) contributions of the hybrid method (1) (-right). Note that two-dimensional LDV experiments provide k_{2D}=0.5 $(\overline{uu} + \overline{ww})$ and we also introduced estimated k_{3D}=0.5 $(\overline{uu} + 2\overline{ww})$, [9]

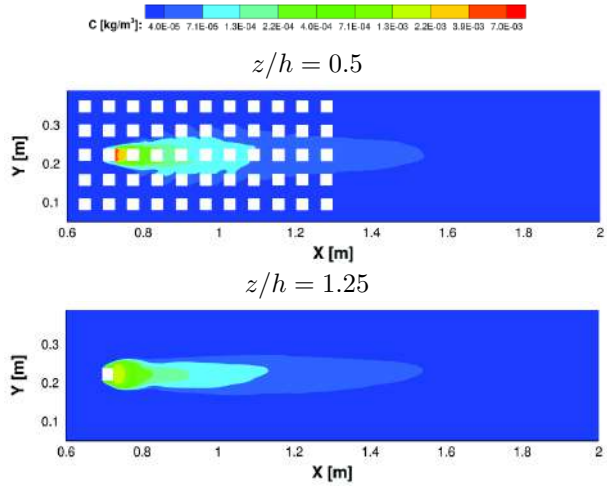

Figure 6: Contours of the mean concentration in characteristic horizontal planes, z/H=0.5 (-top) and z/H=1.25 (-bottom). The results obtained with hybrid (T)RANS/(V)LES approach, [9]

vided a typical ratio between the grid control volume size ($\Delta = \Delta V^{1/3}$) and the estimated Kolmogorov length scale ($\eta = \left(\nu^3/\varepsilon\right)^{1/4}$) to be in the 10-65 range. Note that due to the high value of the Schmidt number, the present configuration and range of its working parameters are challenging for classical DNS and LES. In the present study, we would like to demonstrate capabilities of the hybrid (T)RANS/(V)LES approach in capturing essential features of the flow, turbulence and mass transfer when the RANS-type of the numerical mesh is used. The instantaneous distributions of the vertical velocity (W) and passive scalar (C), calculated by the hybrid approach, for an arbitrary time-step, are shown in Figure (2). It can be seen that hybrid simulation revealed the vortex shedding behind the tower-structure, and production of intermittent flow structures. Because of the placement of the pollution source in the proximity of the tower-structure, the proper capturing of this intermittent behavior of the flow structures will have a crucial role for the distribution of the concentration. The contours of the modeled, numerically resolving and total contributions of the long-term time-averages turbulent kinetic energy in the central vertical plane are shown in Figure (3). It can be seen that the numerically resolving contribution is particularly important in the tower-wake region. The vertical profiles of the mean horizontal and vertical velocity components at different locations are shown in Figure (4). It can be seen that the hybrid (T)RANS/(V)LES approach provides the closest agreement with the experiment at all locations. Similarly, the vertical profiles of the total (-left) and of numerically resolving (-right) contributions of the TKE at various locations, are shown in Figure (5). It can be seen that numerically resolving contributions are important in the wake regions, where significantly improved agreement with measurements is obtained. This improved prediction of the turbulent kinetic energy, and consequently, of the total eddy viscosity, which in turn generates a more intensive turbulent mixing, also resulted in improved distribution of the mean concentration (which contours are shown in Figure (6) and spanwise profiles in Figure (7)). Note that the classical (T)RANS approach is not able to predict the levels of concentration upstream from the source (Figure (7)(a)) and is also predicting significant differences in the peak values of the mean concentration at the source location (Figure (7)(a) as well as farther downstream (Figure (7)(c)).

5.2 Reactive scalars dispersion at the real city neighborhood scale

In the second example, we demonstrate the potential of the hybrid (T)RANS/(V)LES approach in simulating city-scale environmental situations. Here, we apply an integrated approach by combining the flow and turbulence solver with an atmospheric model. The atmospheric model used is the generic reaction set (GRS) model, which includes additional transport equations of reactive scalars (i.e. $k = NO_2$, NO, O_3, ROC, RP, SGN and SNGN, in Equation (2)) which describes local ozone generation or depletion due to exhaust gases emitted in traffic. For more details of the atmospheric chemistry model, see [13]. The simulated domain is shown in Figure (8) and represents a part of the neighborhood (2×2 km^2) of the city of Rotterdam in The Netherlands. [13],[12]. A locally refined numerical mesh in the proximity of the buildings (in total 1800 blockage elements are included with a typical mesh size between 1 and 2.5 m in the proximity of the buildings) and major traffic emission sources (three major roads), and gradually increasing mesh size in the vertical direction, resulted in a RANS-type of a numerical grid with a total of 20×10^6 CVs, Figure (9). The typical meteorological conditions for springtime (light breeze wind coming from West with 2 m/s and characteristic turbulence intensity of 5%) and the predefined intensity of the traffic (measured traffic intensity with an emission of 5×10^{-2}, 5×10^{-3} and 5.5×10^{-3} ppm/s for NO, NO_2 and ROC, respectively, with $NO_2/NO = 1/10$ and $ROC/NO_x = 1$ and the initial background ozone concentration of 0.02 ppm) are simulated. Because of the quite steady incom-

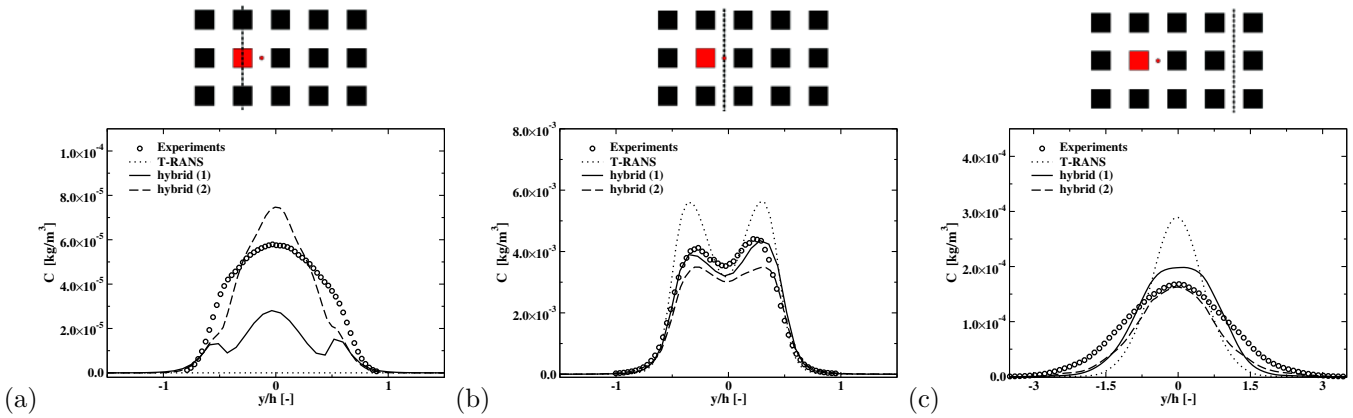

Figure 7: The spanwise mean concentration profiles along the $x/h = -1$ at $z/h = 3.25$ (a), $x/h = 0$ (exactly at the pollution source) at $z/h = 0.5$ (b), and $x/h = 4$ and $z/h = 1.25$ (c) - comparison with experiment, [9]

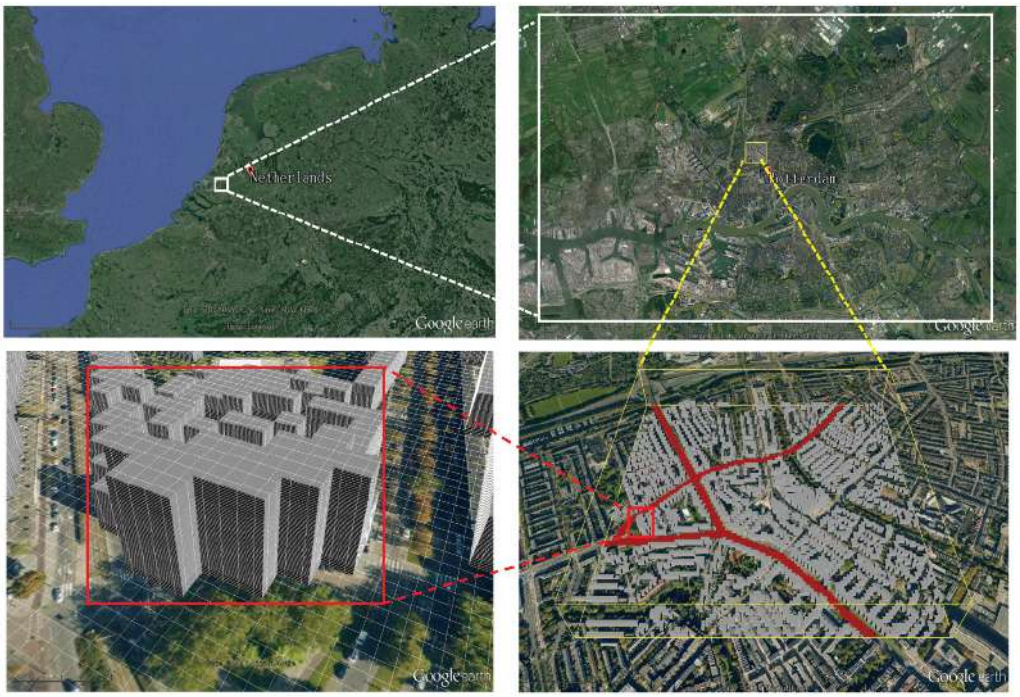

Figure 8: The simulated domain for a city-scale application: the neighborhood scale of the city of Rotterdam in The Netherlands, covers 2×2 km, containing approximately 1800 obstacles (representing parts of buildings). Three major traffic emission sources are indicated in red, [12]. The generic reaction set (GRS) model is used to model the atmospheric chemistry, [13]

ing wind conditions and traffic intensity (lasting for at least a few hours), the long-term time-averaged concentrations are analyzed, Figure (10). Here, the predicted concentration of NO_2 and O_3 are plotted in the pedestrian level plane (z=2 m). It can be seen that the local distribution of NO_2 shows clustered regions in the proximity of the main roads, Figure (10)(a). In contrast to the NO_2 distribution, the ozone (O_3) contours at the pedestrian level ($z = 2$ m) illustrate significantly more complex behavior, Figure (10)(b). Now, the local minima are observed in the proximity of the roads, while the maximum values are non-uniformly distributed in the middle of the simulated domain. These peaks in O_3 are the result of complex local interactions between the strength of the flow (through the mechanism of convection), the intensity of turbulence (through the mechanism of turbulent diffusion), and finally, the strength of the chemical reaction (source/sink term contributions of chemical species). This variation in the local concentration of species additionally illustrates the importance of a fully coupled computational fluid dynamics and atmospheric chemistry model. Despite the fact that the capabilities of the hybrid (T)RANS/(V)LES approach were not explored fully, we suggest that the proof of concept has been well demonstrated, at least under conditions of steady wind flow and steady traffic emission. It is easy to expand the current simulations with a time-varying change of the meteorological conditions (e.g., changes in the wind intensity, direction, energy of fluctuations, etc.) as well as local traffic conditions (e.g., a daily variation of the traffic intensity) (work currently in progress).

6 Conclusions

In the present work, we demonstrated the capabilities and potential of an embedded seamless hybrid RANS/LES approach in prediction of flow, turbulence, and dispersion over complex urban areas. The validation of the proposed approach for the measured laboratory

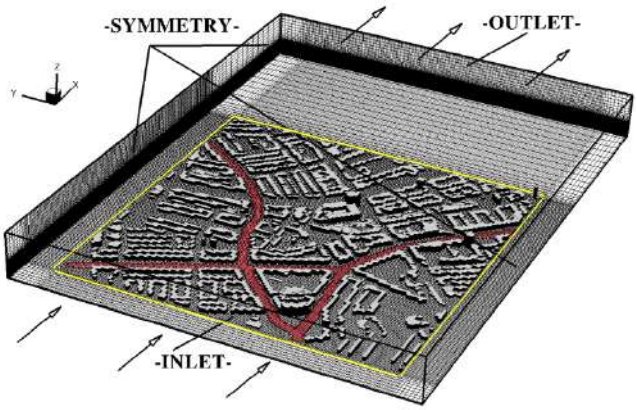

Figure 9: The numerical mesh, extensions of the simulated domain, buildings, roads, and applied numerical mesh (approximately 20×10^6 control volumes are used for computation), [12]

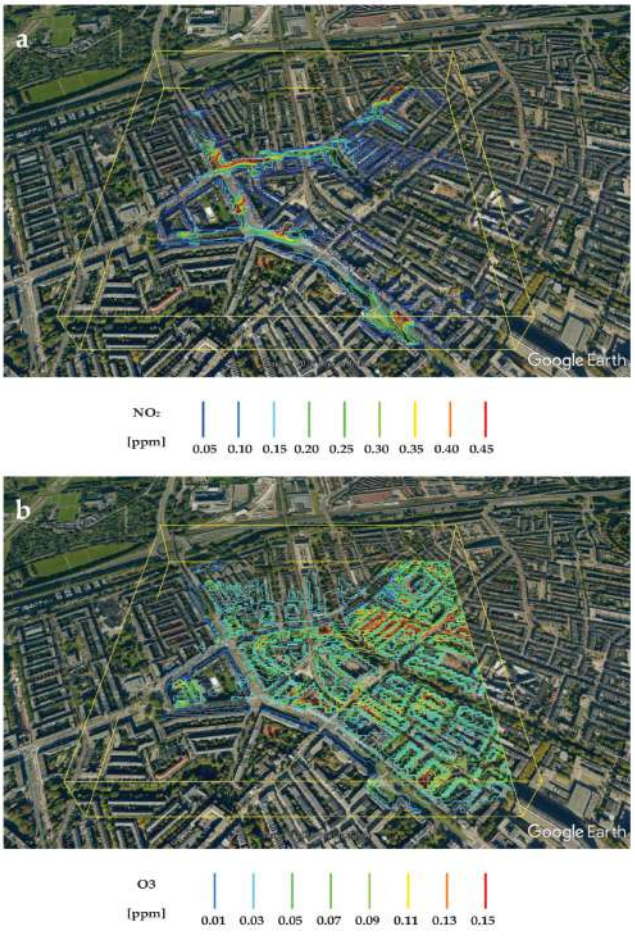

Figure 10: Contours of the mean concentration of NO_2 and O_3 at the pedestrians level (at $z = 2$ m above ground). Results obtained by integrated (T)RANS/GRS approach, [12], [13]

condition revealed a significant improvement of the total turbulent kinetic energy in the proximity of the buildings. This improvement is because of the contribution of numerically resolved intermittent flow structures captured by the hybrid approach. The better agreement of the turbulent kinetic energy also produced a significantly improved prediction of the long-term time-averaged concentration profiles at all locations considered. Furthermore, this hybrid approach coupled with an atmospheric chemistry model can be very useful for localized predictions of industrial- or traffic-induced pollution in real city-scale domains.

References

[1] P. A. Durbin, "On the k-ε Stagnation Point Anomaly," *Int. J. Heat and Fluid Flow*, vol. 17, pp. 89–90, 1996.

[2] G. Medic and P. A. Durbin, "Toward Improved Prediction of Heat Transfer on Turbine Blades," *ASME J. Turbomachinery*, vol. 124, pp. 187–192, 2002.

[3] S. Kenjereš and K. Hanjalić, "Transient analysis of Rayleigh-Bénard convection with a RANS model," *Int. J. Heat and Fluid Flow*, vol. 20, no. 3, pp. 329–340, 1999.

[4] S. Kenjereš and K. Hanjalić, "LES, T-RANS and hybrid simulations of thermal convection at high Ra numbers," *Int. J. Heat and Fluid Flow*, vol. 27, no. 5, pp. 800–810, 2006.

[5] S. Kenjereš and K. Hanjalić, "Tackling Complex Turbulent Flows with Transient RANS," *Fluid Dynamics Research*, vol. 41, no. 012201, pp. 1–32, 2009.

[6] S. Kenjereš, "On modeling and eddy-resolving simulations of flow, turbulence, mixing and heat transfer of electrically conducting and magnetized fluids: A review," *Int. J. Heat and Fluid Flow*, vol. 73, pp. 270–297, 2018.

[7] B. Chaouat and R. Schiestel, "A new partially integrated transport model for subgrid-scale stresses and dissipation rate for turbulent developing flows," *Phys. Fluids*, vol. 17, no. 065106, pp. 1–19, 2005.

[8] R. Schiestel and A. Dejoan, "Towards a new partially integrated transport model for coarse grid and unsteady flow simulations," *Theor. Comput. Fluid Dyn.*, vol. 18, no. 6, pp. 443–468, 2005.

[9] S. Kenjereš, S. de Wildt, and T. Busking, "Capturing Transient Effects in Turbulent Flows over Complex Urban Areas with Passive Pollutants," *Int. J. Heat and Fluid Flow*, vol. 51, pp. 120–137, 2015.

[10] K. Hanjalić and S. Kenjereš, "Some Developments in Turbulence Modelling for Wind and Environmental Engineering," *Journal of Wind Engineering and Industrial Aerodynamics*, vol. 96, no. 10-11, pp. 1537–1570, 2008.

[11] T. Hilderman and R. Chong, "A laboratory Study of Momentum and Passive Scalar Transport and Diffusion Within and Above a Model Urban Canopy - Urban Arrays Report," *Coanda Research and Development Corporation Technical Report*, vol. CRDC00327d, pp. 1–530, 2004.

[12] D. Liu and S. Kenjereš, "Google-Earth Based Visualizations for Environmental Flows and Pollutant Dispersion in Urban Areas," *Int. J. Environmental Research and Public Health*, vol. 14, no. 3, pp. 1–16, 2017.

[13] C. Muilwijk, P. Schrijvers, S. Wuerz, and S. Kenjereš, "Simulations of photochemical smog formation in complex urban areas," *Atmospheric Environment*, vol. 47, pp. 470–484, 2016.

Hybrid URANS/LES Approaches for Internal Combustion Engine Simulations

F. Held and C. Hasse

Simulation of reactive Thermo Fluid Systems
Technische Universität Darmstadt, Otto-Berndt-Straße 2, 64287 Darmstadt, Germany

Abstract

The development of future internal combustion engines will heavily rely on 3D Computational Fluid Dynamics (CFD). The reliability of such simulations strongly depends on the physical models and numerics which are used. While the vast majority of studies in the context of engines have employed URANS approaches for turbulence modeling, there is a strong and increasing interest in transitioning to scale-resolving techniques such as large eddy simulations (LESs). In that respect, hybrid URANS/LES approaches are particularly interesting, since they allow RANS modeling to be used for the wall boundary layers or regions with insufficient resolutions, while the full benefits of LES can be exploited in the usually sufficiently well-resolved inner part of the cylinder, where the turbulence interacts with the liquid fuel spray and chemical reactions. This article reviews aspects of hybrid URANS/LES approaches for engines and discusses selected results ranging from validation studies in simplified geometries to realistic engine applications. Finally, future challenges will be addressed to further promote the use of scale-resolving models.

1 Scale-resolving simulations of internal combustion engines

The energy transition is a global challenge with a major economic and social impact. In the foreseeable future, combustion will still meet a substantial part of the world's primary energy demand. In particular, the internal combustion (IC) engine will continue to be an important technology for mobility and transport. In that context, it will benefit from the introduction of renewable fuels, which are leading to substantial changes in combustion system design. In combination with the need for increased efficiency and near-zero CO_2 pollutant emissions, future engine development will have to cope with an increasing number of challenges and in that context it will heavily rely on Computational Fluid Dynamics (CFD) in combination with experiments.

The combustion engine is a highly complex system with moving components (intake and exhaust valves, piston), numerous thermofluidic phenomena including turbulence, multi-phase flows and chemical reactions, which are strongly coupled. The cause-and-effect chain in IC engines is illustrated in Figure (1), using the example of a gasoline engine. The cause-and effect chain starts with the intake stroke of the engine and the associated formation of a large-scale structure (tumble), which is specifically important for the mixing later in the cycle. This is followed by the injection of fuel. Here, the jet breakup and the formation of the smallest fuel droplets are particularly relevant. The subsequent evaporation of the droplets and the turbulent mixture formation provide the initial condition for the subsequent combustion. Starting from the spark ignition, a flame kernel initially forms which further develops into a fully turbulent propagating flame. The final phase is strongly influenced by the interaction of the flame with the turbulent wall boundary layer.

Figure (1) also denotes a number of so-called unit problems, e.g. wall boundary layers, vortex shedding and droplet-droplet interaction. Unit problems of this kind are usually employed to develop and validate models. Thus, the specific complexity of modeling IC engines is directly connected to the large number of unit problems/sub-processes and their strongly non-linear coupling. All of this must be handled in a single CFD framework when aiming for predictive simulations.

From the above discussion it becomes clear that turbulence plays a major role troughout the engine cycle. Thus, the modeling approach for turbulence and how it interacts with the liquid phase and the chemical reactions is crucial for the overall quality of the simulation. In that context, scale-resolving simulations (SRSs) are particularly appealing, since a substantial portion of the turbulence is resolved and does not need to modelled as in (U)RANS. However, engine research and development currently still heavily relies on URANS approaches, which can only predict the average cycle. Single-cycle phenomena such as knock or misfire or more generally cycle-to-cycle variations (CCVs) can only be predicted by SRSs. Consequently, there is increasing interest in SRSs for IC engines. Recent reviews can be found in [2] and [3], the latter focussing specifically on combustion process development. A recent survey among academic and industrial stakeholders confirmed the high interest in SRSs [4].

In the case of LESs for IC engines, moving geometries with locally / temporally changing resolutions and turbulent wall boundaries are particularly challenging. Taking the example of wall-bounded turbulence at high Reynolds number, a URANS simulation requires grid refinement in the wall-normal direction only. However, for wall-resolved LES, the grid needs to be refined isotropically in all three directions. This leads to a quadratic increase in the number of grid points with the Reynolds number in LES, whereas only a moderate logarithmic dependence can be expected in URANS. To cope with this challenge, a hybrid strategy using URANS modeling in the (underresolved) wall region and LES in the free stream is particularly promising, since an approach of this type can resolve large-scale coherent and smaller, i.e. intermediate-scale, fluctuations in the free flow. These hybrid approaches were originally developed for aerodynamic applications. During the last 10 years, a number of studies (also including contributions from the author's group) have been published confirming the potential for engine simulations. In the following sections we

Figure 1: Cause-and-effect chain in an internal combustion engine. Individual unit problems for the computational simulation are highlighted [1]. The focus of this article is especially on the flow phenomena depicted in the left subfigure (Intake Flow)

present some of our results, showing not only the significant potential but also the associated challenges of hybrid URANS/LES approaches for IC engine simulations.

2 Hybrid approaches

In recent years, a large number of scale-resolving methods have been developed and successfully applied in the context of engines. Not just the classic Smagorinsky model [5] but also other models such as the WALE [6] and Sigma model [7] are worth mentioning. As this piece focuses on hybrid procedures, these models will not be discussed further. A comprehensive comparison including hybrid models was carried out in [8] for a standard engine benchmark case. In the following we briefly describe DES-SST and SAS-SST as two representative hybrid approaches, which we have used successfully in the past. Correspondingly, this is not a comprehensive overview of all hybrid approaches but rather a subjective selection based on our own experience.

DES-SST model

The DES-SST model is a hybrid LES/URANS model developed by Travin et al. [9]. It is based on the SST two-equation URANS approach by Menter [10], which solves additional transport equations for the turbulent kinetic energy k and the turbulent frequency ω. The dissipation term for the k-equation is modified thus

$$\varepsilon = \frac{k^{\frac{3}{2}}}{L_{\mathrm{DES}}} \tag{1}$$

with the modified turbulent length scale L_{DES}. Depending on the available spatial resolution in the domain, the turbulent length scale is switched as follows

$$L_{\mathrm{DES}} = \min(L_t, C_{\mathrm{DES}}\Delta) \quad \text{with} \quad L_t = \frac{k^{\frac{1}{2}}}{\beta\omega}\,, \tag{2}$$

where L_t describes the turbulent length scale calculated using the unmodified SST URANS approach. An additional limiter is introduced to avoid grid-induced separation and leads to the final formulation for the dissipation term:

$$\varepsilon = \frac{k^{\frac{3}{2}}}{L_t} F_{\mathrm{DES}} \quad \text{with} \quad F_{\mathrm{DES}} = \max\left(\frac{L_t}{C_{\mathrm{DES}}\Delta}(1 - F_{\mathrm{SST}}), 1\right). \tag{3}$$

Choosing a constant blending function $F_{\mathrm{SST}} = 0$ leads to the original approach. For the studies discussed in this review a more conservative approach with $F_{\mathrm{SST}} = F_1$ is chosen, where F_1 describes the blending function according to the original SST model proposed by Menter [10].

It should be mentioned that both the k-ε and the k-ω branch exist in the SST-based DES model. Therefore, Travin et al. [9] proposed an individual calibration of the corresponding C_{DES} value:

$$C_{\mathrm{DES}} = (1 - F_{\mathrm{SST}})C_{\mathrm{DES}}^{k\text{-}\varepsilon} + F_{\mathrm{SST}}C_{\mathrm{DES}}^{k\text{-}\omega}\,. \tag{4}$$

SAS-SST model

The scale-adaptive simulation (SAS) approach, contrary to the DES approach, does not formally belong to the hybrid RANS/LES methods. It was proposed by Menter and Egorov et al. [11, 12] and is based on Rotta's exact transport equation for the two-point correlation, which is a time-averaged quantity. Due to the fact that this model is capable of resolving fluctuations smaller than the integral length scales, it is also often referred to as hybrid model. Several formulations are available, but the basic idea can always be traced back to [13]. A modified scale-determining ω equation can be derived from the two-point correlation as

$$\frac{D(\rho\omega)}{Dt} = \mathrm{P}_\omega + \mathrm{Q}_{\mathrm{SAS}} + \mathrm{Diff}_\omega - \mathrm{D}_\omega + (1 - F_1)\,\frac{2\rho}{C_\omega\omega}\frac{\partial k}{\partial x_j}\frac{\partial \omega}{\partial x_j}\,, \tag{5}$$

with the additional source term

$$\mathrm{Q}_{\mathrm{SAS}} = \max\left[C_{\mathrm{SAS}_1}\rho\kappa S^2\left(\frac{L}{L_{vK}}\right)^2 - C_{\mathrm{SAS}_2}\rho k \max\left(\frac{1}{\omega^2}\left(\frac{\partial\omega}{\partial x_j}\right)^2, \frac{1}{k^2}\left(\frac{\partial k}{\partial x_j}\right)^2\right), 0\right]. \tag{6}$$

This formulation includes the von-Kármán length scale as

$$L_{vK} = \kappa \frac{\sqrt{2S_{ij}S_{ij}}}{|\overline{u}''|} \quad \text{with} \quad |\overline{u}''| = \sqrt{\left(\sum_i \frac{\partial^2 \overline{u}_i}{\partial x_j^2}\right)^2}. \tag{7}$$

The resulting unusual scale resolving behavior for an URANS model was analyzed in detail by Schafer et al. [14].

2.1 Model verification, evaluation and validation for engine applications

Due to the typically grid-dependent filtering in scale-resolving methods, completely separating the effects of numerics and model is extremely challenging and the same applies to hybrid methods. Thus, the hybrid DES-SST approach for engines was systematically verified and validated in [15, 16, 17]. In the following, some selected results of this work will be discussed.

In the work of Hasse et al. [16], the hybrid DES-SST modeling approach described in the previous section was verified using a series of simple test cases and compared with the results of the scale-resolving Smagorinsky model. First, the model constant C_{DES} for linking the grid size and the length scale was calibrated using the generic test case of decaying homogeneous isotropic turbulence (HIT), a test case in which the hybrid model operates completely in SRS mode. The result obtained for the constant $C_{DES}^{k\text{-}\varepsilon} = 0.61$ is in agreement with the results obtained by Travin et al. [9]. Therefore, the same constant was chosen as proposed by Travin et al. [9] for the k-ω branch: $C_{DES}^{k\text{-}\omega} = 0.78$.

The model was evaluated with the selected set of model constants using two different test cases: the flow along a backwards-facing step and vortex shedding past a triangle flameholder. Both cases serve as generic test cases and occur in a similar form in different regions during the intake stroke of a combustion engine. It was shown that the DES-SST model achieved a significantly better agreement with the experimental data compared to a conventional URANS approach. A final analysis of the anisotropy shows that the resolved Reynolds stresses cover nearly the entire anisotropy map.

In a more demanding test case, the DES-SST model was applied to a simplified engine setup (Hasse et al. [15]). The test case measured by Borée et al. [18] is characterized by a rectangular compression chamber with a slit-shaped inlet. The tumble motion in the compression chamber, which is formed during the intake stroke, is similar to that in an internal combustion engine. This tumble motion is one of the key characteristics of turbocharged DISI engines and is significantly influenced by cycle-to-cycle variations. For this reason, the experiment was selected to investigate the feasibility of hybrid URANS/LES models for the investigation of cycle-to-cycle variations in combustion engines.

The hybrid model approach allows the use of a scale-resolved LES model in regions with a reasonably high resolution, such as the inner part of the domain, and an URANS SST approach near the wall where the grid is not sufficiently resolved for a LES. It has been shown that the hybrid model is capable of resolving 80-90% of the turbulent kinetic energy. A comparison of the cycle-averaged velocities shows good agreement with the experimental data for both the DES and the URANS simulation. The scale-resolving simulation was capable of reproducing peaks of turbulent kinetic energy not only in regions of the intake jet, but also near the tumble center. Borée et al. [18] were able to clearly assign this effect to a large-scale displacement of the tumble center, which is a direct consequence of cyclic fluctuations.

In the next step, the DES-SST model was applied to a realistic engine geometry [17]. In this context, preliminary investigations with moving meshes and grid-to-grid interpolations were also carried out evaluating the solver's suitability. Compatibility with these methods is a mandatory requirement for a DES model so that it can be used over a complete engine cycle with accompanied compression and expansion of the control volume. It was shown that both effects can be neglected if the grid resolution is sufficiently fine.

A statistically stationary cylinder inflow was chosen as a first test case. For comparison, time-averaged optical velocity measurements and a RANS simulation were performed. Both DES and RANS simulation achieved reasonable agreement with the measured averaged velocity fields. A further analysis of the instantaneous velocity fields of the DES gives an impression of the highly transient flow field. No clear shedding frequency can be assigned to the observed fluctuations. The results suggest that the fluctuating flow field must have a significant influence on the resulting in-cylinder flow.

Finally, the DES-SST model was tested using a full engine cycle. For this purpose, a total of 13 consecutive cycles of an optically accessible engine were simulated. Instantaneous and averaged velocity fields provided satisfactory agreement with the experimental data. A comparison of the fluctuations occurring in the experiment and simulation shows RMS values of similar magnitude. Nevertheless, different flow structures occur in the averaged field. This may indicate that the number of simulated cycles is still too small compared to the experiment. An examination of the cyclical fluctuations in the area of the spark plug suggests that there is a considerable influence on the combustion taking place in the engine.

In summary, the outlined results show great potential for the application of hybrid URANS/LES approaches for engine application.

3 Selected engine studies

Some selected examples of the use of hybrid LES/URANS for engine simulations are presented. We start with investigations in non-moving geometries, then successively increase the degree of complexity. As mentioned above, the results are taken from contributions originating from the author's own group. Thus, this is not meant to be a comprehensive overview. Relevant studies from other groups can, for instance, be found from the references given in the corresponding papers.

3.1 Investigation of the intake flow

A flowbench is a stationary setup including the intake valves of an internal combustion engine. Buhl and Hartmann et al. [19, 20] performed several scale-resolving simulations of the flowbench to investigate the valve inlet flow and characterize engine-relevant features. Due to the high impact of turbulence on the phenomena occurring, various scale-resolving methods were used for modeling. Figure (2) illustrates the calculated time-averaged velocity fields for a DES-SST and a Sigma turbulence model.

With regard to the time-averaged velocity magnitude, only small differences can be identified. When comparing

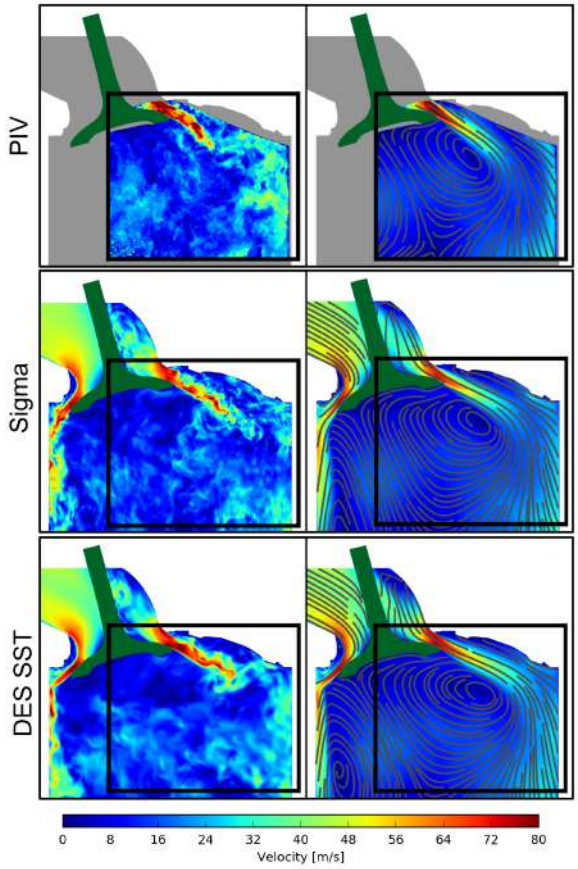

Figure 2: Instantanous (left) and time-averaged velocity magnitude obtained by PIV, Sigma and DES-SST model [19]

the DES-SST results with accompanying PIV measurements, the biggest differences can be seen in the recirculation zone behind the valve. For both turbulence models, the jet is seen to tilt upwards towards the cylinder head. Buhl et al [19] studied this observation in detail. Figure (3) depicts an approximation of the centerline of the intake jet for different turbulence models and grid resolutions. Both the Sigma and the DES-SST model show similar deviations from the experimental data. It can be shown that by increasing the grid resolution, a better approximation of the intake jet when comparing with the experimental data can be achieved.

The results obtained with the DES-SST model were used further to investigate the boundary layer upwards of the intake valve. Hartmann et al. [20] showed that none of the evaluated positions were in conformity with the analytic formulation of a fully turbulent boundary layer. This confirms that there are potential inaccuracies when using a logarithmic wall function.

Finally, an analysis was carried out of how potential vortex shedding at the valve stem influences jet fluctuation. A common frequency of 2860 Hz was identified, which indicates that the vortices generated upstream of the valve gap can influence the flow field in the combustion chamber downstream and thus trigger cyclic variations in an operating engine.

3.2 Investigation of in-cylinder tumble

In the first study presented, Buhl et al. [8] examined the applicability of hybrid LES/URANS models for the investigation of tumble formation. Several LES and hybrid URANS/LES models were applied to an simplified

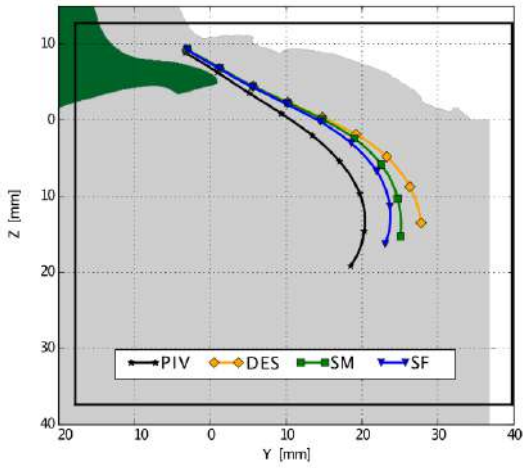

Figure 3: Jet centerline obtained by simulations and PIV based on the time-averaged velocity field in the valve center plane. DES identifies the DES-SST model with medium grid resolution. SM and SF denotes the LES-Sigma model with medium (SM) and fine (SF) grid resolutions, respectively [19]

engine setup. The setup is characterized by a cylindrical combustion chamber with a moving piston and a single non-moving valve concentric to the cylinder liner. This test case is known as a benchmark for IC engine flows for which experimental results [21], LES studies [22, 23, 24] and even DNS studies [25, 26, 27] are available.

Due to the piston movement the influence of cyclic variability on tumble formation can be observed in this engine. Slightly different results were achieved between full LES and hybrid models. Figure (4) illustrates a comparison where the Sigma model represents the full LES approach and the SAS-SST model a hybrid approach. While the average tumble position differs, a similar cyclic variability can be achieved. The average distance between the averaged and instantaneous tumble center for all investigated turbulence models is depicted in Figure (5). Apart from minor deviations, all models examined show similar variabilities along the engine cycle.

Higher engine speeds and therefore higher (local) Reynolds numbers can lead to very small Kolmogorov scales locally, and a sufficient spatial and temporal resolution might not be guaranteed within the entire domain. For these cases, the underlying URANS approach in the investigated hybrid DES-SST and SAS-SST model offers a reasonable backup means of describing the fluid flow.

A second study was performed with a more realistic engine setup by Buhl et al. [28]. Here, the tumble formation and interaction with the piston surface was investigated using a series-production state-of-the-art gasoline cylinder head with an actuated intake valve and flat piston.

The tumble center was detected based on an algorithm developed by Gravtieaux [29] which was extended to cover 3D data fields. In total, the temporal development of the tumble structure was analyzed for 15 individual engine cycles. From the beginning of the tumble formation, significant cycle-to-cycle variations in the tumble center were identified, as shown in Figure (6). When the chamber volume expands, the piston drags the middle section of the tumble center downwards, which leads to a considerable deformation. After reaching the bottom dead center, the tumble starts to reform and moves towards the cylinder head. Due to the stretching and compression of the tumble, strong interaction with the piston boundary

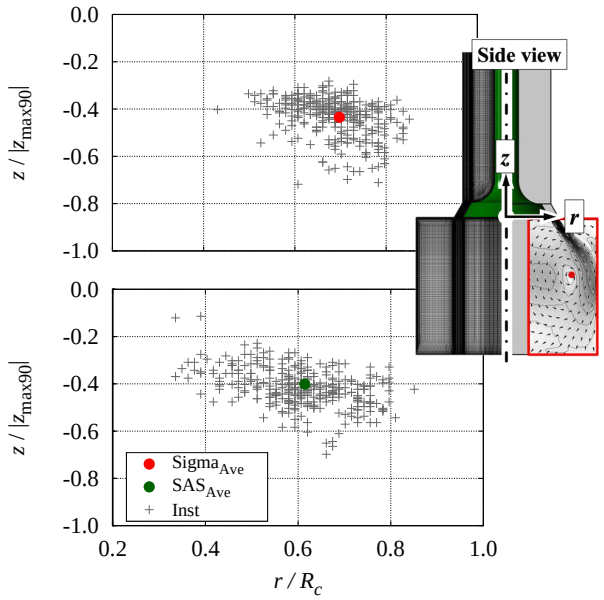

Figure 4: Phase-averaged and instantaneous tumble center positions for Sigma (left) and SAS (right) models at 90°CA [8]

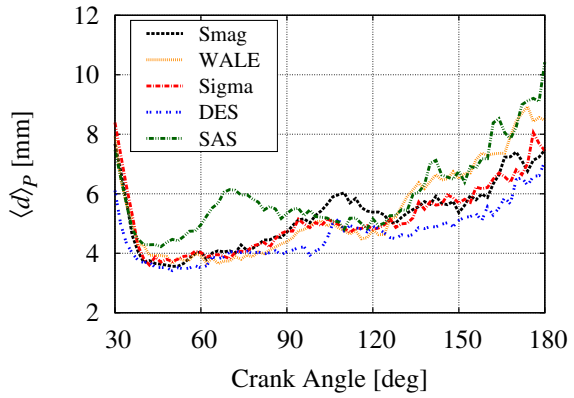

Figure 5: Average distance between the averaged and instantaneous tumble center for all investigated turbulence models [8]

layer can be expected. Therefore, a detailed investigation of the resolved boundary layer at the piston surface was carried out. Figure (7) shows a cross-section of the averaged velocity magnitude at the symmetry plane. The boundary layer is depicted by two isolines. The distance $z^+ = 5$ represents the viscous sublayer and the distance $z^+ = 30$ the logarithmic boundary layer. Tumble interaction results in an almost parallel flow in the regions P1 and P3, and a constantly thin boundary layer can be observed. P2 and P4 are in the region around the stagnation point. At these points, there is an increase in the boundary layer height.

The dimensionless piston boundary layer profiles for points P1-P4 are depicted in Figure (8). A comparison to the analytical log-law formulation (red dashed lines) shows that no turbulent equilibrium boundary layer exists at the piston surface. It is interesting to note that the results for P1 and P3 are in better alignment with the classical boundary layer assumption, while the profiles at P2 and P4 show larger discrepancies.

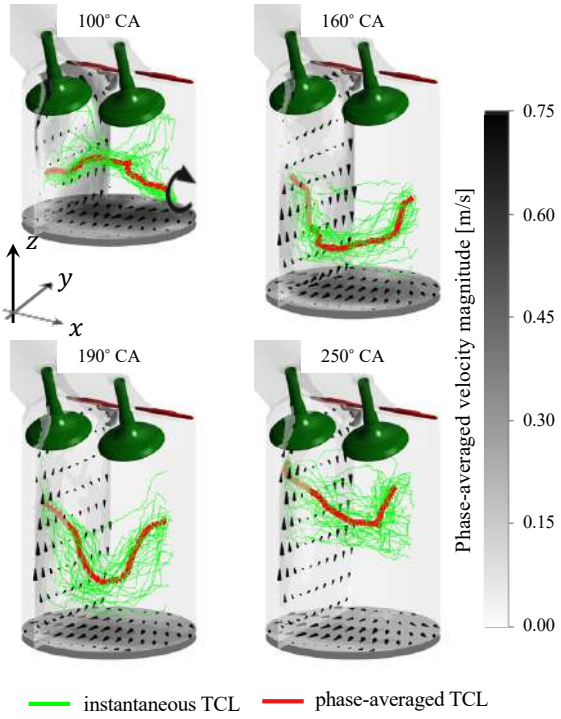

Figure 6: Phase-averaged (red line) and instantaneous (green line) tumble lines at different crank angles [28]

3.3 Investigations of cycle-to-cycle variations (CCVs)

In the work of Buhl et al. [22] an approach combining proper orthogonal decomposition (POD) and conditional averaging was used to develop a methodology to distinguish cycle-to-cycle variations (CCVs) from classical turbulent fluctuations.

For this purpose, a scale-resolving simulation of a simplified two-stroke engine was used to calculate 120 realizations of the intake phase. The resulting instantaneous velocity fields were grouped into different subsets. These subsets were determined by combining the first cycle-dependent POD modes. A large-scale fluctuation can then be determined from the difference between the subset average velocity magnitude and the ensemble average velocity magnitude, while small-scale fluctuations result from the difference between the instantaneous velocity magnitude and its specific subset average.

Due to the grouping of individual instantaneous cycles into several subsets, there is a reduction in the total number of realizations for every averaging process. This makes a significantly higher number of required engine cycles necessary for the analysis. With its good compromise between the grid requirements and scale resolution, the SAS-SST model proved to be particularly suitable for this analysis. It allowed the region of interest to be examined at a high resolution, while maintaining sufficient efficiency for calculating a necessary number of realizations.

In a subsequent study [30], the experience gained with the SAS-SST model was used to investigate CCVs in a well-established benchmark engine with a state-of-the-art cylinder head [31].

Altogether, 60 engine cycles under motored conditions were performed. Synthetic turbulence [32] was used to generate individual initial flow fields for each cycle.

The left side of Figure (9) illustrates the phase-averaged velocity magnitude on the valve middle plane

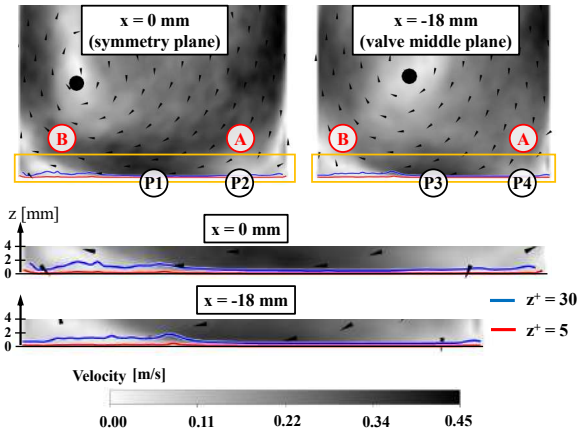

Figure 7: Velocity magnitude and orientation at 160° CA on the symmetry plane ($x = 0\,\mathrm{mm}$) and the valve middle plane ($-18\,\mathrm{mm}$) [28]

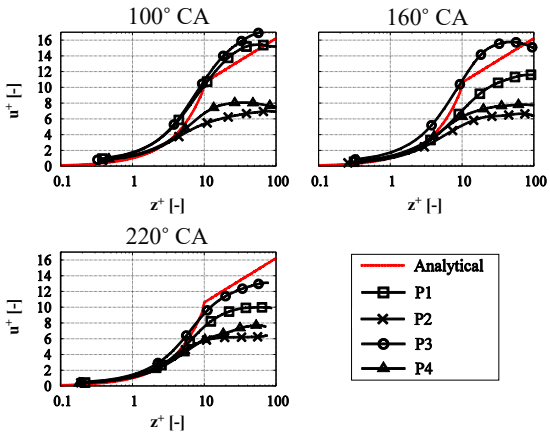

Figure 8: Phase-averaged dimensionless velocity profiles at P1-P4 at 100° CA, 160° CA and 220° CA [28]

at different engine crank angles. A well-defined intake jet can be observed at $-270°$ CA, caused by the inclination of the intake port and the separation edge upstream of the intake valve. The jet is deflected by the cylinder liner and the piston surface, which leads to a distinctive tumble structure. It can be clearly identified at $-180°$ CA and $-90°$ CA. The resolved turbulent structures are visualized by the Q criterion ($Q = 1 \times 10^5 s^{-2}$) and colored according to the viscosity ratio μ_t/μ (right side of Figure (9)). The number of resolved structures and the fact that μ_t/μ is at a typical level for scale-resolving simulations [33] confirm that the SAS-SST model is triggered into the scale-resolving mode.

Figure (10) illustrates the integral in-cylinder charge motion with respect to the x axis. It is quantified by the scalar quantity

$$\mathrm{Tu_x}(\varphi, n) = \frac{1}{2\pi\Omega} \frac{\int_{Cyl} \rho \left[(\mathrm{y} - \mathrm{y_c})\, w - (\mathrm{z} - \mathrm{z_c})\, v \right] dV}{\int_{Cyl} \rho \left[(\mathrm{y} - \mathrm{y_c})^2 + (\mathrm{z} - \mathrm{z_c})^2 \right] dV} \quad (8)$$

with Ω and $_{Cyl}$ as the engine speed and the in-cylinder volume, respectively. The center of the in-cylinder fluid mass is denoted by $\mathrm{y_c}$ and $\mathrm{z_c}$, while the sign of $\mathrm{Tu_x}$ represents the direction of rotation.

The intake phase with open intake valves takes place between $-325°$ CA and $-125°$ CA. In this phase, the dominant inlet jet causes the formation of a large-scale tumble. This is seen from the very high charge motion in the domain. The calculated fluctuations remain low

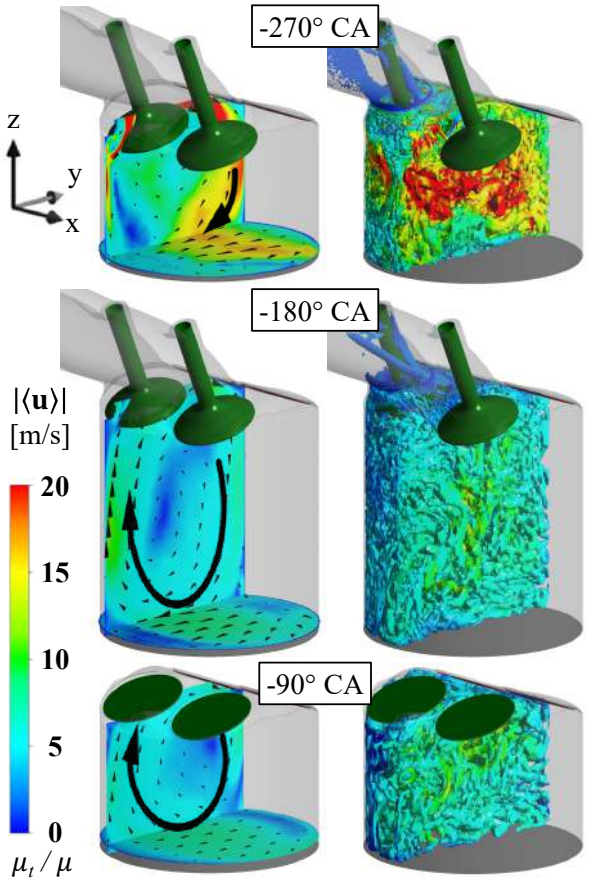

Figure 9: Left: phase-averaged velocity magnitude $|\langle u \rangle|$ on the valve middle plane and a plane 3 mm above the piston surface. Right: resolved turbulent structures ($Q = 1 \times 10^5 s^{-2}$; colored according to the viscosity ratio μ_t/μ). Please note that the same color scheme is applied for $|\langle u \rangle|$ and μ_t/μ [30]

during this phase. When the compression stroke is entered, a reduction in the motion can be obtained. At the same time, the variability between the instantaneous cycles increases. The opening of the exhaust valve during the expansion phase (105° CA) causes an inverted tumble which results in a positive value for $\langle \mathrm{Tu_x} \rangle$.

4 Future challenges and the need for further development efforts

Due to current technological developments such as downsizing, the increase in energy density or rigid environmental laws, a better understanding of the processes inside the engine is increasingly important. For this reason, hybrid URANS/LES methods in particular are drawing attention due to their comparatively low computing requirements. A comprehensive overview of future challenges and a suggestion for a systematic model development is given in [3]. Here, we briefly outline the main ideas.

Initial applications of such models in the context of engines showing promising results. Particularly, the understanding of the influence of CCVs on the charge motion was improved. To expand scale-resolving simulations to further engine-related topics, a continuous development and validation of these models is necessary. A recent survey among academic and industrial users [34] identified three major challenges for the future application of

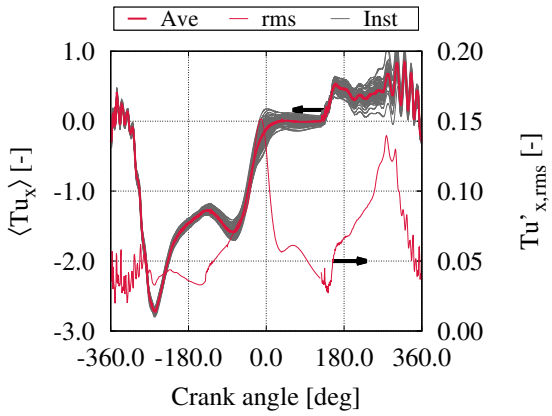

Figure 10: Phase-averaged and instantaneaous in-cylinder motion $\langle Tu_x \rangle$ obtained from individual cycles. In addition, the calculated fluctuation $Tu'_{x,rms}$ is depicted [30]

scale-resolving methods in engine development:

- Lack of validation data
- Transfer of sophisticated models
- Submodel development.

The first step towards further establishing scale-resolving methods in engine development requires the provision of reliable, complete validation data. The provision of mean and fluctuation velocities as well as key scalar quantities is especially relevant. Accompanying reference simulations can serve as "digital twins" and be used as a benchmark to point out deficits in existing models. One good example of appropriate validation experiments is the TUD engine database [31] (also part of the ERCOFTAC Knowledge Base https://kbwiki.ercoftac.org/). The optically accessible single-cylinder engine testbench was carefully designed to provide well-characterized boundary conditions and reproducible engine operations. The experimental results obtained are shared and discussed with accompanied simulation results in the framework of the "Darmstadt engine workshop". Despite the diverse range of models available in the scientific literature, so far mainly relatively simple models have found their way into the scale-resolving context. In the coming years it will be necessary to use suitable validation data to bring more sophisticated models from simpler test cases to the context of engines. In addition, the development of specially suited submodels in combination with SRS for engine-specific applications is also required. Here, the focus is particularly on current technological trends. Current environmental laws, for example, require an accurate description of the pollutant-forming processes inside the engine to achieve further reduction. Current downsizing and operating strategies also play a role. The prediction of knock and detonation processes is crucial for extending the engine operation range, but also a more accurate description of spray formation in direct-injection systems and the consecutive mixture formation is gaining attention. For many of the listed phenomena, a multitude of models already exist in the URANS context. The extension of these models to cover scale-resolving methods promises not only an enormous boost for the understanding of the engine cause-and-effect chain but also the development of more efficient combustion engines.

First steps towards high-resolution validation and reference data have already been taken in recent years. This development goes hand in hand with technological leaps in information technology and optics and offers a better understanding of the entire system. One example is the use of hybrid models for spray simulations [35]. Another highly relevant example is the investigation of the piston boundary layer. In experiments by Renaud et al. [36], the piston boundary layer of a research engine was successfully resolved down to viscous sublayer using PIV/PTV. The work thus provides valuable information that can contribute to the further development of existing wall models. At the same time, several direct numerical simulations (DNSs) of engine-relevant flows have been carried out in recent years [26, 37]. Both experimental and numerical investigations can be used to evaluate, improve and validate hybrid models.

5 Conclusion

This article provided an overview of our group's experience in using the hybrid DES-SST and SAS-SST model for the simulation of engine-related topics. After presenting studies on the general feasibility in the context of engines, various specific engine examples were presented. It has been shown that its deployment for combustion engines is ideal due to their complex geometries and resulting flow phenomena. The scale-resolving behavior of the models were used to describe coherent turbulent structures and thus enable the simulation of cycle-to-cycle variations (CCVs). At the same time the transition to URANS methods near the wall allows to keep computational requirements at a reasonable level.

In addition to providing further validation data, it is now necessary to transfer engine-specific submodels to scale-resolving simulations in order to further promote their application in the context of engines. Future model developments should specifically target the near-wall flow and the interaction of hybrid models with sprays and chemical reactions.

Acknowledgments

The authors acknowledge all the colleagues and students who contributed to the presented studies. We would like to thank ANSYS for providing us with licenses via their Academic Partner Program. This work was supported by the Deutsche Forschungsgemeinschaft (DFG, German Research Foundation) - Projektnummer 237267381 - TRR 150.

References

[1] A. Scholtissek, S. Buhl, D. Hain, and C. Hasse, "Internal Combustion Engine - cause and effect chain," doi:10.6084/m9.figshare.5170480.v3, 2017.

[2] C. J. Rutland, "Large-eddy simulations for internal combustion engines - a review," *International Journal of Engine Research*, vol. 12, no. 5, pp. 421–451, 2011.

[3] C. Hasse, "Scale-resolving simulations in engine combustion process design based on a systematic approach for model development," *International Journal of Engine Research*, vol. 17, no. 1, pp. 44–62, 2015.

[4] W. Leudesdorff, T. Unger, J. Janicka, and C. Hasse, "Scale-resolving Simulations for Combustion Pro-

cess Development," *MTZ worldwide*, vol. 80, no. 2, pp. 62–67, 2019.

[5] J. Smagorinsky, "General Circulation Experiments with the Primitive Equations," *Monthly Weather Review*, vol. 91, no. 3, pp. 99–164, 1963.

[6] F. Nicoud and F. Ducros, "Subgrid-Scale Stress Modelling Based on the Square of the Velocity Gradient Tensor," *Flow, Turbulence and Combustion*, vol. 62, no. 3, pp. 183–200, 1999.

[7] F. Nicoud, H. B. Toda, O. Cabrit, S. Bose, and J. Lee, "Using singular values to build a subgrid-scale model for large eddy simulations," *Physics of Fluids*, vol. 23, no. 8, p. 085106, 2011.

[8] S. Buhl, F. Dietzsch, C. Buhl, and C. Hasse, "Comparative study of turbulence models for scale-resolving simulations of internal combustion engine flows," *Computers & Fluids*, vol. 156, pp. 66–80, 2017.

[9] A. Travin, M. Shur, M. Strelets, and P. R. Spalart, "Physical and Numerical Upgrades in the Detached-Eddy Simulation of Complex Turbulent Flows," in *Advances in LES of Complex Flows*, pp. 239–254, Kluwer Academic Publishers, 2002.

[10] F. Menter, "Zonal Two Equation k-w Turbulence Models For Aerodynamic Flows," in *23rd Fluid Dynamics, Plasmadynamics, and Lasers Conference*, (Reston, Virigina), American Institute of Aeronautics and Astronautics, 1993.

[11] F. R. Menter and Y. Egorov, "The Scale-Adaptive Simulation Method for Unsteady Turbulent Flow Predictions. Part 1: Theory and Model Description," *Flow, Turbulence and Combustion*, vol. 85, no. 1, pp. 113–138, 2010.

[12] Y. Egorov, F. R. Menter, R. Lechner, and D. Cokljat, "The Scale-Adaptive Simulation Method for Unsteady Turbulent Flow Predictions. Part 2: Application to Complex Flows," *Flow, Turbulence and Combustion*, vol. 85, no. 1, pp. 139–165, 2010.

[13] F. Menter and Y. Egorov, "A Scale Adaptive Simulation Model using Two-Equation Models," in *43rd AIAA Aerospace Sciences Meeting and Exhibit*, (Reston, Virigina), American Institute of Aeronautics and Astronautics, 2005.

[14] P. Schaefer, M. Gampert, J. H. Goebbert, L. Wang, and N. Peters, "Testing of Model Equations for the Mean Dissipation using Kolmogorov Flows," *Flow, Turbulence and Combustion*, vol. 85, no. 2, pp. 225–243, 2010.

[15] C. Hasse, V. Sohm, and B. Durst, "Detached eddy simulation of cyclic large scale fluctuations in a simplified engine setup," *International Journal of Heat and Fluid Flow*, vol. 30, no. 1, pp. 32–43, 2009.

[16] C. Hasse, V. Sohm, M. Wetzel, and B. Durst, "Hybrid URANS/LES Turbulence Simulation of Vortex Shedding Behind a Triangular Flameholder," *Flow, Turbulence and Combustion*, vol. 83, no. 1, pp. 1–20, 2009.

[17] C. Hasse, V. Sohm, and B. Durst, "Numerical investigation of cyclic variations in gasoline engines using a hybrid URANS/LES modeling approach," *Computers & Fluids*, vol. 39, no. 1, pp. 25–48, 2010.

[18] J. Boree, S. Maurel, and R. Bazile, "Disruption of a compressed vortex," *Physics of Fluids*, vol. 14, no. 7, p. 2543, 2002.

[19] S. Buhl, F. Hartmann, S. A. Kaiser, and C. Hasse, "Investigation of an IC Engine Intake Flow Based on Highly Resolved LES and PIV," *Oil & Gas Science and Technology - Revue d'IFP Energies nouvelles*, vol. 72, no. 3, p. 15, 2017.

[20] F. Hartmann, S. Buhl, F. Gleiss, P. Barth, M. Schild, S. A. Kaiser, and C. Hasse, "Spatially Resolved Experimental and Numerical Investigation of the Flow through the Intake Port of an Internal Combustion Engine," *Oil & Gas Science and Technology – Revue d'IFP Energies nouvelles*, vol. 71, no. 1, p. 2, 2016.

[21] A. Morse, J. H. Whitelaw, and M. Yianneskis, "Turbulent flow measurements by laser-doppler anemometry in motored piston-cylinder assemblies," *Journal of Fluids Engineering*, vol. 101, no. 2, pp. 208–216, 1979.

[22] S. Buhl, F. Hartmann, and C. Hasse, "Identification of Large-Scale Structure Fluctuations in IC Engines using POD-Based Conditional Averaging," *Oil & Gas Science and Technology - Revue d'IFP Energies nouvelles*, vol. 71, no. 1, p. 1, 2015.

[23] D. C. Haworth, "Large-Eddy Simulation of in-Cylinder Flows," *Oil & Gas Science and Technology*, vol. 54, no. 2, pp. 175–185, 1999.

[24] A. Montorfano, F. Piscaglia, M. Schmitt, Y. M. Wright, C. E. Frouzakis, A. G. Tomboulides, K. Boulouchos, and A. Onorati, "Comparison of Direct and Large Eddy Simulations of the Turbulent Flow in a Valve/Piston Assembly," *Flow, Turbulence and Combustion*, vol. 95, no. 2-3, pp. 461–480, 2015.

[25] M. Schmitt, C. E. Frouzakis, Y. M. Wright, A. G. Tomboulides, and K. Boulouchos, "Investigation of cycle-to-cycle variations in an engine-like geometry," *Physics of Fluids*, vol. 26, no. 12, p. 125104, 2014.

[26] M. Schmitt, C. E. Frouzakis, A. G. Tomboulides, Y. M. Wright, and K. Boulouchos, "Direct numerical simulation of multiple cycles in a valve/piston assembly," *Physics of Fluids*, vol. 26, no. 3, p. 035105, 2014.

[27] M. Schmitt, C. E. Frouzakis, A. G. Tomboulides, Y. M. Wright, and K. Boulouchos, "Direct numerical simulation of the effect of compression on the flow, temperature and composition under engine-like conditions," *Proceedings of the Combustion Institute*, vol. 35, no. 3, pp. 3069–3077, 2015.

[28] S. Buhl, F. Gleiss, M. Köhler, F. Hartmann, D. Messig, C. Brücker, and C. Hasse, "A Combined Numerical and Experimental Study of the 3D Tumble Structure and Piston Boundary Layer Development During the Intake Stroke of a Gasoline Engine," *Flow, Turbulence and Combustion*, vol. 98, no. 2, pp. 579–600, 2016.

[29] L. Graftieaux, M. Michard, and N. Grosjean, "Combining PIV, POD and vortex identification algorithms for the study of unsteady turbulent swirling flows," *Measurement Science and Technology*, vol. 12, no. 9, pp. 1422–1429, 2001.

[30] S. Buhl, D. Hain, F. Hartmann, and C. Hasse, "A comparative study of intake and exhaust port modeling strategies for scale-resolving engine simulations," *International Journal of Engine Research*, vol. 19, pp. 282–292, 2018.

[31] E. Baum, B. Peterson, B. Böhm, and A. Dreizler, "On The Validation of LES Applied to Internal Combustion Engine Flows: Part 1: Comprehensive Experimental Database," *Flow, Turbulence and Combustion*, vol. 92, no. 1-2, pp. 269–297, 2014.

[32] L. Davidson, "Using isotropic synthetic fluctuations as inlet boundary conditions for unsteady simulations," *Advances and Applications in Fluid Mechanics*, vol. 1, no. 1, pp. 1–35, 2007.

[33] O. Vermorel, S. Richard, O. Colin, C. Angelberger, A. Benkenida, and D. Veynante, "Towards the understanding of cyclic variability in a spark ignited engine using multi-cycle LES," *Combustion and Flame*, vol. 156, no. 8, pp. 1525–1541, 2009.

[34] C. Hasse and J. Janicka, "Towards Industrial LES of Engine Combustion," tech. rep., Forschungsvereinigung Verbrennungskraftmaschinen (FVV), 2017.

[35] V. K. Krastev and G. D. Ilio, "On the application of hybrid turbulence models for fuel spray simulation in modern internal combustion engines," in *Secon Internationl Conference on Material Science, Smart Structures and Applications: ICMSS-2019*, AIP Publishing, 2019.

[36] A. Renaud, C.-P. Ding, S. Jakirlic, A. Dreizler, and B. Böhm, "Experimental characterization of the velocity boundary layer in a motored IC engine," *International Journal of Heat and Fluid Flow*, vol. 71, pp. 366–377, 2018.

[37] G. Giannakopoulos, C. Frouzakis, K. Boulouchos, P. Fischer, and A. Tomboulides, "Direct numerical simulation of the flow in the intake pipe of an internal combustion engine," *International Journal of Heat and Fluid Flow*, vol. 68, pp. 257–268, 2017.

Morphing for Smart Wing Design Through RANS/LES Methods

A. Marouf[1,2], N. Simiriotis[1], J-B. Tô[1], J-F. Rouchon[3], Y. Hoarau[2] and M. Braza[1]

[1] *Institut de Mécanique des Fluides de Toulouse, CNRS/INPT UMR N 5502, Toulouse, France*
[2] *Université de Strasbourg/CNRS - ICUBE, Strasbourg 67000, France*
[3] *Laboratoire Plasma et Conversion d'énergie (LAPLACE), CNRS/INPT N5213, Toulouse, France*

Abstract

This article presents numerical simulation results obtained in the context of the H2020 European research project SMS, "Smart Morphing and Sensing for Aeronautical configurations" by using among other, hybrid RANS-LES methods, able to accompany the design of the wings of the future. The morphing concepts studied are partly bio-inspired and are able to act in multiple time and length scales. They are proven efficient for the increase of the aerodynamic performances of A320 wings in reduced scale and near scale one, in synergy with the prototypes built within this project. The simulations have shown the ability of novel electroactive actuators performing slight deformation of the trailing edge region and optimal vibrations, to create suitable vortex breakdown of specific coherent structures and to enhance beneficial vortices, leading to thinning of the shear layers and the wake's width. The simulations quantified the optimal actuation ranges and the gains in lift increase, drag reduction and simultaneous attenuation of the noise sources past the trailing edge.

1 Introduction

The present article highlights the contribution of RANS-LES methods in the future wing design by means of electroactive morphing developed in the currently running H2020 European research project "Smart Morphing and Sensing for aeronautical configurations[1]". This is a multi-disciplinary project that employs intelligent electroactive actuators modifying the lifting structure of an aircraft and allowing optimal shapes with respect to the aerodynamic performance (high lift and low drag). A closed-loop is accomplished for the controller design of the morphing wings in this project by using a new generation of pressure sensors using fiber optics-Bragg grating allowing distributed pressure measurements and in situ real-time optimization of the aerodynamic characteristics.

The coordinator's research institutes IMFT - Institut de Mécanique des Fluides de Toulouse and LAPLACE - Laboratoire Plasma et Conversion d'Energie, had studied since 2009 bio-inspired morphing wings thanks to electrically actuated materials able to deform and vibrate in different time and length scales, as dictated by the turbulence surrounding the wing and developed in its wake. These actuations operate in a similar way as the different classes of large hunting bird wings, winglets and feathers, able to simultaneously increase lift, decrease drag and reduce their noise when these birds hasten to the prey. By optimizing the fluid-structure interaction thanks to these novel actuators, harmful coherent vortices are attenuated by means of vortex breakdown and beneficial vortices are enhanced, producing a significant increase of the aerodynamic performance and decrease of the noise sources. The studies of the research team IMFT-LAPLACE created the *hybrid electroactive morphing* [1] by simultaneously actuating different classes of smart materials in low frequencies (order of 1 Hz) but high deformations (order of 15% of the chord's length) and higher frequencies (order of 500 Hz) but low deformations (order of 1% of the chord's length), like the wings and feathers of the birds respectively. A priority of the European aeronautical industries is to make the flight safer, cleaner, greener and quieter than ever before. The bio-inspired electroactive morphing provides lighter aerostructures with a much fast response than other hydromechanical actuators and different MEMS concepts of previous studies. A first set of bio-inspired morphing prototypes of the IMFT-LAPLACE team were part of the Royal Society Annual Exhibition in 2014 in the stand: "Smart wing design through turbulence control Science imitating Nature[2]", in collaboration with Imperial College[3].

Electroactive morphing wing prototypes of A320 have been studied by the research team IMFT-LAPLACE in collaboration with AIRBUS "Emerging Technologies and Concepts Toulouse" and in the context of the SMS project, in the subsonic wind tunnels of IMFT in reduced scale (chord of 70 cm) and near scale one (wing chord of 2.40m and high-lift flap chord of 1m), by means of Time-Resolved PIV (TRPIV), forces and pressure measurements. Following our previous studies, dynamic camber systems using Shape Memory Alloys (SMA) for low frequency-high deformation [2] and higher-frequency-low deformation trailing edge vibrations [3] by means of piezo-actuators, a new type of an A320 morphing wing was constructed, offering a simultaneous actuation at different time and length scales [4]. This prototype explored the effects of both, low frequency-high deformation by using the SMA actuators together with piezo-electric actuators of Macro-Fiber-Composite (MFC) type. By using the piezo-actuators only, a lift increase of 2 % and drag reduction of 3 % have been obtained, where by simultaneous actuation of the SMA and piezos, a lift increase of order 10 % and a drag reduction of 5% have been reached, with simultaneous reduction of the noise sources of order 20 dB, corresponding to the coherent eddies shed past the trailing edge. The experiments and

[1] www.smartwing.org/SM/EU

[2] http://www.cnrs.fr/insis/recherche/actualites/2014/morphing.htm

[3] https://www.youtube.com/watch?v=AoAaCCvn38M

simulations were accomplished at Reynolds numbers of 500,000 and 1 Million.

The numerical studies in the SMS project, [5] examined the morphing efficiency obtained by trailing-edge low deformation (order of 1-3 mm) and higher frequency vibration (order of 400 Hz) at Reynolds number of 1 Million. The turbulence modelling approach OES, Organised Eddy Simulation, [6], [7], [8] has been used, in which the resolved turbulence contains the coherent structures and the modelled turbulence contains the chaotic turbulent motion. This approach had been proven efficient for the coherent structures development and the related instabilities, even in two-dimensional approach. The numerical results have shown that the morphing produces improved aerodynamic performances and reduces the amplitude of instability modes associated to aerodynamic noise. In the context of the SMS project, The optimal frequency and amplitude of the actuations obtained by the present numerical study are in use for the closed-loop for the optimal manipulation of the embedded actuators, able to cut-off the harmful instabilities at their birth, thus showing the strong synergy between the numerical simulations and the experimental studies for the design in the SMS project.

Beyond the bio-inspired context, it is worthwhile noticing that the birds do not fly at transonic speeds corresponding to the cruise phase of a real aircraft. In these regimes, the numerical approach has proven essential for the design, prior to the experiments under way within the SMS project for this regime. In [9] we investigated the electroactive morphing for an A320 type of wing in transonic regime (Mach number of 0.78, Reynolds number of order 3 Million), with the same turbulence modelling method as previously mentioned. The study revealed that a deformation with a slight upwards deflection of the trailing-edge by 2 degrees associated with a trailing-edge vibration of 300 Hz is able to attenuate the buffet instability and to enhance the life-to-drag of order 6%. This is due to the feedback effects created from the trailing edge and the wake area towards the SWBLI (Shock Wave Boundary Layer Interaction) region, produced by an eddy-blocking within the shear layers, by means of the trailing-edge vibration. This mechanism is similar to a shear sheltering one as in [10].

Frequency (Hz)	300	350	400	450	500	700
$\frac{\langle C_l/C_d\rangle - \langle C_l/C_d\rangle_{static}}{\langle C_l/C_d\rangle_{static}} \times 100$	+2.4%	+5.5%	-2.5%	-5.5%	-5.5%	+5.9%
Frequency (Hz)	720	750	800	1000	1500	
$\frac{\langle C_l/C_d\rangle - \langle C_l/C_d\rangle_{static}}{\langle C_l/C_d\rangle_{static}} \times 100$	+1.6%	+6.1%	+6%	+3.5%	+5.8%	

Table 1: Relative gain (or loss if negative) of the averaged lift-to-drag ratio for different piezo-actuation frequencies compared to the static (non morphing) case

Frequency (Hz)	300	350	400	450	500	700
$\frac{\langle C_d\rangle - \langle C_d\rangle_{static}}{\langle C_d\rangle_{static}} \times 100$	-3.5%	-8.9%	+6.1%	+12.3%	+11.9%	-9.1%
Frequency (Hz)	720	750	800	1000	1500	
$\frac{\langle C_d\rangle - \langle C_d\rangle_{static}}{\langle C_d\rangle_{static}} \times 100$	-1.2%	-9.8%	-9.6%	-4.1%	-9.1%	

Table 2: Relative gain (if negative in respect of drag reduction) or loss (if positive) of the averaged drag coefficient for different piezo-actuation frequencies comparing to the static case

Our current numerical simulations in the SMS project concerning the transonic Reduced Scale (tRS) morphing prototype of an A320 wing have determined the optimal frequency ranges able to considerably increase the aerodynamic performance presented in table 1 and 2. to

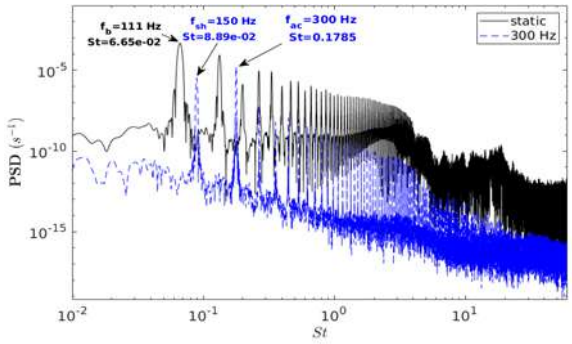

Figure 1: Attenuation of the buffet frequency f_b due to actuation and slight deformation of the trailing edge region in cruise phase, Mach=0.78, Re= 2.06 x 10^6. PSD of lift coefficient, transonic morphing prototype of A320 type

decrease the buffet amplitude as well as the overall PSD level related to the noise. This results to a constriction of the shear layers and to an attenuation of the predominant frequencies of the shear-layers vortices as shown in figure 1. These numerical simulations are in strong synergy and contribute to the experimental studies carried out in the SMS project concerning the design of the morphing prototype in cruise phase.

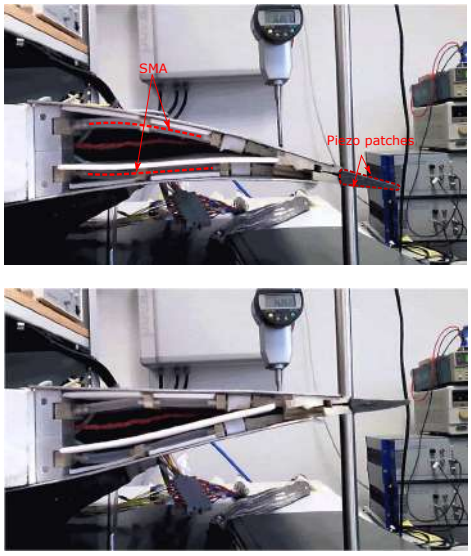

Figure 2: Reduced-Scale prototype using Shape Memory Alloys (SMA)

Figure 3: Series of piezo-electric patches installed in the wing's trailing-edge

Furthermore, the numerical studies in the SMS project include low subsonic regime simulations for the morphing wing design concerning the take-off and landing phases. In this context, the Reduced-Scale (RS) A320 prototype is considered having a chord of 70 cm and consists of a single element wing operating in clean position (at angle of attack of 10 degrees), instrumented by Shape Memory Alloys (figure 2). This design ensures high-amplitude deformations (order of 10 cm) downwards in camber control and low frequency actuation (order of 1Hz) . Moreover, piezo-electric patches allow for higher frequency actuation of order 500 Hz) and low deformations of order 1-3 mm (figure 3). In addition, numerical simulations are carried out for the Large-Scale (LS) prototype of the SMS project, having a total chord of 2.40 m and a flap's chord of 1m, (figure 4) with morphing high-lift flap near scale one, in a two-element configuration of the A320 wing operating at the take-off position. These simulations accompany the design and the experiments concerning this prototype.

Figure 4: Morphing high-lift LS prototype of the A320 wing near scale 1 in the S1 wind tunnel of IMFT

2 Numerical methods and turbulence modelling

The NSMB code [11, 12, 13] is used to perform CFD and CFDSM (Computational Fluid Dynamics - Structural Mechanics) simulations in the SMS project. The code solves unsteady and steady compressible Navier-Stokes equations using the finite volume method, a structured grid is used to simulate the flow around single and two-element wing-flap. This code includes a variety of efficient high-order numerical schemes and turbulence modelling closures in the context of URANS, LES and hybrid turbulence modelling. In the present study, the fourth-order central scheme and second order dual-time stepping for the temporal discretisation are selected. Artificial compressibility preconditioning was used to simulate the flow in a subsonic speed range for both Reduced and Large-Scale configurations. The NSMB code includes efficient fluid structure coupling for moving and deformable structures. It is interfaced with specific structural modules taking into account the prototype's deformation according to different actuations and interfaced with the CFD part of the code. The mesh movement and deformation is carried out by means of the ALE (Arbitrary Lagrangian-Eulerian) method. The Organised Eddy Simulation OES [7] and the hybrid Delayed Detached Eddy Simulation DDES-OES [14] with embedded OES approach in the statistical part of the DDES were selected to simulate the flow for both configurations. The design of the DDES grid around the wing requires a homogeneous local grid cells with $\Delta x \approx \Delta y \approx \Delta z$ following the recommendations in [15].

3 Results and discussion

3.1 Reduced Scale prototype

This part of the study focuses on the Reduced-Scale in clean configuration with a chord of 0.7 m at a Re = 10^6 and angle of attack 10° . Using the DDES-OES, the homogeneous ambient terms are activated as in [16]. The grid used for the Reduced Scale prototype contain 10 million cells for the OES model and 60 million cells for the DDES-OES model with a minimum local cell size less than 1 mm. A span of 0.8C (40 cells in the span direction; C being the chord) is used for the OES model. In the DDES-OES, a span dimension of 0.3C (120 cells in the span direction) is selected as presented in the figure 6. The grids were created to respect the dimensions of the IMFT S4 wind tunnel in the vertical to the chord dimension. The streamwise numerical dimension from the inlet to the outlet is 11C and the wing is placed in the middle. Two-dimensional and three-dimensional simulations are carried out for the Reduced and the Large Scale prototypes.

A detailed parametric study has been accomplished in 2D in order to detect the optimal ranges whereas the 3D study has been performed for selected parameters only. Beyond the comparisons with the TRPIV [5], the numerical simulations are used to focus the experiments in the optimal actuation ranges.

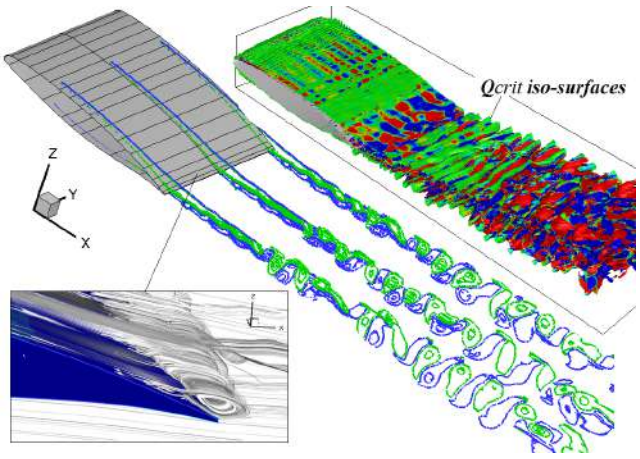

Figure 5: Presentation of the wake turbulent structures and near trailing-edge separation (recirculation) by means of the OES model

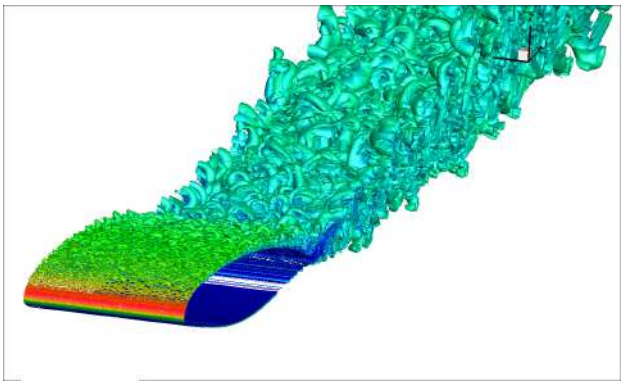

Figure 6: Q criterion (1500) colored by the velocity magnitude using the OES-DDES model

Figures 5 and 6 illustrate the flow behaviour around the RS prototype in static (non morphing) configuration

and provide the near-trailing edge overview of the boundary layer detachment inducing a recirculation vortex due to the angle of attack. The separation creates a higher velocity gradient between the upper and the lower shear layers giving birth to the wake instabilities. In addition, the secondary instability appearing as a three-dimensional undulation of the coherent vortex structures according to well distinct wavelengths is highlighted by means of the Q criterion and related to the amplification of the spanwise velocity.

The spanwise velocity in the z direction has been

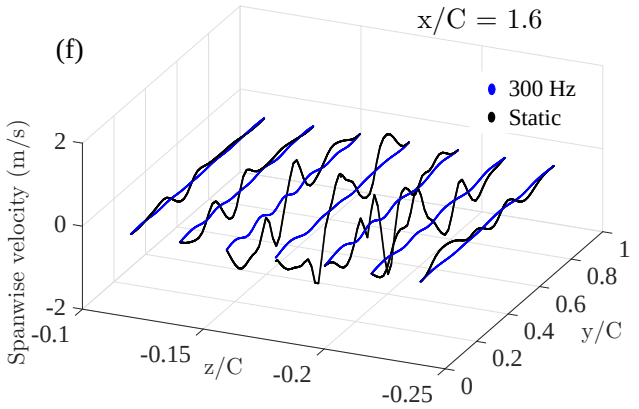

Figure 7: Extracted spanwise velocity through a vertical plane z/C a long the span direction y/C

extracted from different horizontal lines according to the vertical direction z in figure 7. A considerable attenuation of this is obtained, illustrating a practical suppression of the three-dimensionnality. This is due to the actuation frequency by 300 Hz obtained by the piezo-patches operating monochromatically along the span in the trailing-edge region. This actuation modifies the direction of the mean shear of the von Kármán vortices, leading to a subcritical elliptic instability shape of these coherent vortices, thus attenuating the secondary instability spanwisely [17]. Consequently, the wake thickness is thinner compared to the static case (no vibration).

3.2 Large-Scale prototype

In the context of the SMS European project, the Large-Scale (LS) prototype of a morphing A320 high-lift configuration including the wing-flap two-element system was studied in accordance with the IMFT S1 wind tunnel configuration, [18], [19]. The morphing effects for the Large Scale prototype.

A subsonic regime at a Mach number $M = 0.032$ and Reynolds number of $Re = 2.25$ million is selected and an angle of attack for the fixed wing of $\alpha = 8.2°$ which corresponds to the range of angles in the take-off position. A flap's deflection angle of $\delta = 10°$ degrees is selected. 2D and 3D simulations have been performed for the static case, taken as reference to compare with the morphing case. The vibration frequencies vary in the range of 60 to 400 Hz with a fixed vertical actuation amplitude of 0.7 mm.

An optimal frequency range in respect of the aerodynamic performance increase is found near 300 Hz. The coherent structures corresponding to low frequency instabilities are von Kármán vortices interacting with anti-clockwise vortices generated from the actuation of the

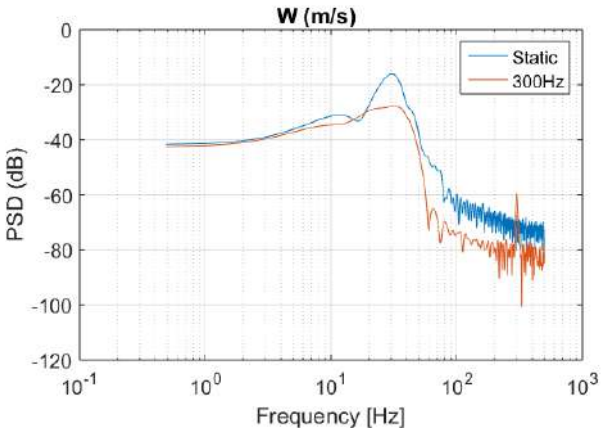

Figure 8: Power Spectral Density of the vertical velocity component at $x/C = 1.47$, $z/C = 0.04$

flap's trailing-edge. These vortices break down the existing von Kármán eddies and lead to a wake thinning. Furthermore, smaller-scale vortices are generated from the trailing edge actuation, that propagate in the wake and produce a shear-sheltering effect as in [8]. This results to a constriction of the shear layers and to an attenuation of the predominant frequencies of the shear-layers vortices as shown in Figure 8. Regarding the aerodynamic coefficient, the drag is decreased and an enhancement of the lift is noticed.

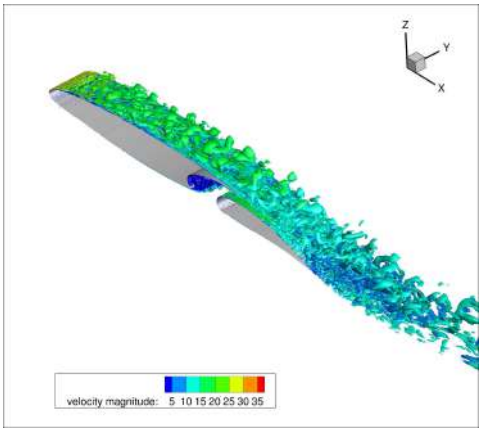

Figure 9: Q criterion (1000) colored by the velocity magnitude for the Large-Scale prototype at the take-off position using the OES-DDES turbulence model

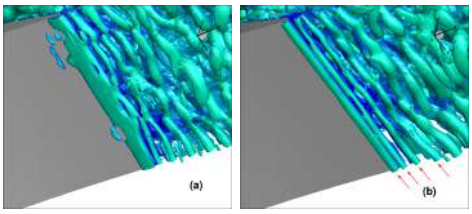

Figure 10: LS prototype, Re= 2.25 Million, take-off configuration.Overview of the bottom surface near trailing-edge region . Left: Static, illustrating coherent vortex rows with vortex dislocations; right: morphing with 300 Hz vibration and slight trailing-edge deformation: attenuation of the vortex dislocations and of the three-dimensional effects in the morphing configuration

Figure 9 illustrates the Q criterion using the DDES-OES in [20]. A breakdown of the vortex rows and ap-

pearance of the three-dimensional structures in the wake is related to the high Reynolds number and the angle of attack. Vortex dislocations of the primary von Kármán vortex rows are formed in the spanwise direction, illustrated by a junction of the "spinal column" (of two adjacent vortex rows [17]), in the spanwise direction in figure 10. It is found that an actuation at 300 Hz and amplitude of 0.7mm suppresses the vortex dislocations by generating anticlockwise vortex rows, resulting to a considerable wake thinning in figure 11.

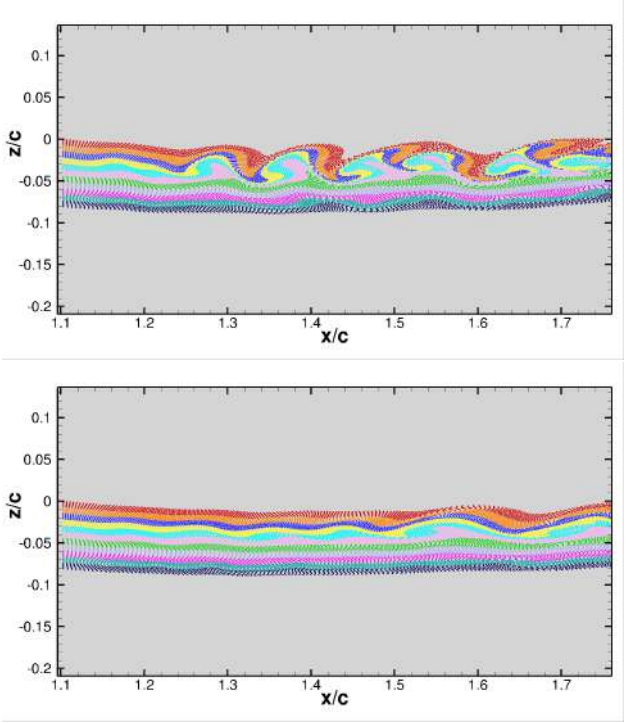

Figure 11: Streaklines illustrating the morphing effect: Top: static. Bottom: morphing with piezoactuators vibrating at 300 Hz with slight trailing-edge deformation showing the vortex breakdown of the coherent structures and the shear layers and wake thinning

Figure 12 shows comparison of the mean lift coefficient in both static and morphing configurations. The CL varies as a function of the frequency in the range of (60 Hz - 300 Hz) and the amplitude actuation in a range of (0.5mm - 1.5mm) and is found increased in all morphing configurations.

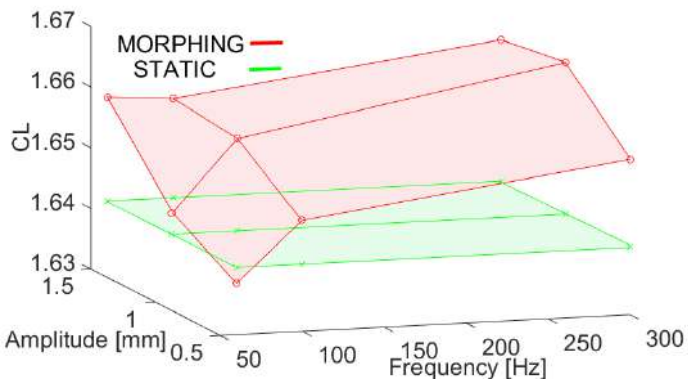

Figure 12: Mean lift coefficient at the take-off position as a function of different actuation frequencies and amplitudes compared to the static case

4 Conclusion

This study provides discussion based on numerical results obtained in the case of two main morphing configurations of an A320 wing in the context of the H2020 NÂř 723402 European project "Smart Morphing and Sensing for aeronautical configurations" coordinated by IMFT - Institut de Mécanique des Fluides de Toulouse. A single element configuration corresponding to the Reduced-Scale (RS) morphing prototype and a high-lift configuration with two-element wing-flap in take-off position corresponding to the Large-Scale (LS) prototype (near scale one) of this project are considered. In the present numerical study, the morphing is imposed in the near-trailing edge region as a slight deformation and vibration in frequency ranges (50 - 400) Hz. The simulations with high camber effects concern another part of our studies, not presented in this article. The turbulence modelling approaches OES (Organised Eddy Simulation) and the hybrid DDES-OES (Delayed Detached Eddy Simulation with embedded OES in its statistical part) have been used. It has been shown that an actuation at 300 Hz produces suitable vortex breakdown, leading to shear layer and wake thinning, as well as to an attenuation of three-dimensionality. These facts lead to a considerable increase of the aerodynamic performances for both morphing configurations of the RS and LS prototypes and attenuate the aerodynamic noise sources corresponding to the predominant frequencies generated by the coherent structures development. These benefits are produced thanks to the wake thinning through a breakdown of the coherent structures in the wake, by optimal manipulation of the turbulence structures near the trailing edge and the wake regions. The turbulence modelling approaches including Hybrid RANS/LES methods contributed to this relevant performance and accompanied the prototypes design realised in the SMS project.

Acknowledgement

This study is a contribution of N. Simiriotis, A. Marouf, J.B. Tô, Y. Bmegaptche Tekap, N. Bhardwaj, Y. Hoarau, J. Scheler, D. Harribey, C. Nadal, J.F. Rouchon. Our thanks are expressed to the IMFT services: "Signaux - Images" (S. Cazin, M. Marchall) for the PIV acquisitions, COSINUS team, (P. Elyakime) for the parallel post-processing of the experimental data and the Technical Constructions Service, "Atelier" of IMFT (R. Soeparno and his team), as well as to the Techical Services of the LAPLACE Laboratory in ENSEEIHT (Ecole Nationale Supérieure d'Electrotechnique, Electronique, Hydraulique et Télécommunications). This work was supported by the STAE Foundation "Sciences et Technologies pour l'aéronautique et l'Espace, http://www.fondation-stae.net/, the European Commission funding of the project H2020 $N°$ 723402 Smart Morphing and Sensing for aeronautical configurations, www.smartwing.org/SMS/EU, the AIRBUS - ETCT (Emerging Technologies and Concepts Toulouse) project PJOR D14012929, the DGA, "Direction Générale de l'Armement", for having providing the PhD fellowship of J. Scheller and N. Simiriotis, l'ENS - "Ecole Normale Supérieure of Rennes" for the PhD fellowship of G. Jodin and the French Ministry of Education and Research for having provided the PhD fellowship of A. Marouf. The authors are grateful to the French Supercomputing Centres CALMIP, CINES, IDRIS and TGCC-CEA for the Computer allocation, as well as to the PRACE Super-

computing allocation N° 2017174208 of the PRACE-FWING project, which provided the SMS project simulations with 15 million CPU hours in the TGCC-CEA Supercomputing Centre.

References

[1] Johannes Scheller. *Electroactive morphing for the aerodynamic performance improvement of next generation airvehicles*. PhD thesis, 2015.

[2] M. Chinaud, J.F. Rouchon, E. Duhayon, J. Scheller, S. Cazin, M. Marchal, and M. Braza. Trailing-edge dynamics and morphing of a deformable flat plate at high Reynolds number by time-resolved PIV. *Journal of Fluids and Structures*, 47:41 – 54, 2014.

[3] J. Scheller, M. Chinaud, JF. Rouchon, E. Duhayon, S. Cazin, M. Marchal, and M. Braza. Trailing-edge dynamics of a morphing NACA0012 aileron at high Reynolds number by high-speed PIV. *Journal of Fluids and Structures*, 55:42 – 51, 2015.

[4] G. Jodin, V. Motta, J. Scheller, E. Duhayon, C. DÃűll, J.F. Rouchon, and M. Braza. Dynamics of a hybrid morphing wing with active open loop vibrating trailing edge by time-resolved PIV and force measures. *Journal of Fluids and Structures*, 74:263 – 290, 2017.

[5] N. Simiriotis, G. Jodin, A. Marouf, P. Elyakime, Y. Hoarau, J.C.R. Hunt, J.F. Rouchon, and M. Braza. Morphing of a supercritical wing by means of trailing edge deformation and vibration at high Reynolds numbers: experimental and numerical investigation. *Journal of Fluids and Structures*, 2019.

[6] M. Braza, R. Perrin, and Y. Hoarau. Turbulence Properties in the cylinder wake at high Reynolds number. *Journal of Fluids and Structures*, 22:757 – 771, 2006.

[7] R. Bourguet, M. Braza, G. Harran, and R. El Akoury. Anisotropic Organised Eddy Simulation for the prediction of non-equilibrium turbulent flows around bodies. *Journal of Fluids and Structures*, 24(8):1240–1251, 2008.

[8] D. Szubert, F. Grossi, A. J. Garcia, Y. Hoarau, J. C. R. Hunt, and M. Braza. Shock-vortex shear-layer interaction in the transonic flow around a supercritical airfoil at high Reynolds number in buffet conditions. *Journal of Fluids and Structures*, 55:276–302, 2015.

[9] J.-B. Tô, N. Simiriotis, A. Marouf, D. Szubert, I. Asproulias, D.M. Zilli, Y. Hoarau, J.C.R. Hunt, and M. Braza. Effects of vibrating and deformed trailing edge of a morphing supercritical airfoil in transonic regime by numerical simulation at high Reynolds number. *Journal of Fluids and Structures*, 91, 2019.

[10] J.C.R. Hunt, I. Eames, and J. Westerweel. Vortical interactions with interfacial shear layers. In *In Kaneda, Y.(Ed.), IUTAM Symposium on Computational Physics and New Perspectives in Turbulence, IUTAM Bookseries, vol.4, Springer, Nagoya, Japan, pp.331-338*, 2008.

[11] Y. Hoarau, D. Pena, J. B. Vos, D. Charbonnier, A. Gehri, M. Braza, T. Deloze, and E. Laurendeau. Recent developments of the Navier Stokes Multi Block (NSMB) CFD solver. In *54th AIAA Aerospace Sciences Meeting*, 2016.

[12] J. Vos, A. Rizzi, A. Corjon, E. Chaput, and E. Soinne. Recent advances in aerodynamics inside the NSMB (Navier Stokes Multi Block) consortium. In *36th AIAA Aerospace Sciences Meeting and Exhibit*, 1998.

[13] Y. Hoarau. Analyse physique par simulation numérique et modélisation des écoulements décollés instationnaires autour de surfaces portantes, 2002.

[14] V. Shinde, T. Marcel, Y. Hoarau, T. Deloze, G. Harran, F. Baj, J. Cardolaccia, J.P. Magnaud, E. Longatte, and M. Braza. Numerical simulation of the fluid-structure interaction in a tube array under cross flow at moderate and high Reynolds number. *Journal of Fluids and Structures*, 47:99 – 113, 2014.

[15] Philippe R. Spalart. Detached-Eddy Simulation. *Annual Review of Fluid Mechanics*, 41(1):181–202, 2009.

[16] Philippe R. Spalart and Christopher L. Rumsey. Effective Inflow Conditions for Turbulence Models in Aerodynamic Calculations. *AIAA Journal*, 45(10):2544–2553, 2007.

[17] M. Braza, D. Faghani, and H Persillon. Successive stages and the role of natural vortex dislocations in three-dimensional wake transition. *J. Fluid Mech*, 439:1–41, 2001.

[18] A. Marouf, Y. Hoarau, J. B. Vos, D. Charbonnier, Y. Bmegaptche Tekap, and M. Braza. Evaluation of the aerodynamic performance increase thanks to a morphing A320 wing with high-lift flap by means of CFD Hi-Fi approaches. In . *In AIAA Aviation Forum, invited session of the SMS European project, Dallas, 17-21 June 2019*.

[19] A. Marouf, Y. Bmegaptche Tekap, N. Simiriotis, J. Tô, J. Rouchon, Y Hoarau, and M. Braza. Numerical investigation of frequency-amplitude effects of dynamic morphing for a high-lift configuration at high Reynolds number. *International Journal of Numerical Methods for Heat & Fluid Flow*, 2019.

[20] A. Marouf, N. Simiriotis, J.B. Tô, Y. Bmegaptche, Y. Hoarau, and M. Braza. DDES and OES Simulations of a Morphing Airbus A320 Wing and Flap in Different Scales at High Reynolds. In *Hoarau Y., Peng SH., Schwamborn D., Revell A., Mockett C. (eds) Progress in Hybrid RANS-LES Modelling. Notes on Numerical Fluid Mechanics and Multidisciplinary Design*, 2020.

Recent Studies on Instabilities and Transition of High-Speed Flows

S. Fu and Z. Xiao

Laboratory of Advanced Simulation of Turbulence (LAST)
School of Aerospace Engineering, Tsinghua University, Beijing 100084, China

Abstract

This article describes some of the recent progresses on RANS-LES hybrid models, as well as instability analysis, applied to a wide range of flows including hypersonic flow transition studies at the LAST, Tsinghua University. RANS-LES hybrid model is now improved to account for flow transition in addition to the alleviation of the grey area and flow control. In the stability analysis of high-speed flows, advanced global stability analysis technique had been developed to investigate flow instability of attachment line at high Mach numbers. Instability of flows with thermal-chemical non-equilibrium effects and roughness induced transition had also been studied.

1 Introduction

DES-type (detached-eddy simulation) model based on the one-equation Spalart-Allmaras (S-A) turbulence model was originally proposed by Spalart to predict the massive separation over twenty years. And then, Strelets constructed the general type of DES based on the two-equation k-ω SST model. Now, DES-type model is one of the most popular RANS-LES (Reynolds-averaged Navier-Stokes and large eddy simulation) hybrid models.

It was found that the grid-induced separation (GIS) occurred when the DES was applied to simulate the attached or small separation flows with a fairly ambiguous grid due to the too early switching from RANS to LES (large eddy simulation). Thus, an advanced version of DDES (delayed-DES) [2] was proposed by introducing a delayed function to avoid the occurrence of GIS, early separation and vortex breakdown. It was verified that DDES performed well in the massive separation. However, it always over-protects the attached boundary layer and it has the problem of log-layer mismatch (LLM). Another advanced DES model is IDDES [3] (improved DDES), which cures the problem of log-layer mismatch. Until now, IDDES is almost the most powerful DES-type model. However, IDDES also has some inherent deficiencies, such as the grey area, i.e., too slow transition from RANS to LES.

Moreover, almost all the DES-type models are based on the full turbulence models, such as S-A, SST, and so on. The natural transition from laminar to turbulent is not considered. It should be urgently improved.

Despite considerable efforts in experimental, theoretical, and numerical studies, many critical physical mechanisms underlying the hypersonic boundary-layer transition are still poorly understood. The various types of potential perturbation include attachment-line instability, thermal and chemical processes, surface roughness, etc.

The traditional local stability analysis can only consider the one-dimensional variation of the mean flow. However, in practice, most flows are typically two- or three-dimensional, for example, the attachment-line instability. These motivate people to develop more sophisticated tools to analyze the realistic flow field. Therefore, based on the linear assumptions [4], it is very natural to extend the local stability analysis to the global analysis [5]. An important feature of hypersonic flows is the high temperature growing in the order of the square of Mach number. The extremely high temperature will excite vibrational and electronic energy of molecules and cause chemical dissociation and even ionization, which in turn decreases the temperature in the field and invalidates the ideal gas assumption [6]. Roughness such as steps [7], gaps [8], humps [9], and indentations play an important role in triggering instability modes [10] or interacting with existing disturbances [11] in the hypersonic boundary layer. However, there is limited research on the complete hypersonic transition mechanisms over a two-dimensional roughness.

2 RANS-LES Hybrid models

2.1 Considering the transition effects

As mentioned before, almost all the DES-type models are constructed based on the full turbulence model. Then, the DES-type models cannot capture the natural transition. If the fundamental model is taken as the transition model, the DES-type model can simultaneously predict the transition on the windward side and massive separation on the leeward side.

The three-equation k-ω-γ transition/turbulence model [12] is developed and improved by our group. To ensure that the transition model acts in the laminar, where the intermittency γ is 0, transitional region, and DDES only acts in the fully turbulent region, where γ is 1, the modified length scale is defined as follows

$$l_{DDES} = l_{RANS} - \frac{1 + sign(1.0, \gamma - C)}{2.0} f_d \max\{0, (l_{RANS} - l_{LES})\}. \tag{1}$$

For the IDDES model, the definition of length scale is a little different from that of DDES.

$$l_{IDDES} = l_{RANS} + \frac{1 + sign(1.0, \gamma - C)}{2.0} \times \left\{ \left[\hat{f}_d(1 + f_e) - 1 \right] l_{RANS} + (1 - \hat{f}_d) l_{LES} \right\}. \tag{2}$$

The hypersonic flow past the Orion capsule is predicted by DDES-FT and DDES-Tr. This flow includes transition on the windward side and massive separation on the leeward side. It is a great challenge to numerical simulation models. Both DDES-FT and DDES-Tr can

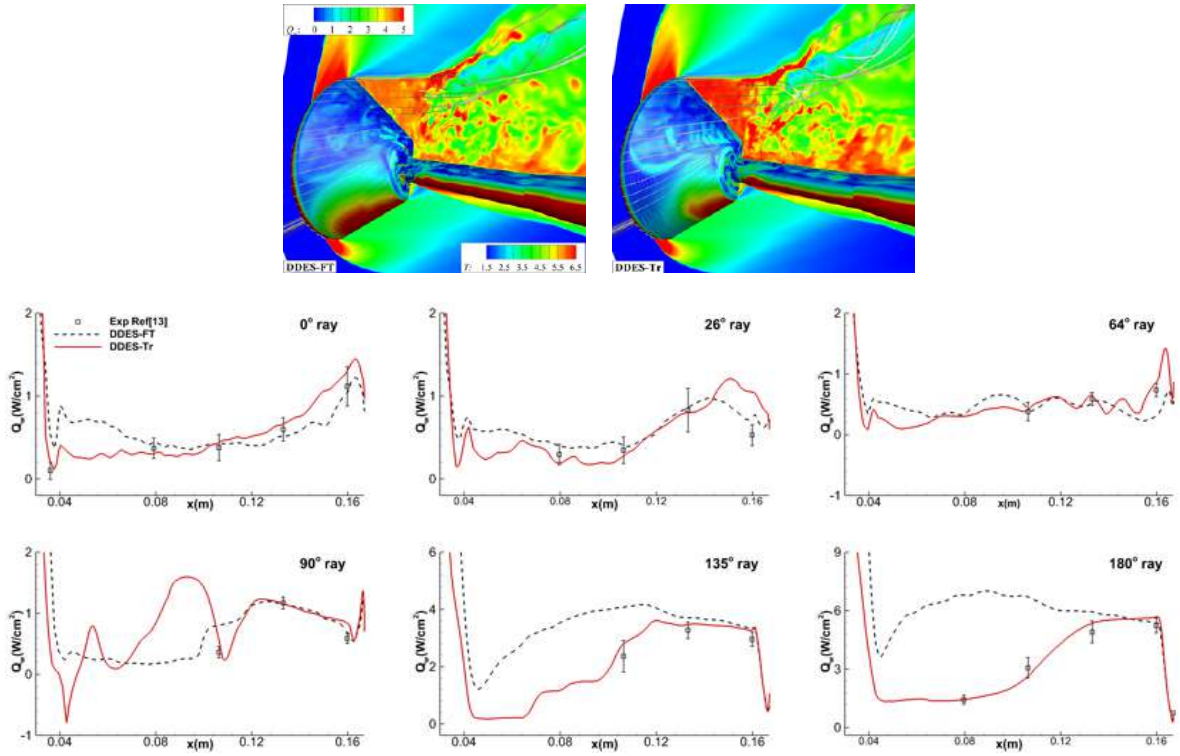

Figure 1: Hypersonic transition and massive separation past Orion capsule by RANS-LES-Tr [1]

predict the aeroheating rate on the leeward side well and only DDES-Tr matches the measurements well on the windward side.

2.2 Alleviating the Grey Area

DDES or DES model has a length scale, L_{LES}, which is defined as $C_{DES}\Delta$. And Δ is taken as the maximum of Δx, Δy and Δz. Here, C_{DES} is a constant and Δ is always taken as the streamwise and spanwise grid scale.

According to the similarity of DES and LES, $\nu_t = (C_S\Delta)^2 S$ and Δ is taken as the streamwise or spanwise length. At the same time, C_S is also constant. Then, the modeled eddy viscosity is too large to resolve the shear-layer instability. And the grey area problem is very distinguishable. According to Moin, the coefficient C_S in the Smagorinsky model should be adjusted between 0.1 and 0.24 to obtain the best performances for different flows. For the DHIT case, a large C_S of 0.18 was recommended. For the shear flows at high Reynolds number, such as channel flow, a small C_S of 0.1 agreed well with the measurements. Then, adaptive coefficient C_{DES} is proposed to bridge the shear flow and massive separation of nearly isotropic flow.

$$C_{DES} = (1 - f_{VTM})C_{DES,min} + f_{VTM}C_{DES,hit} \quad (3)$$

where f_{VTM} is the adaptive function, ranging from 0 to 1 in the separation regions. $C_{DES,hit}$ is calibrated by predicting the DHIT. $C_{DES,min}$ is calculated by

$$C_{DES,min} = \frac{C_{S,min}}{C_{S,hit}} C_{DES,hit} \quad (4)$$

According to Eq. (4), the eddy viscosity at the early shear layer is about 30% of the original one. Some results past the NACA 0015 at low-speed and angle of attack of 13 degrees are presented in Figure (2). From the comparisons of DDES and DDES-AC, the latter model performs much better than DDES.

2.3 Hybrid-based flow control

The separated flows generally lead to airframe noise, pressure fluctuation, shock wave buffet, dynamic airloads, and so on. How to control or reduce the noise and oscillation? Two kinds of method can be generally applied, such as passive and active.

Figure (3) presents some unsteady flows by the passive control devices, such as the turbulence screens for controlling the noise and massive separation past the tandem cylinders at low-speed shown in Figure 3(a), the airbrake for controlling the pitching moment and pressure fluctuations on the vertical tail at low speed and high angle of attack past the fighter model shown in Figure 3(b), the vortex generators for controlling the shock wave buffet at transonic speed past the supercritical wing shown in Figure 3(c), the leading edge saw-tooth spoiler for controlling the dynamic loads at supersonic speed past a cavity model shown in Figure 3(d), and the transition by the diamond roughness elements past the compressor corner at hypersonic speed shown in Figure 3(e). Although the passive control models only can be applied to control the flows, noise or dynamic loads in a narrow range, they are very effective in controlling or reducing the noise, buffet and dynamic airloads, and so on. For the fighter model, the airbrake can not only control the high pitching moment, but it also can reduce the pressure fluctuations on the vertical tail. At the same time, for the cavity model, the saw-teeth spoiler also can both reduce the dynamic loads in the cavity and reduce the drag by the cavity.

3 Instabilities of high-speed flows

3.1 Global stability analysis

The high fidelity base flow solver and high order global stability solver [18] have been developed in LAST. In particular, the leading edge of a wing plays a very im-

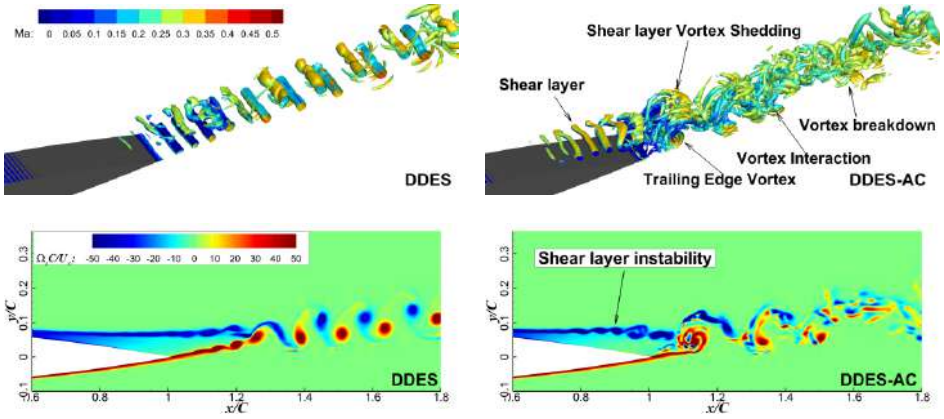

Figure 2: Grey area alleviation from RANS to LES by DDES-AC past NACA 0015 [13]

portant role in boundary layer transition. One noticeable phenomenon in experiments is the leading edge contamination: if the Reynolds number is sufficiently high, the initial turbulent flow could persist along the attachment line. In real flight vehicles, due to significant geometric variation in wing-body junctions, the initial laminar flow could easily become turbulent, contaminating the flow state of the attachment line. Such a phenomenon motivated people to understand the mechanism of the attachment-line transition.

Some global stability results of highly swept flow over a cold cylinder at Mach number 7.14 are shown in Figure (4). In Figure 4(a), the leading global modes of the eigenvalues $\omega = (0.25097, 0.00073146)$ is visualized by iso-surface (positive values in red, negative values in blue) of the surface tangential velocity perturbations, contours of the relative density perturbation are also shown at the background. Figure 4(b) represents the contour of the $x-z$ plane cross-cut at $y = 0.001$ for surface tangential velocity perturbation $V_t(x, y, z)$ together with the streamline over this plane. It is clearly demonstrated that the global modes display the features of both attachment-line modes, as in sweep Hiemenz flow, and cross-flow-like modes further downstream along the surface.

3.2 Thermal-chemical non-equilibrium flow

Thermal-chemical equilibrium models are developed and applied to hypersonic flow simulations, subsequently followed by non-equilibrium models since the rates of thermal and chemical processes are physically finite [19, 20]. Consequently, it is inevitable to investigate the effects of thermal-chemical non-equilibrium on stability and transition.

To describe the thermal-chemical non-equilibrium gases, additional conservations of vibrational energy and species mass are coupled into the Navier-Stokes equation for ideal gases, and the non-dimensional equations are written as follows [21]:

$$\frac{\partial \rho}{\partial t} + \nabla \cdot (\rho \boldsymbol{u}) = 0, \tag{5}$$

$$\rho \frac{\mathrm{D}\boldsymbol{u}}{\mathrm{D}t} + \nabla p - \frac{1}{Re_L} \nabla \cdot \boldsymbol{\tau} = 0, \tag{6}$$

$$\rho c_{p,tr} \frac{\mathrm{D}T}{\mathrm{D}t} - Ec \frac{\mathrm{D}p}{\mathrm{D}t} - \frac{Ec}{Re_L} (\boldsymbol{\tau} : \nabla \boldsymbol{u}) - \nabla \cdot \left(\frac{k_{tr}}{Re_L} \nabla T \right) - \frac{\mu}{Re_L Sc} \nabla T \cdot \left(\sum_{s=1}^{n_s} c_{ptr,s} \nabla Y_s \right) = -Re_L \left(Q_{t-\nu} + \sum_{s=1}^{n_s} h_s \dot{\omega}_s \right) \tag{7}$$

$$\rho \frac{\mathrm{D}Y_s}{\mathrm{D}t} - \nabla \cdot \left(\frac{\mu}{Re_L Sc} \nabla Y_s \right) = Re_L \dot{\omega}_s \tag{8}$$

$$\rho c_{vib} \frac{\mathrm{D}T_\nu}{\mathrm{D}t} - \nabla \cdot \left(\frac{k_\nu}{Re_L} \nabla T_\nu \right) - \frac{\mu}{Re_L Sc} \nabla T_\nu \cdot \left(\sum_{s=1}^{n_\nu} c_{vib,s} \nabla Y_s \right) = Re_L Q_{t-\nu} \tag{9}$$

$$p = \rho R T \tag{10}$$

Furthermore, the corresponding stability equation for thermal-chemical non-equilibrium flow can be derived, and the effects of non-equilibrium on stability can be investigated. Figure (5) shows the effects under different Mach numbers and wall temperatures.

3.3 Roughness induced transition at hypersonic speed

Roughness elements in high-speed flow will lead to an early or late transition from laminar to turbulent flow. In order to find out the effect of the roughness elements on the transition process, we simulate three kinds of 2D roughness elements interacting with a pair of oblique waves in a 3D computational field. The transition problem is studied with an implicit large eddy simulation approach based on a high-order scheme [22].

Figure 6(a)-Figure 6(d) show the vortex evolutions of the transition processes by using the Q-criterion. Comparing with a flat plate flow without the roughness element, as shown in Figure 6(a), the gap has almost no effect on the oblique transition in Figure 6(b) [23, 24]. In Figure 6(c), the oblique transition in the forward-facing step flow is earlier than the flow without a roughness. In contrast, the backward-facing step will delay the transition, as shown in Figure 6(d). The evolution of the maximum streamwise fluctuating-velocity $|u'_{max}/U_\infty|$ in Figure 6(e) shows that the velocity fluctuation increases at the head of the forward-facing step and decreases after the backward-facing step. The change of velocity and pressure [25] in the vicinity of the step flows dominate the disturbance change in these cases. The evolutions of the

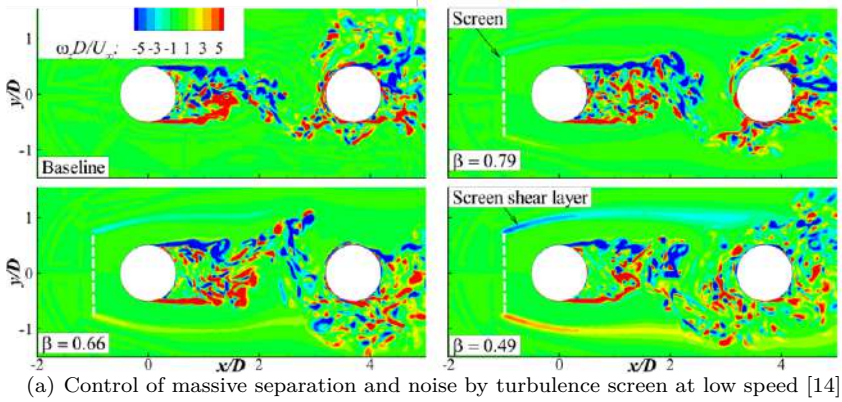

(a) Control of massive separation and noise by turbulence screen at low speed [14]

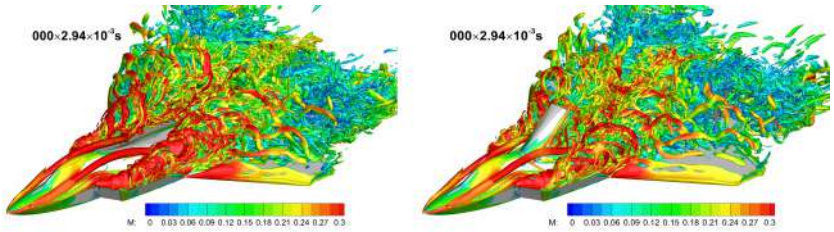

(b) Control of pitching moment and pressure fluctuations by airbrake at low speed[15]

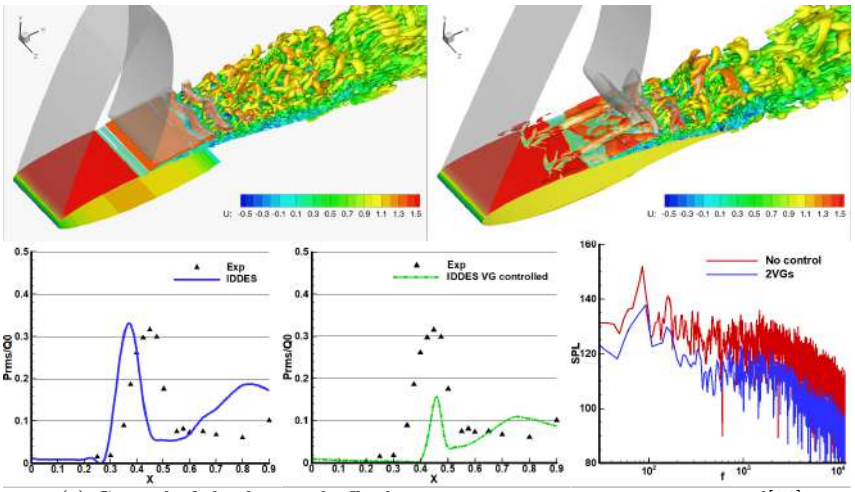

(c) Control of shock wave buffet by vortex generator at transonic speed[16]

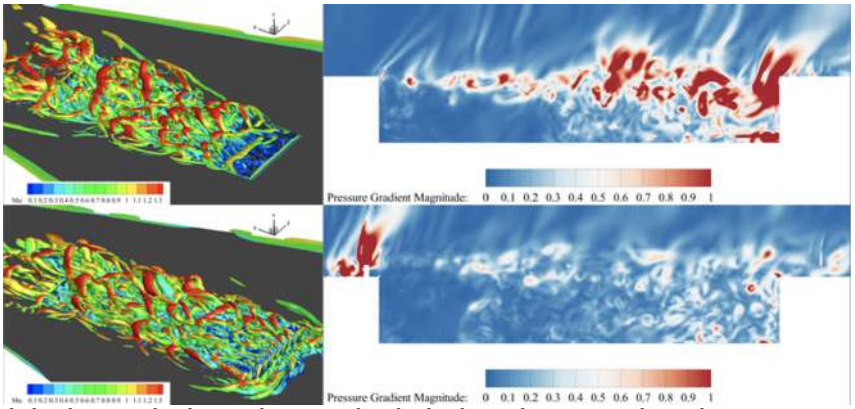

(d) Control the dynamic load past the cavity by the leading-edge saw-tooth spoiler at supersonic speed[17]

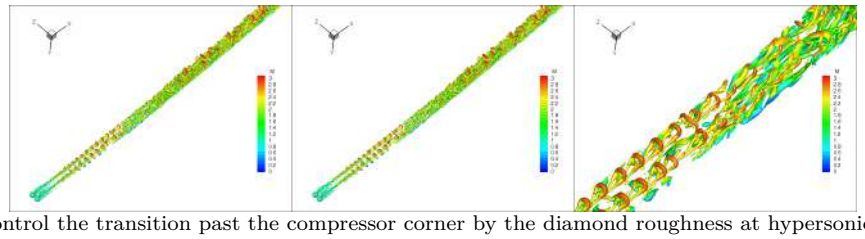

(e) Control the transition past the compressor corner by the diamond roughness at hypersonic speed

Figure 3: Some unsteady flows by passive control devices

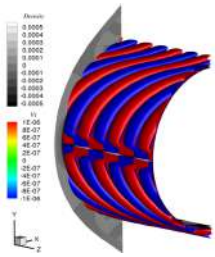

(a) A typical leading global mode

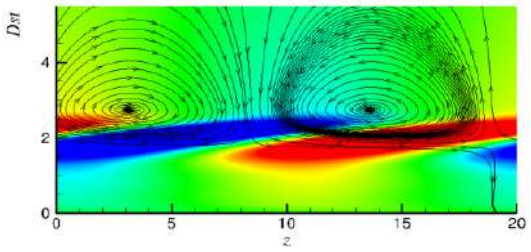

(b) Contour of the $x-z$ plane cross-cut at $y = 0.001$

Figure 4: Global analysis of highly swept flow over a cylinder at Mach 7.14

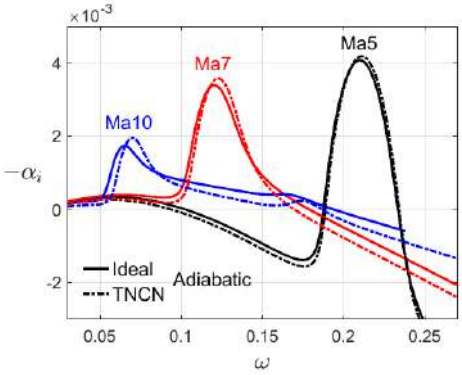

(a) Effect of Mach numbers

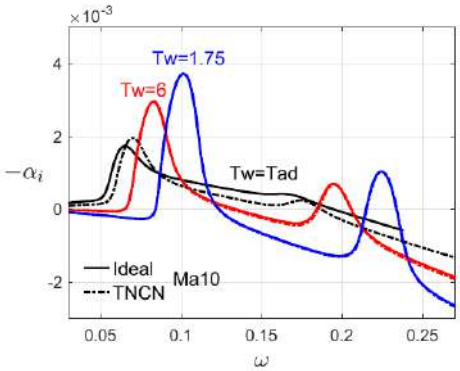

(b) Effect of temperatures

Figure 5: Comparisons of the growth rate between the ideal and thermal-chemical non-equilibrium flow

skin friction coefficient in Figure 6(f) indicates the transition location with and without a roughness element. This work provides a theoretical basis for the design of the transition control methodology and the transition location prediction in a real high-speed aircraft.

4 Summary

This paper introduces the latest research work at LAST on the hybrid model and transition studies. Simulation results have been briefly discussed. Below are the conclusions:

(1) A length scale has been proposed, and the DES-type model has been extended to the transitional flow. The prediction of DDES-Tr matches the measurement aeroheating rate on both windward and leeward sides.

(2) An adaptive coefficient C_{DES} is adopted to alleviate the grey area. The results of NACA 0015 show that the DDES-AC performs much better than the traditional DDES.

(3) A series of simulations have been conducted on the control of separation flows by passive methods from low to supersonic speed.

(4) A highly efficient global stability analysis solver has been developed. The attachment-line transition has been studied with global stability analysis.

(5) The effect of thermal non-equilibrium flow has been investigated. Both the Mach number and wall temperature can significantly influence the stability.

(6) The geometry of the 2D roughness elements is of vital importance in effect on the hypersonic boundary layer transition.

Acknowledgment

This work was supported by the National Key Project (Grant No. GJXM92579), EU-China joint IMAGE project (Grant No 688971) and the National Natural Science Foundation of China (Grant No. 91952302, 11772174 and 91852113). The authors also would like to thank the supports from the National Key Research and Development Program of China (Grant No. 2016YFA0401200 and 2019YFA0405300). We also express our gratitude to Tsinghua National Laboratory for Information Science and Technology, Shanghai Super-Computation Center and Parallel Technology for computation resources.

References

[1] Z. Xiao, G. Wang, M. Yang, and L. Chen, "Numerical investigations of hypersonic transition and massive separation past orion capsule by ddes-tr," *International Journal of Heat and Mass Transfer*, vol. 137, pp. 90–107, 2019.

[2] P. R. Spalart, S. Deck, M. L. Shur, K. D. Squires, M. K. Strelets, and A. Travin, "A new version of detached-eddy simulation, resistant to ambiguous grid densities," *Theoretical and computational fluid dynamics*, vol. 20, no. 3, p. 181, 2006.

[3] M. L. Shur, P. R. Spalart, M. K. Strelets, and A. K. Travin, "A hybrid rans-les approach with delayed-des and wall-modelled les capabilities," *International Journal of Heat and Fluid Flow*, vol. 29, no. 6, pp. 1638–1649, 2008.

[4] V. Theofilis, "Advances in global linear instability analysis of nonparallel and three-dimensional

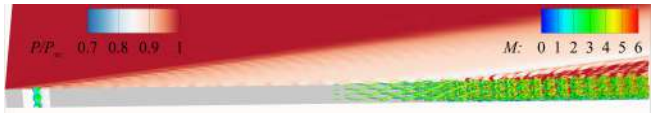

(a) Oblique transition in a flat plate flow

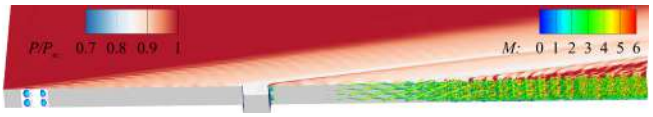

(b) Oblique transition affected by a gap

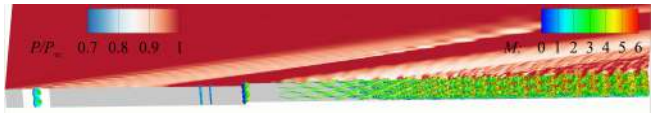

(c) Oblique transition affected by a forward-facing step

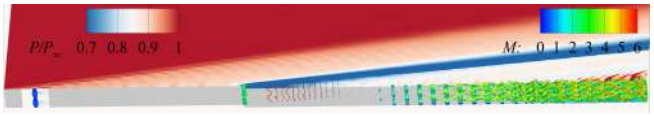

(d) Oblique transition affected by a backward-facing step

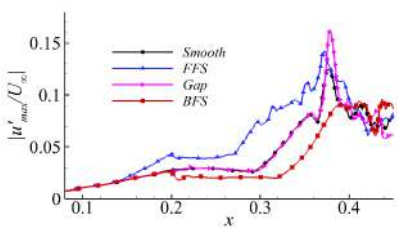

(e) Velocity fluctuation in the streamwise direction

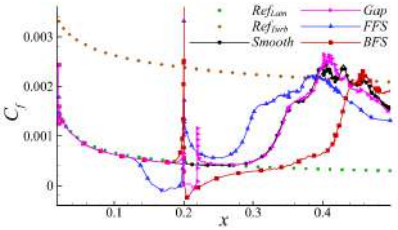

(f) The skin friction coefficient in the streamwise direction

Figure 6: Transition influenced by a 2D roughness element

flows," *Progress in aerospace sciences*, vol. 39, no. 4, pp. 249–315, 2003.

[5] V. Theofilis, "Global linear instability," *Annual Review of Fluid Mechanics*, vol. 43, pp. 319–352, 2011.

[6] J. D. Anderson Jr, *Hypersonic and high-temperature gas dynamics*. American Institute of Aeronautics and Astronautics, 2006.

[7] M. W. Tufts, H. L. Reed, B. K. Crawford, G. T. Duncan Jr, and W. S. Saric, "Computational investigation of step excrescence sensitivity in a swept-wing boundary layer," *Journal of Aircraft*, vol. 54, no. 2, pp. 602–626, 2017.

[8] S. A. Berry and T. J. Horvath, "Discrete-roughness transition for hypersonic flight vehicles," *Journal of Spacecraft and Rockets*, vol. 45, no. 2, pp. 216–227, 2008.

[9] C. L. Haley, K. M. Casper, and X. Zhong, "Joint numerical and experimental investigation of roughness effect on hypersonic 2nd mode instability and transition," in *AIAA Scitech 2019 Forum*, p. 0873, 2019.

[10] J. Rossiter, "Wind tunnel experiments on the flow over rectangular cavities at subsonic and transonic speeds," tech. rep., Ministry of Aviation; Royal Aircraft Establishment; RAE Farnborough, 1964.

[11] O. Marxen, G. Iaccarino, and E. S. Shaqfeh, "Nonlinear instability of a supersonic boundary layer with two-dimensional roughness," *Journal of fluid mechanics*, vol. 752, pp. 497–520, 2014.

[12] S. Fu and L. Wang, "Rans modeling of high-speed aerodynamic flow transition with consideration of stability theory," *Progress in Aerospace Sciences*, vol. 58, pp. 36–59, 2013.

[13] J. Liu, W. Zhu, Z. Xiao, H. Sun, Y. Huang, and Z. Liu, "Ddes with adaptive coefficient for stalled flows past a wind turbine airfoil," *Energy*, vol. 161, pp. 846–858, 2018.

[14] W. Zhu, Z. Xiao, and S. Fu, "Numerical modeling screen for flow and noise control around tandem cylinders(in revision)," *AIAA Journal*.

[15] W. Cui, J. Liu, Y. Sun, Q. Li, and Z. Xiao, "Air-brake controls of pitching moment and pressure fluctuation for an oblique tail fighter model," *Aerospace science and technology*, vol. 81, pp. 294–305, 2018.

[16] J. Huang, Z. Xiao, J. Liu, and S. Fu, "Simulation of shock wave buffet and its suppression on an oat15a supercritical airfoil by iddes," *Science China Physics, Mechanics and Astronomy*, vol. 55, no. 2, pp. 260–271, 2012.

[17] K. Luo, W. Zhu, Z. Xiao, Z. Weng, L. Deng, D. Yang, and J. Liu, "Investigation of spectral characteristics by passive control methods past a supersonic cavity," *AIAA Journal*, vol. 56, no. 7, pp. 2669–2686, 2018.

[18] Y. Xi and S. Fu, "Receptivity analysis over elliptical cones at mach number 7.45," in *IUTAM transition*, 2019.

[19] P. A. Gnoffo, *Conservation equations and physical models for hypersonic air flows in thermal and chemical nonequilibrium*. National Aeronautics and Space Administration, Office of Management, Scientific and Technical Information Division, 1989.

[20] G. V. Candler, "Rate effects in hypersonic flows," *Annual Review of Fluid Mechanics*, vol. 51, pp. 379–402, 2019.

[21] X. Chen, P. C. Boldini, and S. Fu, "Research on hypersonic boundary-layer stability with high-temperature effects," in *Asia-Pacific International Symposium on Aerospace Technology*, pp. 499–512, Springer, 2018.

[22] H. Zhu, S. Fu, L. Shi, and Z. Wang, "Implicit large-eddy simulation for the high-order flux reconstruction method," *AIAA Journal*, pp. 2721–2733, 2016.

[23] Y. Xue, L. Wang, Z. Wang, and S. Fu, "Gap-induced transition via oblique breakdown at mach 6," *Shock Waves*, vol. 29, no. 8, pp. 1181–1190, 2019.

[24] Y. Xue, Z. Wang, and S. Fu, "Impact of a gap on boundary layer transition at mach 6," in *FLUCOME*, 2019.

[25] Y. Xue, J. Ren, J. Luo, and S. Fu, "Drag increment induced by a small-scale forward-facing step in mach 5 turbulent boundary layer flows(accpeted)," *Chinese Journal of Aeronautics*.

Towards a Separation Sensitive Explicit Algebraic Reynolds Stress RANS Model

S. Monté, L. Temmerman, B. Tartinville, B. Léonard and C. Hirsch

Numeca International S.A., 189 Chaussée de La Hulpe, 1170 Brussels, Belgium

Abstract

The present paper deals with the development of a novel **E**xplicit **A**lgebraic **R**eynolds **S**tress (EARSM) turbulence model, the **S**eparation **S**ensitive **C**orrected (SSC-EARSM) model [10], specifically designed with the aim of better predicting separated flows. The starting point of the model is the SBSL-EARSM model [9] (SBSL stands for **S**implified **B**a**S**e**L**ine) in which three modifications are introduced based on identified weaknesses of the said model, namely the near-wall behaviour of the model, the under-prediction of the shear stress level in the separated shear layer, and its ability to detect separation. The introduction of these modifications allows for a strong improvement in predicting the shear stress across the separating shear layer leading to, therefore, a much improved prediction of the separation zone as demonstrated here. This development shows that current weaknesses of most RANS models can be corrected. This is demonstrated in this work by reference to two well-known reference hill flows as well as the application of the model to the **C**ommon **R**esearch **M**odel [18] (CRM) designed for and considered during the AIAA Drag Prediction Workshops and the JAXA **A**erodynamic **P**rediction **C**hallenge (APC) Workshops.

1 Introduction

While unsteady approaches such as hybrid RANS-LES, LES and, even DNS, are gaining a foothold as industrial tools for the simulation of turbulent flows and the associated phenomena thanks in greatest part to the ever-growing availability of computational power and its associated cost reduction, RANS modelling remains an important, if not traditional, approach for simulating turbulence thanks to its relatively low cost, for design cycles. This is despite the limitations of the assumptions on which RANS is build.

Consequently, RANS model development remains an area where research is needed, as highlighted by the NASA CFD-2030 Vision Document [15]. The European Commission is also funding research on this area with projects such as the recently started HiFi-Turb project[1], coordinated by NUMECA, which aims at generating high fidelity databases on industrial-type configurations and exploiting them for this very purpose with the help of deep learning and artificial intelligence techniques.

[6] points out that flows featuring a separation from a slope such as the flow over a hill remain beyond the reach of most of the present RANS closures, even the more complex ones. [6] further states that the inability of these models to include any spectral dynamics limits their use when attempting the capture of flows dominated by large-scale dynamics. The direct consequence is that these models return an insufficient level of turbulence intensity in the separated shear layer. As it controls the reattachment process, this leads to an over-prediction of the length of the recirculation zone. Indeed, a low level of turbulence activity results in a retardation of the transport momentum which causes a reduction of the volume of fluid entrained into the shear layer, itself leading to a delay of the flow reattachment and an extension of the separation region length. A key element of any model improvement is thus the need to maintain a high level of shear stress in the separated mixing layer.

The present model has thus been designed with this in mind. The SSC-EARSM model is derived from the SBSL-EARSM model [9] and combines a sensitization to promote separation and a correction of the shear stress in the separated region.

In the following section, the key elements of the SSC-EARSM model will be summarized. The interested reader will find additional information as well as a more complete description of the model in [10, 11]. Section 3 will focus on results including the turbulent flat plate, two hill flows, and, as industrial demonstrator, the transonic flow around the generic CRM wing-body aircraft configuration. Additional configurations covering automotive and aeronautical applications are considered in [10,11,4]. Concluding remarks are then drawn.

2 Formulation of the SSC-EARSM model

The SBSL-EARSM model [9] is used as a starting point for the development of the SSC-EARSM model due to its performances in capturing separated flows [7].

Through *a-priori* and *a-posteriori* testing using the DNS database of a turbulent flat plate [13] and the highly resolved LES data of the flow over a curved backward facing step [3], two areas for improvement have been identified. The first is the near-wall behavior of the model. The second consists of accurately capturing the intensity of both the turbulence energy and the shear stress in the separated shear layer.

It has been observed that the dissipation rate is overestimated in the buffer zone of the boundary layer, leading to an excessive destruction of the turbulence energy. A damping function, f_β, is therefore introduced in (1) fol-

[1] https://www.ercoftac.org/hifi-turb-project/

lowing [1].

$$\frac{Dk}{Dt} = P_k(1 + f_{SSE}) - \overbrace{f_\beta \beta^\star k\omega}^{\epsilon} + \frac{\partial}{\partial x_i}\left[(\nu + \sigma_k \nu_t \frac{\partial k}{\partial x_i})\right] \quad (1)$$

This damping function writes:

$$f_\beta = \frac{\frac{0.075}{0.27} + \left(\frac{Re_{tw}}{8}\right)^4}{1 + \left(\frac{Re_{tw}}{8}\right)^4} \quad \text{with} \quad Re_{tw} = \frac{k}{\omega\nu} \quad (2)$$

The second near-wall correction aims at correctly capturing the near-wall behavior of the Reynolds stresses by introducing a van Driest damping function [19] defined as:

$$f_1 = 1 - e^{-\frac{y^\star}{26}} \quad (3)$$

with $y^\star$ defined according to [14]:

$$y^\star = 2.4\sqrt{Re_y} + 0.003Re_y^2 \quad \text{with} \quad Re_y = \frac{\sqrt{k}d}{\nu} \quad (4)$$

The rationale behind the introduction of (3) rests on an *a-priori* study carried on a turbulent boundary layer of the behavior of the effective eddy viscosity coefficient defined as:

$$C_\mu^{eff} = -0.5\beta_1 = -\frac{u'v'}{k}\frac{\partial U}{\partial y} \quad (5)$$

These corrections lead to a better prediction of the turbulence energy in the boundary layer. An unfortunate consequence is that the increase in turbulence intensity may delay the point at which separation occurs, hence the need for sensitizing the model to flow separation. This is achieved by introducing two additional modifications.

The first correction is the function f_{SSE} introduced in (1). SSE stands for **S**hear **S**tress **E**nhancement. Its purpose is to enhance the production of the shear stress in the separated shear layer by locally increasing the production of the turbulence energy P_k . The correction is based on the observation that, when the flow separates, the streamwise velocity exhibits an inflexion point i.e. the shear is maximum near this point. This region is identified by using the von Karman length scale L_{vk} defined as:

$$L_{vk} = \frac{S}{|\nabla^2 U|} \quad (6)$$

where S is the magnitude of the strain rate. The function f_{SSE} reads:

$$f_{SSE} = f_1 f_d e^{-0.1\left(\frac{L}{L_{vk}} - 1\right)^2} \quad (7)$$

The term $f_1 f_d$ prevents the function f_{SSE} from being active very near the wall as well as when the flow is attached. The function f_1 is defined in (3) while the function f_d ([16]) reads:

$$f_d = 1 - tanh\left(c_s \frac{\nu + \nu_t}{\kappa^2 d^2 \sqrt{U_{i,j}U_{i,j}}}\right) \quad (8)$$

where $c_s = 8f_{HiRe} + 6(1 - f_{HiRe})$. The function f_{HiRe} allows switching between low and high local Reynolds number and is defined as:

$$f_{HiRe} = 1 - e^{-(y^\star/5000)} \quad (9)$$

The second modification to further sensitize the model to the separation, consists of introducing a recalibrated version of the **S**cale **A**daptive **S**imulation (SAS) term ([8]) following [6] and denoted P_{SAS} in (10). The ω-equation thus writes:

$$\frac{D\omega}{Dt} = \underbrace{\gamma\frac{\omega}{k}P_k}_{P_\omega} - \beta\omega^2 + \frac{\partial}{\partial x_i}\left[(\nu + \nu_t)\frac{\partial \omega}{\partial x_i}\right] + \sigma_d \frac{\partial k}{\partial x_i}\frac{\partial \omega}{\partial x_i} + P_{SAS} \quad (10)$$

This term is defined as:

$$P_{SAS} = C_{SAS,1} min(1000P_\omega, max(P^\star_{SAS}, 0)) \quad (11)$$

with

$$P^\star_{SAS} = C_{SAS,2}\kappa S^2 \sqrt{\frac{L}{L_{vk}}} \quad (12)$$
$$-8.55C_{SAS,3}k\ max\left(\frac{1}{k^2}\frac{\partial k}{\partial x_i}\frac{\partial k}{\partial x_i}, \frac{1}{\omega^2}\frac{\partial \omega}{\partial x_i}\frac{\partial \omega}{\partial x_i}\right)$$

with $C_{SAS,1} = 1$, $C_{SAS,2} = 3.6517$ and $C_{SAS,3} = 2.25f_{HiRe} + 2.75(1 - f_{HiRe})$. Note that the constants used here are slightly different from those given in [10] following additional testing and recalibration. For attached flows, (11) is negligible while it is active in the separation region for detached flows. This term increases the production of the turbulence specific dissipation rate, leading, by balance, to an increase in the production of turbulence energy and thus an increase in turbulence viscosity that eases the separation. The SAS and SSE terms act together by promoting a more intense mixing between the freestream and separated regions leading to an improvement in the predictive capability of the model.

3 Results

3.1 The turbulent flat plate

The objective of this test is to demonstrate that the modifications brought into the model do not deteriorate the prediction of attached flows. The computations are performed by reference to DNS data [13] at $Re_\theta = 2,540$ and compare the performance of the SSC-EARSM and SBSL-EARSM models.

Figure 1 shows that the introduction of the dissipation rate damping (2) in (1) improves the prediction of the turbulence energy, especially in the nearwall region. Figure 2 shows the prediction of the streamwise velocity. In the buffer region ($5 < y^+ < 20$), the new model predicts a profile that is in better agreement with the DNS data. This improvement extends into the log region. Note that, for this flow, and as expected, the additional SAS and SSE terms are not active. Figure 3 demonstrates that, although the SBSL-EARSM does work reasonably well, the SSC-EARSM model greatly improves the prediction of P_k/ϵ by correctly capturing the peak in the buffer region as well as the local minimum and maximum in the log region.

3.2 The curved backward facing step

The second case considered in this paper is the curved backward facing step [3] at $Re_H = 13,700$ based on the step height H and the centre-line channel velocity at inlet. The reference data originates from a highly resolved LES computation.

Table 1 reports the streamwise locations of both the separation and reattachment points for the reference LES [3], the SBSL-EARSM model and the SSC-EARSM model. Both models over-predict the separation point,

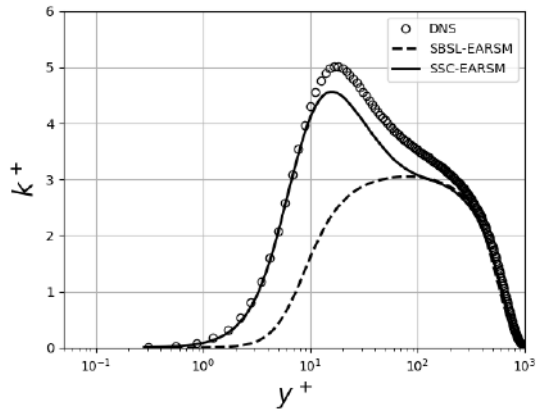

Figure 1: Distribution of turbulence energy as a function of the wall distance in wall units for the turbulent flat plate. Comparison with DNS data [13]

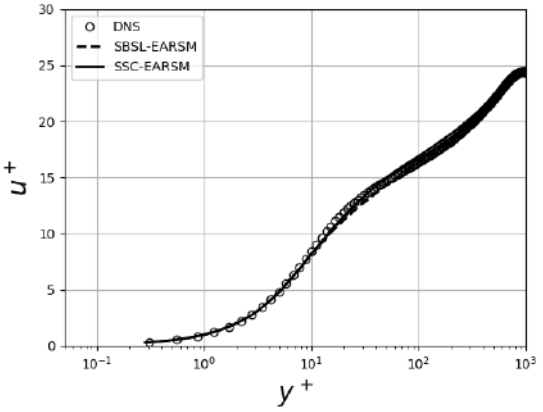

Figure 2: Streamwise velocity profile distribution as a function of the wall distance in wall units for the turbulent flat plate. Comparison with DNS data [13]

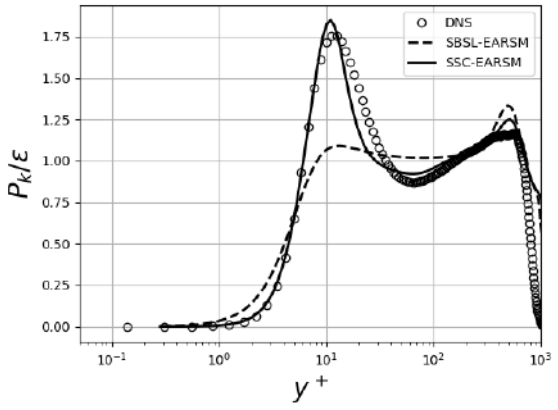

Figure 3: Ratio of the turbulence energy production to the dissipation rate P_k/ϵ as a function of the wall distance in wall units for the turbulent flat plate. Comparison with DNS data [13]

Table 1: Prediction of the separation and reattachment positions for the separated region for the curved backward facing step

	$(x/H)_{sep.}$	$(x/H)_{reat.}$
LES[3]	0.83	4.36
SBSL-EARSM	0.95	4.97
SSC-EARSM	1.12	4.34

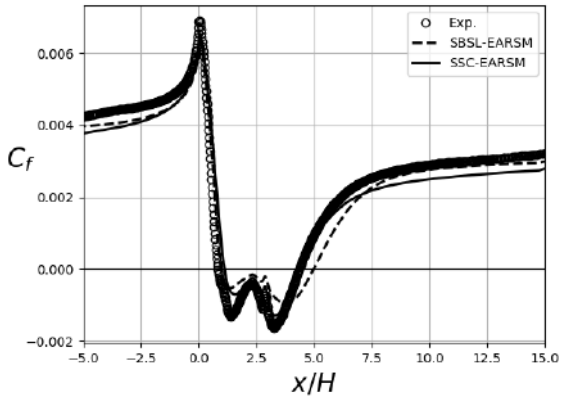

Figure 4: Prediction of the skin friction coefficient as a function of the streamwise position for the curved backward facing step. Comparison with LES data [3]

the new model showing the most delay while the reattachment point is correctly predicted by the new model and over-predicted by the SBSL-EARSM model. This is confirmed in Figure 4, which shows the skin friction coefficient along the lower wall. The SSC-EARSM model provides here the better match. Figure 5 looks at the velocity profile at different streamwise locations with the predictions of the new model being in close agreement with the reference data [3].

Figure 6 shows the prediction of the shear stress at different streamwise locations in the channel. The good agreement of the predictions made by the SSC-EARSM model with the reference data demonstrates the positive impact brought by the corrections made to enhance the turbulence intensity and promote the turbulent mixing in the separated shear layer.

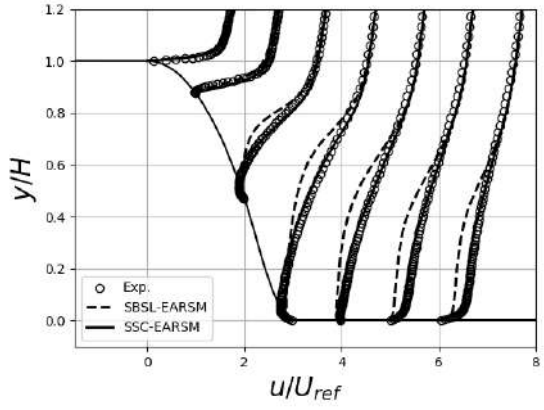

Figure 5: Prediction of the streamwise velocity at different streamwise locations for the curved backward facing step. Comparison with LES data [3]

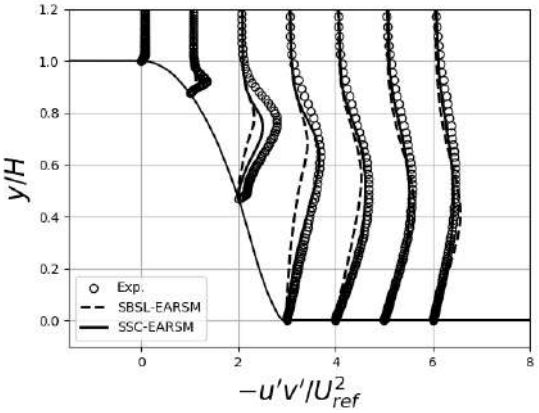

Figure 6: Prediction of the shear stress at different streamwise locations for the curved backward facing step. Comparison with LES data [3]

Table 2: Prediction of the separation and reattachment positions for the NASA hump

	$(x/c)_{sep.}$	$(x/c)_{reat.}$
Exp[5]	0.66	1.11
SBSL-EARSM	0.66	1.17
SSC-EARSM	0.66	1.08

3.3 The NASA hump flow

This test case has been investigated experimentally [5] and numerically with LES [2] and consists of a high Reynolds number flow over a smooth step. Based on the chord length c and the freestream velocity, the Reynolds number is equal to 936,000. With a steeper step than the previous case, the flow separation location is easier to predict. The separation zone is relatively small ($0.35c$). This case is very challenging for RANS models as most fail to predict correctly the separation length. NASA [15] points to the fact that models generally under-predict the shear.

Figure 7 shows the distribution of the skin friction coefficient confirming that the SSC-EARSM predicting a slightly shorter separation zone than the experiment while the SBSL-EARSM over-predicts it. Therefore, the SSC-EARSM model gives a much improved picture of the streamwise velocity as shown in Figure 8 and the shear stress as shown in Figure 9. This latest figure again demonstrates the positive impact of the modifications brought into the model.

3.4 The Common Research Model as considered in the JAXA APC-III workshop

The case considered in this section is an aeronautical application: the NASA Common Research Model (CRM) [18]. The configuration corresponds to a generic, modern design of a civil aircraft at high cruising speed. The geometry has been used during the recent AIAA Drag Prediction Workshops[2] and the Aerodynamics Prediction Challenge workshops[3] organised by JAXA. Experimental data [17] were obtained from a wind tunnel for an 80% scaled copy of the CRM. The experiments were

[2]https://aiaa-dpw.larc.nasa.gov/
[3]https://cfdws.chofu.jaxa.jp/apc/apc3/

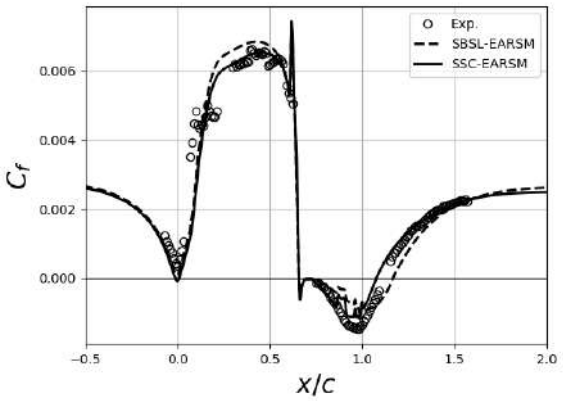

Figure 7: Prediction of the skin friction coefficient as a function of the streamwise position for the NASA hump. Comparison with experimental data [5]

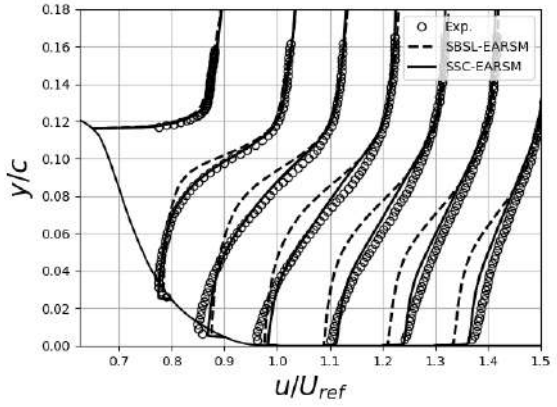

Figure 8: Prediction of the streamwise velocity at different streamwise locations for the NASA hump. Comparison with experimental data [5]

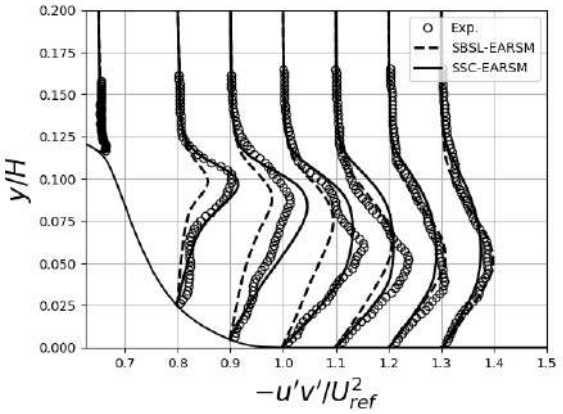

Figure 9: Prediction of the shear stress at different streamwise locations for the NASA hump. Comparison with experimental data [5]

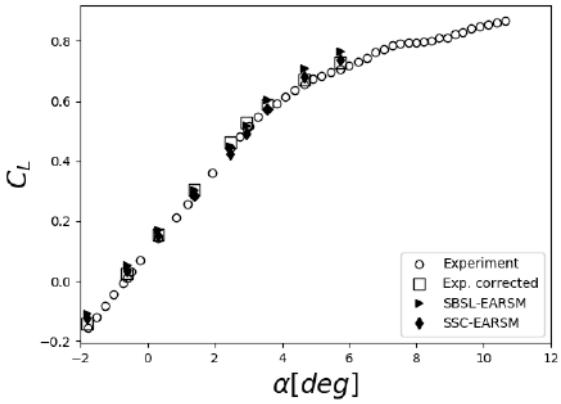

Figure 10: Lift coefficient as a function of the angle of incidence for the CRM configuration. Comparison with experimental data [17]

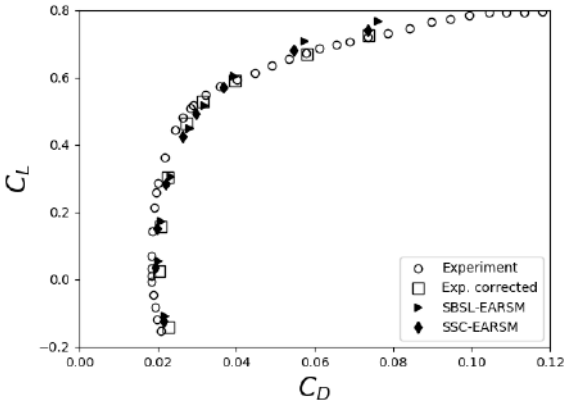

Figure 11: Lift coefficient as a function of the drag coefficient for the different angles of incidence for the CRM configuration. Comparison with experimental data [17]

conducted in the $2m \times 2m$ JAXA transonic wind tunnel. The flow corresponds to a Mach number of 0.847 and a Reynolds number based on the mean aerodynamic chord of 2,260,000 for different angles of incidence ranging from $-1.79°$ to $5.72°$. The present results consist of a subset of data obtained in the course of a contribution to APC-III ([4]) with the objective of demonstrating that the model improvements described in the present paper also translate into an improvement for a realistic configuration. The focus thus remains on the model described in the present paper.

A family of hex-dominant meshes of around 33 million cells each, generated with the commercial mesh generator HEXPRESS^{TM}/HYBRID [12], is used.

Figure 10 shows the prediction of the lift coefficient by the SBSL-EARSM and the SSC-EARSM models for all the angles of incidence considered compared with the experimental data. The set of reference data includes "corrected data" which takes into account support interferences[3]. Especially at the higher angles of attack, the lift coefficient predicted by the SSC-EARSM model agrees fairly well with the experimental data, particularly with the corrected ones. Figure 11, showing the lift coefficient as a function of the drag coefficient, further highlights this results. Figure 12 shows the prediction of the pitching moment coefficient. Both models achieve a reasonable prediction of this quantity, which is notoriously difficult to capture accurately. Figure 13 looks at selected distributions of the pressure coefficient on the wing for an angle of attack of $4.65°$. At the lowest angles of incidence, both models predict very similar results as illustrated by Figure 10 for example. It is not the case at the higher angles of attack where the SSC-EARSM model shows an improvement in the capture of the pressure distribution. This is explained by the fact that the flow features on the upper side of the wing are better captured.

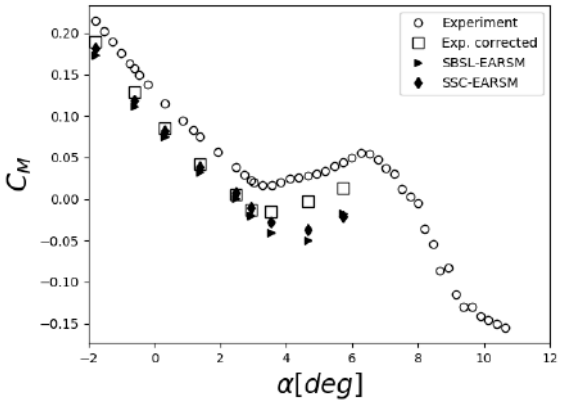

Figure 12: Pitching moment coefficient as a function of the angle of incidence for the CRM configuration. Comparison with experimental data [17]

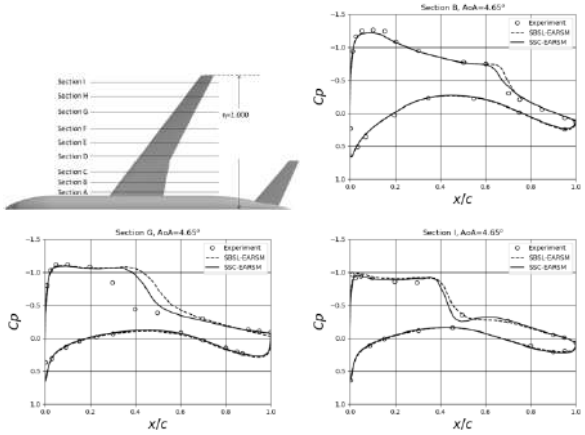

Figure 13: Pressure coefficient distribution at three spanwise locations along the chord at $4.65°$ of incidence. Comparison with experimental data [17]. Top left corner: positions at which pressure coefficient profiles have been extracted

4 Conclusions

The present paper summarizes efforts made to improve the predicting capabilities of an existing RANS model for separated flows. This is achieved by incorporating the von Karman length scale into the model. This allows to take into account, in a generic way, the ratio of the first

[3]https://cfdws.chofu.jaxa.jp/apc/apc3/

to second derivatives of the velocity field, allowing for the promotion of a selective enhancement of the production of both the turbulence energy and the dissipation rate, mostly in the separated shear layer. Consequently, the main flow features for the cases considered are better captured as demonstrated in the previous sections.

Acknowledgements

The authors would like to acknowledge the financial support of the European Commission through the ANADE project (Advances in Numerical and Analytical tools for DEtached flow prediction). The authors are very grateful to Professor M. Leschziner for the many discussions during the course of this work.

References

[1] Abe, K., Jang, Y.J. and Leschziner, M.A. (2003), An investigation of wall-anisotropy expressions and length-scale equations for non-linear eddy-viscosity models, Int. J. Heat Fluid Flow, vol. 24, pp. 181-198.

[2] Avdis, A., Lardeau, S. and Leschziner, M.A. (2009), Large eddy simulation of separated flow over a two-dimensional hump wih and without control by means of a synthetic slot-jet, Flow Turbul. Combust., vol. 83, $n°3$, pp. 343-370.

[3] Bentaleb, Y., Lardeau, S. and Leschziner, M.A. (2011), Large-eddy simulation of turbulent boundary-layer separation from a rounded step, Journal of Turbulence, vol. 13, pp. 1-28.

[4] Botella C., J., Léonard, B., Temmerman, L., Hirsch, C. (2018), Sensitivity to turbulence models and numerical dissipation of the CRM drag prediction, AIAA Paper 2018-3332.

[5] Greenblatt, D., Paschal, K.B., Yao, C.-S., Harris, J., Schaeffler, N.W. and Washburn, A.E. (2006), Experimental investigation of separation control. Part 1: baseline and steady suction, AIAA J., vol. 44, pp. 2820-2830.

[6] Jakirlić, S. and Maduta, R. (2015), Extending the bounds of 'steady' RANS: toward an instability-sensitive Reynolds stress model, Int. J. Heat Fluid Flow, vol. 51, pp. 175-194.

[7] Mehdizadeh, O., Temmerman, L., Tartinville, B. and Hirsch, C. (2012), Application of EARSM turbulence model to internal flows, ASME Paper GT-2012-68886.

[8] Menter, F.R. and Egorov, Y. (2010), The scale-adaptive simulation method for unsteady turbulent flow predictions. Part 1: theory and model description, Flow Turbul. Combust., vol. 85, pp. 113-138.

[9] Menter, F.R., Garbaruk, A.V. and Egorov, Y. (2012), Explicit algebraic Reynolds stress models for anisotropic wall-bounded flows, Progress in Flight Physics, Vol. 3, pp. 89-104.

[10] Monté, S., Temmerman, L., Tartinville, B., Léonard, B. and Hirsch, C. (2016), A novel EARSM model for separated flows, in 11th International ERCOFTAC Symposium on Engineering Turbulence Modelling and Measurements, Palermo, Italy.

[11] Monté, S., Temmerman, L., Tartinville, B., Léonard, B. and Hirsch, C. (in preparation), SSC-EARSM: A novel EARSM model for separated flows.

[12] NUMECA International, "Products". [Online] Available: https://www.numeca.ne/products.

[13] Schlatter, P., Li, Q., Brethouwer, G., Johansson, A.V. and Henningson, D.S. (2010), Simulations of spatially evolving turbulent boundary layers up to $Re_\theta = 4300$, Int. J. Heat Fluid Flow, vol. 31, pp. 251-261.

[14] Skote, M. and Wallin, S. (2016), Near-wall damping in model predictions of separated flows, Int. J. Comp. Fluid Dyn., vol. 30, pp. 218-230.

[15] Slotnick, J., Khodadoust, A., Alonso, J., Darmofal, D. Gropp, W., Lurie, E. and Mavripilis, D. (2014), CFD vision 2030 study: a path to revolutionary computational aerosciences, NASA/CR-2014-218178.

[16] Spalart, P.R., Deck, S., Shur, M.L., Strelets, M.K. and Travin, A. (2006), A new version of detached-eddy simulation, resistant to ambiguous grid densities, Theoret. Comput. Fluid Dynamics, vol. 20, pp. 181-195.

[17] Ueno, M., Kohzai, T. and Koga, S. (2014), JAXA Research and Development Memorandum. Transonic wind tunnel test of the NASA CRM, vol. 1.

[18] Vassberg, J., Dehaan, M., Rivers, M. and Wahls, R. (2008), Development of a Common Research Model for applied CFD validation studies, AIAA Paper 2008-6919.

[19] Wallin, S. and Johansson, A.V. (2000), An explicit algebraic Reynolds stress model for incompressible and compressible turbulent flows, J. Fluid Mech., vol. 403, pp. 89-132.

Turbulence

Introduction to Theory and Applications of Turbulent Flows

Frans T.M. Nieuwstadt, Bendiks J. Boersma, Jerry Westerweel

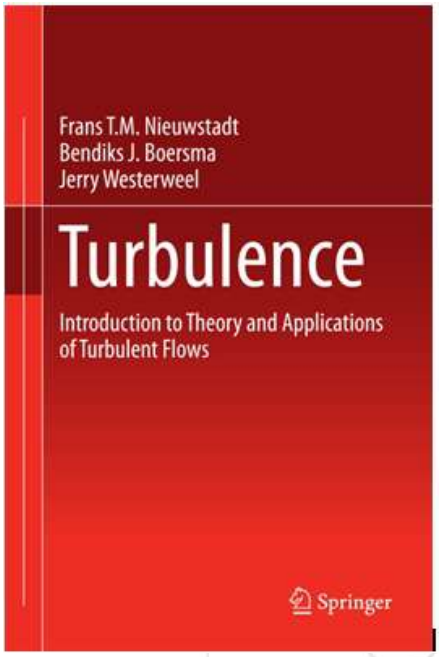

- **Winner of the 2017 Most Promising New Textbook Award from the Textbook & Academic Authors Association**
- Proven to be an excellent course-text over many years
- Combines theory with practical applications
- Avoids lengthy mathematical descriptions

This book provides a general introduction to the topic of turbulent flows. Apart from classical topics in turbulence, attention is also paid to modern topics. After studying this work, the reader will have the basic knowledge to follow current topics on turbulence in scientific literature. The theory is illustrated with a number of examples of applications, such as closure models, numerical simulations and turbulent diffusion, and experimental findings. The work also contains a number of illustrative exercises

ERCOFTAC Workshops and Summer Schools

ERCOFTAC Workshops, Conferences – 2020

Title	Location	Date	Coordinators	Organiser
3rd Workshop on Modelling of Biological Cells, Fluid Flow and Microfluidics 2020	Vratna, Slovakia	09-13/02/2020	Kovalcikova K.	SIG 37
Multiscale and directional approach to single-phase and two-phase flows	France	4-7/05/2020	Cambon, C., Gorokhovski M., Casciola C. M.	SIGs 35, 39, 50, Henry Bénard PC
15th International SPHERIC Workshop	Newark, USA	15-18/06/2020	Tafuni, A. Rogers, B.	SIG 40
Reconstruction methods for complex flows and porous media	Sheffield, UK	22-23/06/2020	Yi Li	SIG 42, 14
3rd Workshop and Challenge on Data Assimilation & CFD Processing for PIV and Lagrangian Particle Tracking	Lisbon, Portugal	11-12/07/2020	Sciacchitano A.	SIG 32

ERCOFTAC Summer Schools, Courses - 2020

Title	Location	Date	Coordinators	Organiser
Course on Particle Image Velocimetry	Delft, Netherlands	8-12/06/2020	Sciacchitano A.	SIG 32
Fluids under Control	Prague, Czech Republic	24–28/08/2020	Bodnar T.	PC Czech Republic
2nd International School on Hemophysiscs	Montpellier, France	06-09/10/2020	Nicoud F.	SIG 37

Flow, Turbulence and Combustion Journal

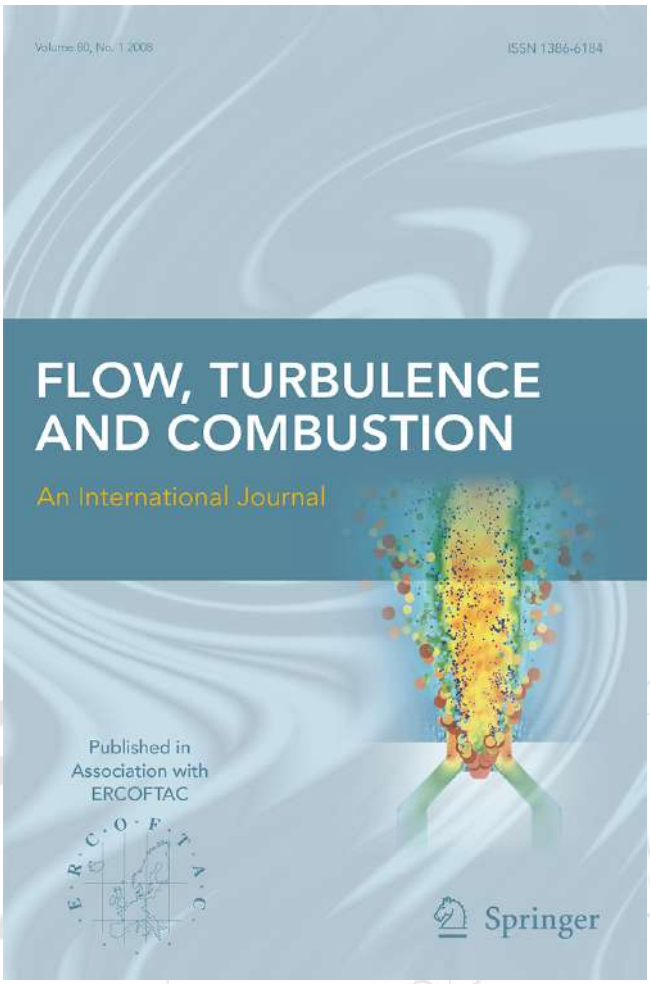

http://link.springer.com/journal/10494

2018 Impact Factor: 2.371

As stated on its cover, **Flow, Turbulence and Combustion (FTAC)** *is published in association with ERCOFTAC"*. The expectation is, therefore, that FTaC would be a primary medium for disseminating the most innovative and highest-quality scientific output of ERCOFTAC-supported technical events.

In addition to contributed articles constituting the large majority of FTaCs published output FTaC publishes *special issues* arising from major ERCOFTAC conferences, notably **ETMM** and (in 2017) **DLES**. However, there are many other opportunities that are, arguably, not sufficiently exploited in particular, in respect of original contributions to theme issues of the Bulletin and papers arising from SIG events, such as workshops and summer schools.

Both the Editor-in-Chief of FTaC and the Scientific Programme Committee of ERCOFTAC wish to see more contributions channelled from ERCOFTAC sources to FTaC. Such contributions in the form of high-quality technical papers within the scope of FTaC are most welcome. They will be subjected to the same rigorous review process as any other contributed manuscript.

FTaC provides a forum with global reach for the publication of original and innovative research results that contribute to the solution of fundamental and applied problems encountered in single-phase, multi-phase and reacting flows, both in idealized and real systems. This includes topics in fluid dynamics, scalar transport, multi-physics interactions and flow/turbulence control. Contributions may report research that falls within the broad spectrum of analytical, computational and experimental methods, including research pursued in academia, industry and the variety of environmental and geophysical sectors. The emphasis is on originality, timeliness, quality and thematic fit, as identified by the title of the journal and the above qualifications. Relevance to real-world problems and industrial applications will be regarded as strengths. Contributions may be full-length research and review manuscripts or short communications (of no more than 6 printed pages). The latter may report new results, address contentious topics or contain discussions of full-length papers previously published in the journal. Short communications will benefit from rapid publication. All contributed manuscripts, as well as any invited contributions to special or theme issues, will undergo rigorous peer review by three expert reviewers prior to decisions on acceptance or rejection.

Flow, Turbulence and Combustion Journal

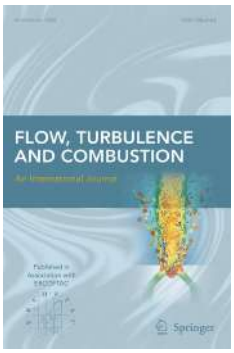

Recent Table Of Contents Of Flow Turbulence And Combustion
An International Journal Published By Springer
In Association With ERCOFTAC
Editor-In-Chief: M. A. Leschziner
Editors: A. Dreizler, K. Fukagata, E. Gutmark, A. Kempf, S. Menon, W. Rodi, T. Schuller, B. van Wachem, R. Sandberg
Founding Editor: F. Nieuwstadt

Volume 104, Number 1, January 2020

Further articles can be found at `www.springerlink.com`

Abstracted/Indexed in Science Citation Index, Science Citation Index Expanded (SciSearch), Journal Citation Reports/Science Edition, SCOPUS, INSPEC, Chemical Abstracts Service (CAS), Google Scholar, EBSCO, CSA, ProQuest, Academic OneFile, ASFA, Current Abstracts, Current Contents/Engineering, Computing and Technology, Earthquake Engineering Abstracts, EI Encompass, Ei Page One, EI-Compendex, EnCompassLit, Engineered Materials Abstracts, Gale, OCLC, PASCAL, SCImago, STMA-Z, Summon by Serial Solutions, VINITI - Russian Academy of Science.

Instructions for Authors for Flow Turbulence Combust are available at `http://www.springer.com/10494`.

Flow, Turbulence and Combustion Journal

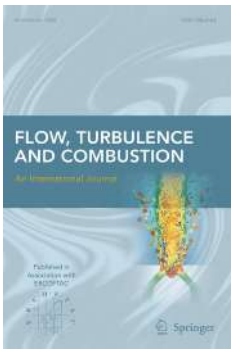

Recent Table Of Contents Of Flow Turbulence And Combustion
An International Journal Published By Springer
In Association With ERCOFTAC
Editor-In-Chief: M. A. Leschziner
Editors: A. Dreizler, K. Fukagata, E. Gutmark, A. Kempf, S. Menon, W. Rodi, T. Schuller, B. van Wachem, R. Sandberg
Founding Editor: F. Nieuwstadt

Volume 104, Number 2-3, March 2020

Special Issue: Progress in Engineering Turbulence Modelling, Simulation and Measurements
Guest Editors: Franck Nicoud, Stefan Hickel, Ananias Tomboulides, Wolfgang Rodi and Michael Leschziner

Progress in Engineering Turbulence Modelling, Simulation and Measurements
F. Nicoud, S. Hickel, A. Tomboulides, W. Rodi, M. Leschziner

Characterization of the Spatio-Temporal Response of a Turbulent Boundary Layer to Dynamic Roughness
D. Huynh, B. McKeon

Skin Friction Measurements of Systematically-Varied Roughness: Probing the Role of Roughness Amplitude and Skewness
K.A. Flack, M.P. Schultz, J.M. Barros

Influence of Surface Anisotropy on Turbulent Flow Over Irregular Roughness
A. Busse, T.O. Jelly

The Effects of Froude Number on a Turbulent Boundary Layer with a Free-Surface
F. Nasiri, E. Balaras

Turbulent Heat-Transfer Enhancement in Boundary Layers Exposed to Free-Stream Turbulence
J. You, T.A. Zaki

Evaluation of Flame Area Based on Detailed Chemistry DNS of Premixed Turbulent Hydrogen-Air Flames in Different Regimes of Combustion
M. Klein, A. Herbert, H. Kosaka, B. Böhm, A. Dreizler, N. Chakraborty, V. Papapostolou, H.G. Im, J. Hasslberger

Impact of Spray Droplet Distribution on the Performances of a Kerosene Lean/Premixed Injector
P. Domingo-Alvarez, P.Bénard, V. Moureau, G. Lartigue, F. Grisch

Response of Heat Release Rate to Flame Straining in Swirling Hydrogen-Air Premixed Flames
K. Aoki, M. Shimura, J. Park, Y. Minamoto, M. Tanahashi

Numerical Characterization of a Premixed Hydrogen Flame Under Conditions Close to Flashback
D. Mira, O. Lehmkuhl, A. Both, P. Stathopoulos, T. Tanneberger, T.G. Reichel, C.O. Paschereit, M. Vzquez, G. Houzeaux

Modal Analysis of a Laminar-Flow Airfoil under Buffet Conditions at Re=500,000
M. Zauner, N.D. Sandham

Transitional Flow Dynamics Behind a Micro-Ramp
J. Casacuberta, K.J. Groot, Q. Ye, S. Hickel

Numerical Investigation of Jet-Wake Interaction for a Dual-Bell Nozzle
S. Loosen, M. Meinke, W. Schröder

Discovery of Algebraic Reynolds-Stress Models Using Sparse Symbolic Regression
M. Schmelzer, R.P. Dwight, P. Cinnella

An a priori DNS analysis of scale similarity based combustion models for LES of non-premixed jet flames
A. Shamooni, A. Cuoci, T. Faravelli, A. Sadiki

Turbulence Modeling for Turbulent Boundary Layers at Supercritical Pressure:A Model for Turbulent Mass Flux
S. Kawai, Y. Oikawa

Assessment of a Coolant Injection Model on Cooled High-Pressure Vanes with Large-Eddy Simulation
M. Harnieh, M. Thomas R. Bizzari, J. Dombard, F. Duchaine, L. Gicquel

LES of the Gas-Exchange Process Inside an Internal Combustion Engine Using a High-Order Method
G.K. Giannakopoulos, C.E. Frouzakis, P.F. Fischer, A.G. Tomboulides, K. Boulouchos

Numerical Investigations of Phase-Separation During Multi-Component Mixing at Super-Critical Conditions
P. Tudisco, S. Menon

Wall-Modeled Large-Eddy Simulations of a Multistage High-Pressure Compressor
J. de Laborderie, F. Duchaine, L. Gicquel, S. Moreau

Analysis of the Soot Particle Size Distribution in a Laminar Premixed Flame: A Hybrid Stochastic/Fixed-Sectional Approach
A. Bouaniche, J. Yon, P. Domingo, L. Vervisch

1. Large Eddy Simulation
Salvetti, M.V.
University of Pisa, Italy.
Tel: +39 050 221 7262
mv.salvetti@ing.unipi.it

4. Turbulence in Compressible Flows
Dussauge, Jean-Paul
IUSTI, Marseille
jean-paul.dussauge
@polytech.univmrs.fr

5. Environmental Fluid Mechanics
Armenio, V.
Universit di Trieste, Italy
Tel: +39 040 558 3472
armenio@dica.units.it

10. Transition Modelling
Dick, E.
University of Ghent, Belgium
Tel: +32 926 433 01
erik.dick@ugent.be

12. Dispersed Turbulent Two Phase Flows
Sommerfeld, M.
University of Magdeburg, Germany
Tel: +49 345 552 3680
martin.sommerfeld@ovgu.de

14. Stably Stratified and Rotating Flows
Redondo, J.M.
UPC, Spain
Tel: +34 934 017 984
redondo@fa.upc.edu

15. Turbulence Modelling
Jakirlic, S.
Darmstadt University of Technology, Germany
Tel: +49 615 116 3554
s.jakirlic@sla.tu-darmstadt.de

20. Drag Reduction and Flow Control
Choi, K-S.
University of Nottingham, England
Tel: +44 115 951 3792
kwing-so.choi@nottingham.ac.uk

28. Reactive Flows
Roekaerts, D.
Delft University of Technology,
The Netherlands.
Tel: +31 152 782 470
D.J.E.M.Roekaerts@tudelft.nl

32. Particle Image Velocimetry
Scarano, F., Sciacchitano, A.
Delft University of Technology,
The Netherlands.
F.Scarano@tudelft.nl
A.Sciacchitano@tudelft.nl

33. Transition Mechanisms, Prediction and Control
Hanifi, A.
FOI, Sweden
Tel: +46 855 503 197
ardeshir.hanifi@foi.se

34. Design Optimisation
Giannakoglou, K.
NTUA, Greece
Tel: +30 210 772 1636
kgianna@central.ntua.gr

35. Multipoint Turbulence Structure and Modelling
Cambon, C.
ECL Ecully, France.
Tel: +33 472 186 161
claude.cambon@ec-lyon.fr

36. Swirling Flows
Braza, M.
IMFT, France
Tel: +33 (0) 561 285 839
braza@imft.fr

37. Bio-Fluid Mechanics
Nicoud, F.
Université de Montpellier, France
franck.nicoud@umontpellier.fr

39. Aeroacoustics
Bailly, C.
Ecole Centrale de Lyon, France
Tel: +33 472 186 014
christophe.bailly@ec-lyon.fr

40. Smoothed Particle Hydrodynamics
Rogers, B. D.
University of Manchester, UK
Tel: +44 (0) 161 306 6000
Benedict.Rogers@manchester.ac.uk

41. Fluid Structure Interaction
Braza, M.
IMFT, France
Tel: +33 (0) 561 285 839
marianna.braza@imft.fr
Lacazedieu, E.
EDF R&D, France
Tel: +33 (1) 30 87 80 87
elisabeth.lacazedieu@edf.fr

42. Synthetic Models in Turbulence
Nowakowski, A.
University of Sheffield, England
Tel: +44 114 222 7812
a.f.nowakowski@sheffield.ac.uk

43. Fibre Suspension Flows
Lundell, F.
The Royal Institute of Technology, Sweden
Tel: +46 87 906 875
fredrik@mech.kth.se

44. Multiscale-generated Turbulent Flows
Fortune, V.
Université Pierre et Marie Curie, France
Tel: +33 549 454 044
veronique.fortune
@lea.univ-poitiers.fr

45. Uncertainty Quantification in Industrial Analysis and Design
Lucor, D.
d'Alembert Institute, France
Tel: +33 (0) 144 275 472
didier.lucor@upmc.fr

46. Oil, Gas and Petroleum
Sommerfeld, M.
Otto von Guericke-Universität Germany
martin.sommerfeld@ovgu.de
Khanna, S.
BP Global, USA

47. 3D Wakes
Morrison, J.F.
Imperial College, London
Tel: +44 (0) 20 7594 5067
j.morrison@imperial.ac.uk
Cadot, O.
ENSTA Paris Tech,
Université Paris-Saclay
Tel: +33 (0) 16 931 9756
cadot@ensta.fr

48. Respiratory Aerosols
Kassinos, S.
University of Cyprus
kassinos@ucy.ac.cy
Sznitman, J.
Biofluids Laboratory, Israel
sznitman@bm.technion.ac.il

49. Non-Ideal Comp. Fluid Dynamics
Guardone, A.
Politecnico di Milano, Italy
alberto.guardone@polimi.it
Pini, M.
Delft University of Technology,
The Netherlands
M.Pini@tudelft.nl

50. GeoAstro
Marino, R.
CNRS/École Centrale de Lyon, France
raffaele.marino@ec-lyon.fr

51. High-Pressure & Compressible Combustion
di Mare, F.
University Bochum, Germany
Francesca.dimare@rub.de

ERCOFTAC Pilot Centres

Alpe - Danube - Adria
Steiner, H.
Inst. Strömungslehre and
Wärmeübertragung
TU Graz, Austria
kristof@ara.bme.hu

Belgium
Hillewaert, K.
Bâtiment Eole,
6041 Gosselies,
Belgium.
Tel: +32 71 910 942
Fax: +32 495 385 030
koen.hillewaert@cenaero.be

Brasil
Rodriguez, O.
Department of Mechanical Engineering,
Sao Carlos School of Mechanical
Engineering,
Universidade de Sao Paulo,
Brasil.
oscarmhr@sc.usp.br

Czech Republic
Bodnar, T.
Institute of Thermomechanics AS CR,
5 Dolejskova,
CZ-18200 Praha 8,
Czech Republic.
Tel: +420 224 357 548
Fax: +420 224 920 677
bodnar@marian.fsik.cvut.cz

Iberia
Onate, E.
Universitat Politenica de Catalunya,
Valero, E.
Universidad Politécnica de Madrid,
Spain.
onate@cimne.upc.edu
eusebio.valero@upm.es

France South
Braza, M.
IMF Toulouse,
CNRS UMR - 5502,
Allée du Prof. Camille Soula 1,
F-31400 Toulouse Cedex, France.
Tel: +33 534 322 839
Fax: +33 534 322 992
Braza@imft.fr

France West
Hadjadj, A.
Tel: +33 232 959 794
hadjadj@coria.fr
CORIA, France
Lucor, D.
Tel: +33 (0)169 157 226
didier.lucor@limsi.fr
LIMSI-CNRS, France

Germany North
Sommerfeld, M.
University of Magdeburg,
Germany
Tel: +49 345 552 3680
martin.sommerfeld@ovgu.de

Germany South
Becker, S.
Universität Erlangen, IPAT
Cauerstr. 4
91058 Erlangen
Germany
Tel: +49 9131 85 29451
Fax: +49 9131 85 29449
sb@ipat.uni-erlangen.de

Greece
M. Founti.
National Tech. University Of Athens,
School of Mechanical Engineering,
Lab. of Steam Boilers and
Thermal Plants,
Heroon Polytechniou 9,
15780 Zografou, Athens, Greece
Tel: +30 210 772 3605
Fax: +30 210 772 3663
mfou@central.ntua.gr

Switzerland
The new coordinator to be confirmed.

Italy
Rispoli, F.
Tel: +39 064 458 5233
franco.rispoli@uniroma1.it
Borello, D
Tel: +39 064 458 5263
domenico.borello@uniroma1.it
Sapienza University of Rome,
Via Eudossiana, 18
00184 Roma, Italy

Netherlands
Van Heijst, G.J.
J.M. Burgerscentrum,
National Research School for Fluid
Mechanics, Mekelweg 2,
NL-2628 CD Delft, Netherlands.
Tel: +31 15 278 1176
Fax: +31 15 278 2979
g.j.f.vanheijst@tudelft.nl

Nordic
Wallin, S.
KTH, Dept. of Mechanics,
SE-100 44 Stockholm,
Sweden
Tel: +46 733 303 453
stefanw@mech.kth.se

Poland
Szumbarski J.
Warsaw University of Technology,
Inst. of Aero. & App. Mechanics,
ul. Nowowiejska 24,
PL-00665 Warsaw, Poland.
Tel: +48 22 234 7444
Fax: +48 22 622 0901
jasz@meil.pw.edu.pl

France - Henri Bénard
Godeferd, F.S.
Ecole Centrale de Lyon.
Fluid Mechanics and Acoustics Lab.,
F-69134 Ecully Cedex,
France.
Tel: +33 4 72 18 6155
Fax: +33 4 78 64 7145
fabien.godeferd@ec-lyon.fr

United Kingdom
Juniper, M.
Department of Engineering,
Trumpington Street,
Cambridge, CB2 1PZ
United Kingdom.
Tel: +44 (0) 1223 332 585
mpj1001@cam.ac.uk

ISSN: 2518-0991

Best Practice Guidelines for Computational Fluid Dynamics of Dispersed Multi-Phase Flows

Editors

Martin Sommerfeld, Berend van Wachem
&
René Oliemans

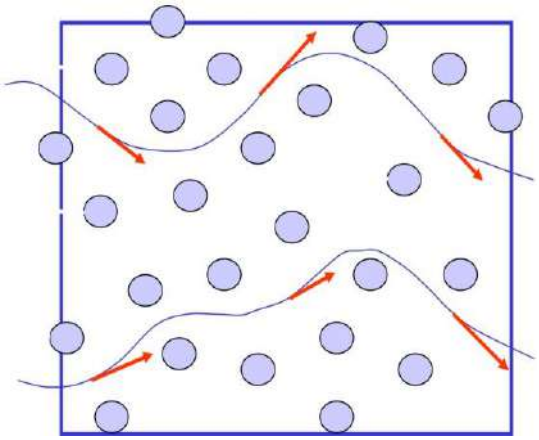

The simultaneous presence of several different phases in external or internal flows such as gas, liquid and solid is found in daily life, environment and numerous industrial processes. These types of flows are termed multiphase flows, which may exist in different forms depending on the phase distribution. Examples are gas-liquid transportation, crude oil recovery, circulating fluidized beds, sediment transport in rivers, pollutant transport in the atmosphere, cloud formation, fuel injection in engines, bubble column reactors and spray driers for food processing, to name only a few. As a result of the interaction between the different phases such flows are rather complicated and very difficult to describe theoretically. For the design and optimisation of such multiphase systems a detailed understanding of the interfacial transport phenomena is essential. For single-phase flows Computational Fluid Dynamics (CFD) has already a long history and it is nowadays standard in the development of air-planes and cars using different commercially available CFD-tools.

Due to the complex physics involved in multiphase flow the application of CFD in this area is rather young. These guidelines give a survey of the different methods being used for the numerical calculation of turbulent dispersed multiphase flows. The Best Practice Guideline (BPG) on Computational Dispersed Multiphase Flows is a follow-up of the previous ERCOFTAC BPG for Industrial CFD and should be used in combination with it. The potential users are researchers and engineers involved in projects requiring CFD of (wall-bounded) turbulent dispersed multiphase flows with bubbles, drops or particles.

Table of Contents

Copies of the Best Practice Guidelines can be acquired electronically from the ERCOFTAC website:

www.ercoftac.org

Or from:

ERCOFTAC (CADO)
PO Box 1212
Bushey, WD23 9HT
United Kingdom

Tel: +44 208 117 6170
Email: admin@cado-ercoftac.org

The price per copy (not including postage) is:

ERCOFTAC members	
First copy	*Free*
Subsequent copies	75 Euros
Students	75 Euros
Non-ERCOFTAC academics	140 Euros
Non-ERCOFTAC industrial	230 Euros
EU/Non EU postage fee	10/17 Euros